Development of Advanced Polycrystalline Diamond Coatings on Cutting Tools for CFRP Composites

March 2023

Soldatov Alexander

Graduate School of
Natural Science and Technology
(Doctoral Course)

OKAYAMA UNIVERSITY

Abstract

The aim of this thesis is improvement in cutting performance of diamond coated tools in machining CFRP composite materials. Such improvement has achieved through application of advanced polycrystalline diamond coatings for WC-Co based cutting tools. Also, a reconditioning approach to the diamond coated tools has been proposed.

A hot filament chemical vapor deposition (HFCVD) method to prepare the diamond coatings with different film morphologies through boron doping was described in term of a fundamentals, applied equipment, a deposition parameters and a substrate pretreatment technique. Experimental investigations of cutting performance of CFRP with undoped, and boron-doped CVD diamond-coated drills were performed. In additional, the influences of the diamond coating properties, such as film morphology, boron doping, and etc., on the film adhesion itself and the drilled hole quality were clarified by evaluating the tool wear, thrust force, torque and CFRP delamination. According to the results, the boron-doped microcrystalline diamond (B-MCD) coated drills presented advantages in tool life and quality of drilled holes over the undoped nanocrystalline diamond (NCD) and boron-doped nanocrystalline diamond (B-NCD) coated drills. Also, the results reveal adhesion enhanced effect of the CVD diamond coating to WC-Co substrate through appropriate boron doping of the film.

In addition, the developed reconditioning technique of the diamond-coated tools for industries applications was described. Experiments were performed by B-MCD coatings on the WC-Co drills and following tool decoating by reactive ion beam etching (RIBE). Cutting tests were carried out and repeated to evaluate cutting performance of reconditioned drills and compare with the new drills. As result, the cutting ability of the reconditioned drills was confirmed. Moreover, even the two-time reconditioned drills showed the cutting performance results comparable with the new drills in terms of tool flank wear and drilled hole quality. All produced CFRP holes kept the required hole size and showed the absence of critical delamination and burrs. In order to estimate an influence of reconditioning procedures on drills' cutting ability, tool substrate textures were investigated in terms of surface morphology, adhesion, and cutting edge geometries. The results obtained show that repeated tool substrate pretreatment before HFCVD process created in crater formation in the WC-Co and should be tailored for the tool reconditioning. The developed reconditioning approach to the B-MCD-coated cutting tools gives significant advantages in CFRP machining in terms of the tool cost and the material savings and may facilitate a transition towards an eco-friendly circular economy.

Table of contents

Abstract i

Table of contents ii

List of figures v

List of tables ix

List of abbreviations x

Chapter 1 Introduction 1

1.1 Background and motivation 1

1.2 Overview of composite materials 3

1.2.1 Classification of composite materials 3

1.2.2 Fiber-reinforced plastic (FRP) composites 6

1.2.3 Description of CFRP composite components 11

1.2.4 Manufacturing of CFRP composites 13

1.3 Drilling of CFRP composites 13

1.3.1 Introduction 13

1.3.2 Drilled hole quality 15

1.3.3 Tool shapes, materials, and coatings applied for drilling of CFRP composites 20

1.3.3.1 Tool shapes 20

1.3.3.2 Tool materials 22

1.3.3.3 Tool coatings 23

1.4 Machinability of CFRP composites 26

1.4.1 Effect of material properties 26

1.4.2 Effect of process parameters 29

1.4.3 Effect of tool materials and geometries 30

1.5 Tool wear phenomena 31

1.6 Research objective 34

1.7 Overview and outline of the thesis 36

Chapter 2 Advanced diamond coatings and their cutting performance in drilling of CFRP laminates 37
2.1 Introduction 37
2.2 Diamond synthesis by CVD 38
2.2.1 CVD systems 38
2.2.1.1 HFCVD 39
2.2.1.2 Plasma-enhanced CVD methods 40
2.2.1.3 Combustion-flame-assisted CVD 41
2.2.1.4 Summary 42
2.2.2 CVD diamond coatings for cutting tool application 45
2.2.3 Optimizing adhesion of CVD diamond coatings to cutting tools 47
2.2.3.1 Wet-chemical etching method 47
2.2.3.2 Intermediate layers 48
2.2.3.3 Thermal treatment 48
2.2.3.4 Doping into diamond coatings 49
2.2.3.5 Summary 49
2.3 Experimental procedures 50
2.3.1 Applied drills 50
2.3.2 Substrate preparation and deposition of the diamond coatings 51
2.3.3 Drilling tests 56
2.4 Experimental results and discussion 58
2.4.1 Characterization of deposited diamond coatings 58
2.4.2 Drill flank wear evaluation 63
2.4.3 Thrust force and torque evaluation 66
2.4.4 Hole quality evaluation 68
2.5 Conclusions 72

Chapter 3 Reconditioning of diamond coated tools 73
3.1 Introduction 73
3.2 General features of RIBE process 76
3.2.1 Ion beam definition 76
3.2.2 Closed Drift Ion Source “RADICAL” 76

3.2.3 “RADICAL” CDIS operation parameters 79
3.2.4 Application for diamond films etching 80
3.3 Materials and methods 82
3.3.1 Experimental procedures 82
3.3.2 Cutting tools 83
3.3.3 Substrate preparation and deposition of the diamond coating 84
3.3.4 Decoating by RIBE 88
3.3.5 Cutting tests 89
3.4 Experimental results and discussion 91
3.4.1 Tool surface evaluation 91
3.4.2 Adhesion evaluation 95
3.4.3 Cutting edge rounding evaluation 96
3.4.4 Drill flank wear evaluation 99
3.4.5 Thrust force evaluation 101
3.4.6 Hole quality evaluation 104
3.5 Conclusions 109

Chapter 4 Conclusions 110

References 114
Acknowledgements 126
List of publications 127

List of figures

Figure 1.1 Mechanical properties of various metals and composites 2
Figure 1.2 Classification for various composites according to reinforcement format 4
Figure 1.3 The most commonly used fabric types 5
Figure 1.4 Example of stacking sequence in multidirectional layup 6
Figure 1.5 Relative properties for various individual fibers 7
Figure 1.6 Manufacturing process for making carbon/graphite fibers 8
Figure 1.7 Different possible ply orientation for UD laminate layup 12
Figure 1.8 Quasi-isotropic vs. unidirectional lay-up 12
Figure 1.9 Quality criteria when drilling FRPs 15
Figure 1.10 Delamination forms: (a) peel-up at entrance and (b) push-out at exit 16
Figure 1.11 Diagram of the delamination damage: (a) uniform damage, (b) cracks, (c) uniform damage with cracks and (d) uniform damage with fine cracks 17
Figure 1.12 Acceptable damage (courtesy of Bombardier Aerospace) 19
Figure 1.13 Uncut fibers at the exit of drilled holes in UD-CFRPs 20
Figure 1.14 Schematic drawings of different drilling tools for CFRPs: (a) conventional twist drill, (b) double point angle twist drill, (c) brad & spur drill (candlestick drill), (d) dagger drill (one-shot drill), (e) step drill, (f) core drill and (g) the special core drill 20
Figure 1.15 Flank wear results of different tool materials when turning CFRP 25
Figure 1.16 Factors affecting machinability of CFRP composites 26
Figure 1.17 Cutting mechanisms in the orthogonal machining of FRP composites 27
Figure 1.18 Microstructure when orthogonal cutting of graphite/epoxy composite: (a) $\theta = 150^\circ$ and 0.05 mm depth of cut and (b) $\theta = 120^\circ$ and 0.1 mm depth of cut 28
Figure 1.19 A cross section of a replica from a cutting edge when machining FRPs (α_o is the rake angle and γ_o is the clearance angle) 31
Figure 1.20 Schematic illustration showing tool wear patterns in (a) adhesion and abrasion wear, (b) extended abrasion wear on the flank face, (c) flaking and delamination and (d) breakage of substrate material 32

Figure 2.1 Schematic diagram of HFCVD method 39

Figure 2.2 Schematic diagram of microwave CVD method 40

Figure 2.3 Schematic diagram of DC arc jet CVD method 41

Figure 2.4 Schematic diagram of combustion-flame assisted CVD method 42

Figure 2.5 Principle of the HFCVD process 45

Figure 2.6 Kinds of HFCVD diamond coatings applied for cutting tools: (a) MCD, (b) NCD, (c) Multilayer and schematic representation of crack propagation (red line marked) for (d) MCD, (e) NCD, (f) Multilayer, respectively 46

Figure 2.7 WC-Co drill for CFRP drilling: (a) drill shank side, (b) reamer cutting side, (c) drill cutting edge side, (d) primary cutting edge, (e) secondary cutting edge, and (f) tertiary cutting edge 51

Figure 2.8 The WCE process for WC-Co substrate pretreatment 52

Figure 2.9 The WC-Co substrate morphology: a) original, b) after WCE process 52

Figure 2.10 HFCVD experimental setup 53

Figure 2.11 Schematic diagram of hot filaments arrangement and drill setting into the HFCVD setup chamber: (a) Chamber; (b) Current feedthrough; (c) Drills with ceramic holders; (d) Filament holder; (e) Grounded filament holder; (f) Hot filaments; (g) Table 55

Figure 2.12 Experimental CVD setup chamber with installed drills: (a) Reactor, (b) Filaments, (c) Drills with ceramic holders, (d) Table 56

Figure 2.13 Experimental setup for drilling tests: (a) dynamometer, (b) tested drill, (c) CFRP workpiece, and (d) fixture 58

Figure 2.14 SEM images of surface morphologies observed on drill tip area of the coated drills (a) for: (b) NCD, (c) B-MCD, and (d) B-NCD coatings 59

Figure 2.15 Topographic images with surface profiles, observed on a flank area of cutting edge, for: (a) NCD, (b) B-MCD, and (c) B-NCD coated drills, respectively 60

Figure 2.16 Raman spectra of NCD, B-MCD and B-NCD coated drills, using green ($\lambda = 532$ nm) excitation 61

Figure 2.17 SEM images of indentation morphologies, obtained by Rockwell testing machine with a load of 1471 N, on: (a) NCD, (b) B-MCD, and (c) B-NCD coated drills, respectively 62

Figure 2.18 Variations of maximum flank wear as a function of drilled hole number 63
Figure 2.19 SEM images of the drills after drilling 600 holes: (a, b) NCD coated drill, (c, d) B-MCD coated drill and (e, f) B-NCD coated drill 65
Figure 2.20 Variations of the thrust force as a function of drilled hole number 67
Figure 2.21 Variations of the torque as a function of drilled hole number 67
Figure 2.22 Schematic diagram of delamination factor (*F*d) 68
Figure 2.23 Variations of the delamination factor on entry hole side as a function of drilled hole number 69
Figure 2.24 Variations of the delamination factor on exit hole side as a function of drilled hole number 69
Figure 2.25 Images of CFRP hole exit: (a) 300th hole made by WC-Co drill and 600th holes made by NCD (b), B-MCD (c), B-NCD (d) coated drills, respectively 71
Figure 3.1 RIBE experimental setup 77
Figure 3.2 Structure of "RADICAL" type based CDIS: (a) external cathode ring; (b) acceleration channel; (c) internal cathode ring; (d) anode; (e) magnetic coil 78
Figure 3.3 Etching rate as a function of CDIS discharge current 81
Figure 3.4 Tool life with multiple reconditioning cycles 82
Figure 3.5 One-shot WC-Co drill utilized in the current study: (a) drill shank; (b) reamer cutting portion; (c) cutting edge portion; (d) magnified view of the drill cutting edge portion; (e) primary cutting edge; (f) rounded corner; (g) secondary cutting edge; (h) tertiary cutting edge 83
Figure 3.6 Original semi-automatic setup for chemical substrate pretreatment 84
Figure 3.7 WCE cycle for chemical substrate pretreatment 85
Figure 3.8 Industrial diamond coating system (ShinMaywa Industries) 87
Figure 3.9 Industrial ion etching system IE800 (ShinMaywa Industries) 88
Figure 3.10 RIBE experimental setup for tool de-coating: (a) vacuum chamber; (b) CDIS; (c) processed cutting tools; (d) planetary rotation system; (e) simulated ion beam, pink colored 89
Figure 3.11 Experimental setup for cutting tests: (a) machine; (b) tested drill; (c) CFRP workpiece; (d) fixture; (e) dynamometer 90

Figure 3.12 Morphologies of the drill flank surface, observed at 6 mm from the drill tip: (a) original, as grinded; (b) wet-chemical etching 0 (WCE0) of the new drill (TLC0); (c) chemical vapor deposition 0 (CVD0) of the TLC0; (d) reactive ion beam etching 1 (RIBE1) of the 1st-time reconditioned drill (TLC1); (e) WCE1 of the TLC1; (f) CVD1 of the TLC1; (g) RIBE2 of the 2nd-time reconditioned drill (TLC2); (h) WCE2 of the TLC2; (i) CVD2 of the TLC2 91
Figure 3.13 Substrate roughness characteristics by the arithmetical mean height (*S*a) of the surface texture 92
Figure 3.14 Raman spectra of the CVD0, CVD1, and CVD2 coatings, using a green ($\lambda = 532$ nm) excitation 94
Figure 3.15 SEM images of indentation morphologies, obtained by a Rockwell testing machine with a load of 980.7 N on the TLC0 (a), the TLC1 (b), and the TLC2 (c, d) 96
Figure 3.16 Measurement results of the cutting edge rounding (CER) 97
Figure 3.17 Change of the CER (6 mm measured point) 98
Figure 3.18 Change of the CER (11 mm measured point) 98
Figure 3.19 Variations of the maximum flank wear as a function of the drilled holes number. 99
Figure 3.20 SEM images of the TLC0 (a–c), the TLC1 (d–f), and the TLC2 (g–i) after drilling 200 holes 100
Figure 3.21 Variations of thrust forces for the TLC0, TLC1 and TLC2 during drilling process of 100th hole 102
Figure 3.22 Variations of the thrust force as a function of drilled holes number 103
Figure 3.23 SEM images of drill tip area of the TLC0 (a–c), the TLC1 (d–f), and the TLC2 (g–i) after diamond coating deposition 104
Figure 3.24 Variations of the delamination factor on the entry hole side as a function of the drilled holes number 106
Figure 3.25 Variations of the delamination factor on the exit hole side as a function of the drilled holes number 106
Figure 3.26 Images of the 1st and 200th CFRP hole entry sides made by the TLC0 (a, d), made by the TLC1 (b, e), and made by the TLC2 (c, f) 107
Figure 3.27 Images of 1st and 200th CFRP hole exit sides made by the TLC0 (a, d), made by the TLC1 (b, e), and made by the TLC2 (c, f) 108

List of tables

Table 1.1 Properties of various carbon fiber types 9

Table 1.2 Classification of carbon fibers based on their tensile strength and modulus 9

Table 1.3 Mechanical properties for the common CFRP laminates against GFRP and AFRP composites 11

Table 2.1 CVD method comparison 44

Table 2.2 Deposition process parameters 54

Table 2.3 Composition of prepreg P2352W-19 (TORAY) 57

Table 2.4 Mechanical properties of the CFRP laminate 57

Table 3.1 “RADICAL” CDIS operating parameters 79

Table 3.2 WCE process steps 86

Table 3.3 Deposition process parameters 87

List of abbreviations

AFRP : Aramid fiber reinforced plastic
AWJ : Abrasive water jet
BDD : Boron-doped diamond
B-MCD : Boron-doped microcrystalline diamond
B-NCD : Boron-doped nanocrystalline diamond
C : Carbon
CDIS : Closed electron drift ion source
CER : Cutting edge rounding
CFRP : Carbon fiber reinforced plastic
CMC : Ceramic matrix composite
Co : Cobalt
CVD : Chemical vapor deposition
CVD0 : CVD diamond film, deposited on the new tool
CVD1 : CVD diamond film, deposited in the first reconditioning cycle
CVD2 : CVD diamond film, deposited in the second reconditioning cycle
DC : Direct current
DLC : Diamond like carbon
ECE : Electrochemical etching
FRP : Fiber reinforced plastic
GFRP : Glass fiber reinforced plastic
HFCVD : Hot filament chemical vapor deposition
HPHT : High pressure – high temperature synthesis
HSS : High speed steel
MCD : Undoped microcrystalline diamond
MD : Multidirectional
MMC : Metal matrix composite
NCD : Undoped nanocrystalline diamond
PAN : Polyacrylonitrile based carbon
PCD : Polycrystalline diamond
PMC : Polymer matrix composite
PVD : Physical vapor deposition

RIBE : Reactive ion beam etching
RIBE1 : Reactive ion beam etching of the diamond coated drill for the first time
RIBE2 : Reactive ion beam etching of the diamond coated drill for the second time
SEM : Scanning electron microscope
TLC : Tool life cycle
TLC0 : Tool life cycle of the newly deposited tool
TLC1 : Tool life cycle of the first-time reconditioned tool
TLC2 : Tool life cycle of the second-time reconditioned tool
UD : Unidirectional
WC : Tungsten carbide
WCE : Wet chemical etching
WCE0 : Wet chemical etching of the new WC-Co substrate
WCE1 : Wet chemical etching of the WC-Co substrate in the first reconditioning cycle
WCE2 : Wet chemical etching of the WC-Co substrate in the second reconditioning cycle

Chapter 1. Introduction

1.1 Background and motivation

Composite materials have played an important role throughout human history, from housing early civilizations to enabling future innovations. Indeed, humans have been using composite materials for thousands of years in different areas. The first uses of composites date back to 1500 BC when early Egyptians and Mesopotamian settlers used a mixture of mud and straw to create strong and durable buildings. The combination of mud and straw in a block of brick provides it a strong property against both squeezing and tearing or bending. The straw continued to reinforce ancient composite products, including pottery and boats [1]. In 1200 AD, the Mongols invented the first composite bow using a combination of "animal glue", bone, and wood. The bows were pressed and wrapped with birch bark. Composite Mongolian bows helped to ensure Genghis Khan's military dominance. Due to their advantages such as being lightweight and strong, many of the great advancements in composites were the result of war needs. For example, a Japanese sword made of soft iron sandwiched between steel has good resistance to flexure and impact [2]. The modern decade the marking point in the evolution of the composite has been associated with the development of carbon and boron fibers in the 1960s. In 1961, the first carbon fiber was patented and several years later became commercially available. Since the 1970s there has been a significant increase in the use of composites in aerospace, defense, nuclear, automotive, and marine (boats, yachts) industries. Composite structures and/or components can be found in wind energy systems, pressure vessels, sports goods (golf clubs, tennis rackets, bicycles, and surfing), and biomedical products [3].

Composites are materials that are composed two or more constituent parts resulting in a product with superior properties compared to its elements [4, 5]. One is generally a hard, stiff, and strong dispersed phase known as reinforcement, which is embedded within a softer bulk phase called the matrix. The reinforcement can be in the form of particles, fibers, whiskers, etc., and are commonly made from glass, carbon, aramid or metallic compounds while the matrix is either a polymer, metal, or ceramic. The matrix protects the reinforcement from abrasion or chemical reactions, keeps the fibers in place, distributes a load, and determines a service temperature of a composite material. While such elements retain their characteristics when joined to form the composite, they also influence the resulting properties of the material. More recently, the term 'advanced composites' has been used to describe materials fabricated from sheets of pre-impregnated fibers in a suitable resin matrix [4-7]. These sheets, which are also

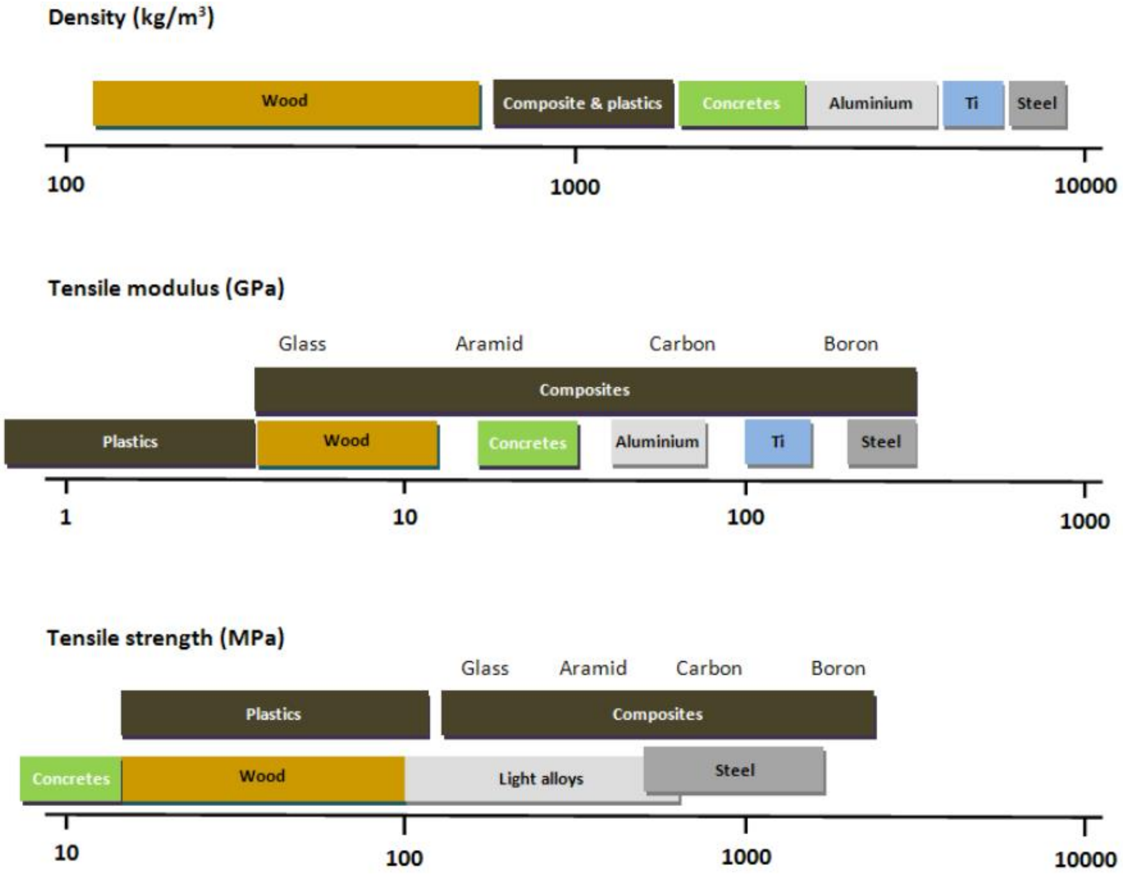

Figure 1.1. Mechanical properties of various metals and composites [6]

known as prepregs or plies, are typically 100-150 μm thick. The main advantages provided by advanced composites are high strength/stiffness to weight ratios resulting in significant weight reduction, superior rigidity, and damping, tailorable characteristics to satisfy loading requirements, and near-net-shape formability. They are particularly attractive for components in the aerospace and automotive fields.

For example, the use of composites is expanding in the civilian aircraft industry where approximately 50% of the total weight for the new Boeing 787 Dreamliner is made from composites compared to less than 5% in the Boeing 757/767 produced in the 1980s [8]. Similarly, CFRP accounts for 22-25% (35 tons) of the structural weight of the new Airbus A380, which is estimated to provide a 12% reduction in fuel consumption.

A comparison between properties of various materials including conventional metals and composites is presented in Figure 1.1. Composites provide the advantages of lower weight, greater strength, and higher stiffness.

Although the fabrication of the composite based parts produces near net shape products, various machining operations including edge trimming, drilling, milling, turning, etc. are often still necessary to meet part quality requirements and assembly needs. Moreover, the machinability of composites differs from conventional materials and their alloys in many aspects such as chip formation, cutting tool requirements, and operating parameters [9-11]. This is primarily due to the non-homogeneous and anisotropic nature of composites as well as the dissimilar mechanical and thermal properties of the reinforcement and matrix [11-13]. For example, the different thermal expansion coefficients of the fibers and matrix materials in composites can result in thermal stresses causing deformation with a possibility of part damage. Separation of surface layers can also occur due to low interlaminate strength and high cutting forces [14]. Such detrimental forces can be reduced through the proper selection of tool geometry, tool material, and cutting parameters [8]. Also, an abrasive effect of hard fibers in composites always leads to severe tool wear and, consequently, short tool life. Furthermore, when cutting tool conditions deteriorate due to wear and tear, the composite workpiece tends to show material-specific defects, such as delamination, burrs, and tearing of fibers. Based on the mentioned composite machining problems, it is known that composites are difficult-to-cut materials.

Nevertheless, the industries promote significant interest to develop novel, cost-effective approaches for composite machining and enhance their profitability in various manufacturing fields. This study, therefore, focuses on the research and development the novel approaches for improving composite cutting performance.

1.2 Overview of composite materials

1.2.1 Classification of composite materials

Composites are generally classified according to the matrix system used and can be broadly divided into metal matrix composites, ceramic matrix composites, or polymer matrix composites. Alternatively, they can also be categorized based on their reinforcement format/arrangement which typically involves particles, whiskers, fibers (continuous, discontinuous, aligned, and random), and structural arrangements, as shown in Figure 1.2 [4].

Metal matrix composites (MMC) are capable of providing higher temperature operating limits than their only metal-based counterparts [15]. Metals such as aluminum, copper, nickel, magnesium, steel, titanium, or their alloys can be strengthened with continuous carbon, boron, and silicon fibers or particle reinforcement, such as silicon and boron carbides. Fabrication of such composites is achieved by wetting fibers in the molten metal or infiltration of a preform by liquid metal under pressure [5].

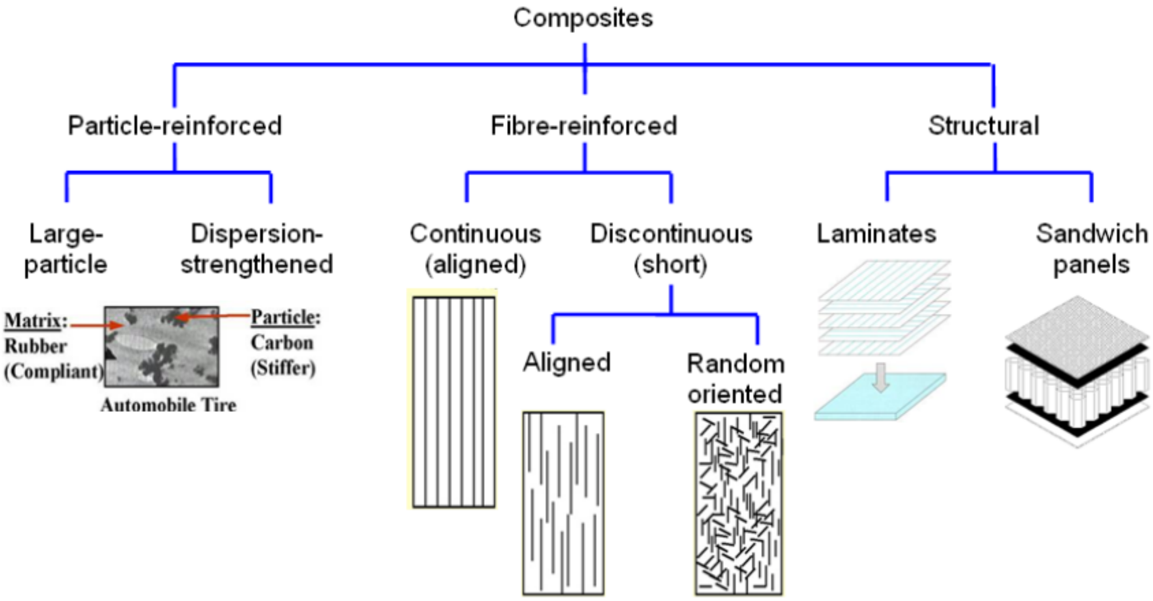
Composites
Particle-reinforced
Fibre-reinforced
Structural
Large-particle
Dispersion-strengthened
Continuous (aligned)
Discontinuous (short)
Laminates
Sandwich panels
Matrix: Rubber (Compliant)
Particle: Carbon (Stiffer)
Automobile Tire
Aligned
Random oriented

Figure 1.2. Classification for various composites according to reinforcement format [4]

Compared with CMCs and PMCs, the benefits of MMCs include non-flammability, resistance to degradation by organic fluids, and high thermal/electrical conductivity. The main disadvantage of the MMCs is corrosion led interfacial degradation at the fiber/matrix interface. The MMCs have been used in automotive, aerospace, and other applications. Some automotive applications include pistons and their ring inserts, engine block body, connecting rods, brake calipers, etc. In aerospace, MMCs are used for applications such as structural rods for space platforms, satellite antenna masts, aircraft stiffeners, and various joints and fittings.

Ceramic matrix composites (CMC) have higher specific modulus and mechanical properties than metals at elevated temperatures which allow their use up to 2000 °C, although applications are limited because of inherent brittleness [4]. Reinforcement with SiC or carbon fibers can significantly improve the fracture toughness of CMCs. Glass, MgO, Al_2O_3, Si_3N_4, AlN, and ZrO_2 are ceramic materials typically used as matrix materials. Usually, ceramic matrix materials are solid powders before they are formed into composite materials. The whiskers or the fibers are usually blended with the powder and then pressed to form a preform. The preform is then heated, and the ceramic particles consolidate with each other and with the reinforcements in a process called sintering. The most inviting applications for the CMCs are high-temperature environments and where high stiffness is required. The ability of CMCs to withstand high-temperature environments has led to their use in aerospace and defense applications, as shields for space re-entry vehicles, nose cones, engine parts, especially turbine blades, and in areas where exhaust gases are restricted.

Polymer matrix composites (PMC) consist of a polymer resin as the matrix, with fibers as the reinforcement. This group of composites will be discussed further in Section 1.3.

Dispersion strengthened composites comprise small particles (approximately 10^{-5} mm to 10^{-4} mm in diameter) which are added to the matrix material. These particles help the matrix resist deformation and result in a harder and stronger material. With large-particle reinforced composites, the particle diameter is typically in the order of several micrometers and carries a major fraction of the load. The automobile tire is an example of this configuration, which has relatively large carbon particles embedded within a polymer matrix. Whiskers are anisotropic single crystals typically fabricated by chemical vapor deposition (CVD) and have length/diameter ratios of 10 – 100, where the diameter is typically between 0.1 – 1 μm. Particles and whiskers are mainly used with MMCs and CMCs because they distribute randomly to retain the composite's isotropic nature.

Fibers currently used for engineering applications have a comparatively long axis and are often circular (up to several tens of micrometers in diameter) and have greater mechanical properties along the length axis. Fiber reinforced composites will be described in more detail in the following section.

Structural composites are typically fabricated by stacking multiple layers of fiber-reinforced plastic sheets to produce a homogeneous material known as laminates. The laminate properties depend on the individual layers as well as the fiber orientation of the different layers of the structure. Laminates are occasionally used to create sandwich panels containing a honeycomb structure.

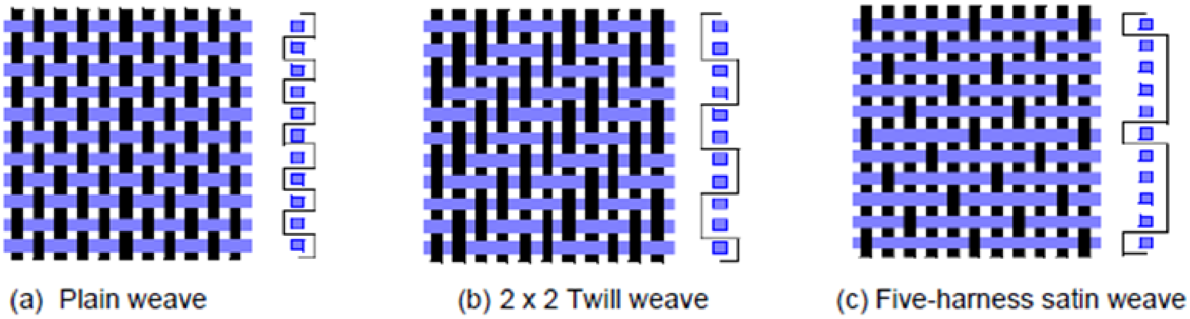

Figure 1.3. The most commonly used fabric types [6]

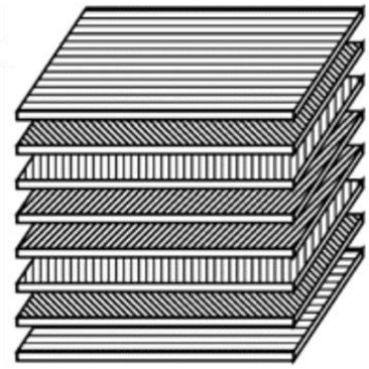

Figure 1.4. Example of stacking sequence in multidirectional layup [16]

1.2.2 Fiber-reinforced plastic (FRP) composites

PMCs are often referred to as fiber-reinforced plastics (FRPs) when strong and brittle fibers are incorporated within a ductile and soft polymer matrix [12].

Continuous fibers in the form of unidirectional (UD) or woven fabrics are the principal fibrous patterns in FRP composites. The term unidirectional refers to the material having fibers arranged in a single direction while woven structures involve perpendicularly intersecting fibers. Woven fabrics include plain weaves when each fiber yarn passes over and under every other perpendicular yarn, twill weaves and satin weaves as presented in Figure 1.3. Both UD and woven plies can be laid up to produce multidirectional composite laminates as shown in Figure 1.4.

Carbon, glass, and aramid are the most common types of fibers used in PMC, where the letters C, G, or A are placed before the acronym FRP to specify the nature of the reinforcing fibers [12]. Boron and polyethylene fibers are also used for FRP composites although to a less extent. General mechanical properties and relative cost information for the various individual fibers are shown in Figure 1.5.

Fibers are typically produced by drawing liquid material or pulling a precursor through an orifice. They are subsequently supplied in the form of tows consisting of individual continuous fiber filaments, which generally contain a bundle of between 3,000 to 30,000 filaments.

Glass fibers were first introduced in the 1930s and are widely used as the reinforcement material for polymer matrix composites. The most common types include E-glass (electrical), S-glass (high strength and stiffness), and C-glass.

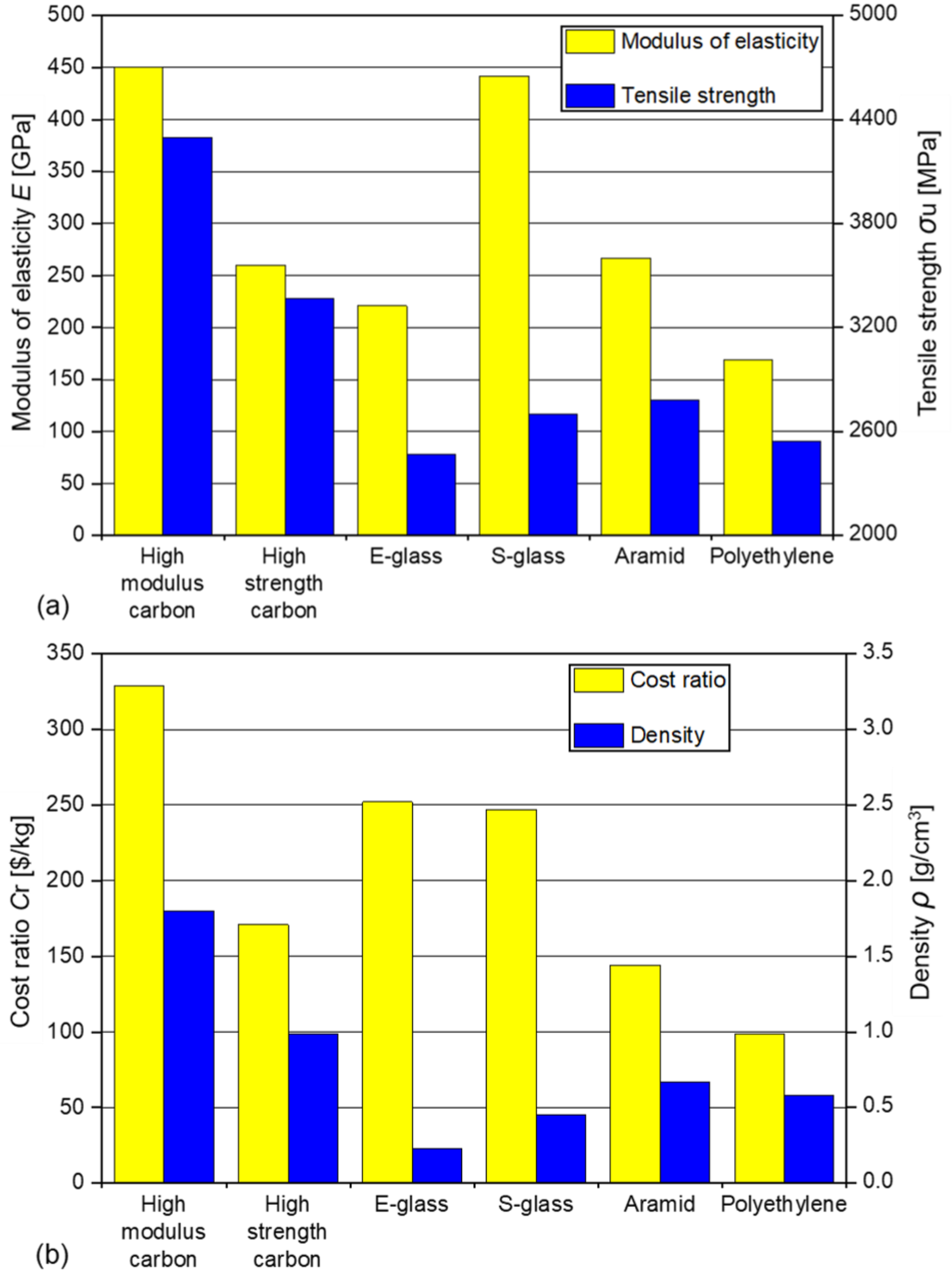

Figure 1.5. Relative properties for various individual fibers [6]

The S-glass fibers are used for aerospace applications, while C-glass fibers are used in applications requiring corrosion resistance, such as marine and chemical industries. The glass fibers have excellent chemical resistance as well as low cost compared to other fibers, but their

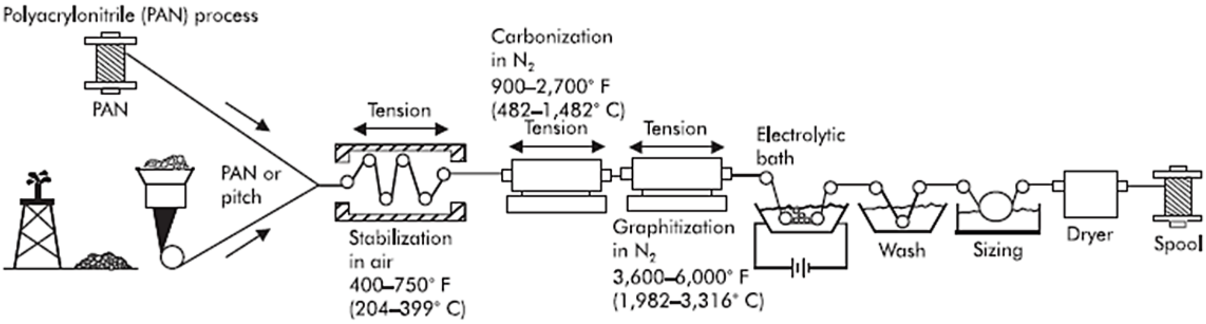
Polyacrylonitrile (PAN) process
PAN
PAN or pitch
Tension
Stabilization in air 400–750° F (204–399° C)
Carbonization in N$_2$ 900–2,700° F (482–1,482° C)
Tension
Tension
Electrolytic bath
Graphitization in N$_2$ 3,600–6,000° F (1,982–3,316° C)
Wash
Sizing
Dryer
Spool

Figure 1.6. Manufacturing process for making carbon/graphite fibers [5]

limitation is service temperature which is below 200 °C [4]. Additionally, they have higher density and lower tensile strength in comparison to carbon fibers. Also, the glass fibers are highly abrasive, and adversely affect the machinability of GFRP composites.

Aramid fibers were introduced early in the 1970s. They are characterized by high tensile strength and tensile modulus (σ_u = 3720 MPa and E = 63-143 GPa) together with low density (~1.44 g/cm^3) [5]. Stiffness can reach 125 GPa and although very strong in tension, they have very poor compression and shear properties. In addition, aramid fibers can save their mechanical properties between -200 to 200 °C. These fibers are used in a polymer matrix and the most common commercial name is Kevlar. Typical applications of aramid fibers include bulletproof vests and battlefield shelters, the leading edge of aircraft wings, clutch linings, and pressure vessels. Cutting of aramid fiber composites requires tools to have a high degree of edge sharpness and a small cutting edge radius as they are capable of sustaining large deformation in bending with subsequent spring-back causing fuzzing of the machined surface [8].

Carbon fibers were first introduced in the 1960s [7]. In addition to having a low density (~1.6 g/cm^3), they have a wide range of moduli and tensile strengths which can be up to 3 times the stiffness of steel and 15 times the strength of construction steel [17]. These fibers are considered the most important material for reinforcement because it possesses the highest specific strength/modulus among all fiber materials. Commercial carbon fibers are created when polyacrylonitrile fibers (PAN), pitch, or cellulose (Rayon) are carbonized through oxidation and following thermal pyrolysis at high temperatures. Figure 1.6 shows the typical steps used in making PAN-based carbon fiber. The fibers are first drawn and oxidized in air to crosslink them, then they are carbonized in a nitrogen atmosphere. This ensures the removal of non-carbon atoms and creates fibers that consist of carbon only. Graphitization is further carried out to improve the purity and crystallinity of the fibers. After graphitization, surface treatment and size are applied. Carbon fibers are anisotropic and their properties are affected by the degree of orientation of the graphite layers concerning the fiber axis. Graphite layers are based on hexagonal rings of carbon in which carbon atoms are held with a strong covalent bond. Secondary bonds hold the graphite layers together, which provides slip along the hexagonal planes [5]. A higher temperature of graphitization promotes the orientation of the graphite layers in the fiber direction and thus resulting in a higher tensile modulus.

Carbon fibers are broadly classified into three categories, namely general purpose (GP), high performance (HP), and activated carbon fibers (ACF) [17]. The GP and HP types are characterized by an amorphous and isotropic structure. Contrary, activated carbon fibers have a large number of open micro-pores that can act as adsorption points limiting their use. They are utilized to produce environmental protection equipment such as water treatment units and gas masks. Table 1.1 details the properties of the different carbon fiber types, while Table 1.2 presents the properties of carbon fibers classified according to their tensile strength and strength/modulus ratio.

In FRP composites, the matrix is used to support and bond the reinforcement phase, transmit and distribute external applied loads to the reinforcement, control chemical, and electrical composite properties and prevent any crack propagation [2-5]. In addition, as the matrix normally softens, melts, or degrades at a lower temperature than the fibers, it defines the maximum operating temperature for the composite part. It means that PMCs cannot be used near or above the glass transition temperature (*T*g), at which many of its physical properties change or degrade [5]. The matrix phase can be pure or mixed with other additives to improve its mechanical properties and allowable operating temperature.

Two groups of matrix materials commonly employed in FRP composites are thermoset polymers (e.g. polyester, epoxy) and thermoplastic (e.g. polyamide, PEEK).

Thermosets are materials that undergo a chemical reaction or curing and normally

Table 1.1. Properties of various carbon fiber types [17]

Type	**Tensile modulus (GPa)**	**Strength to modulus ratio %**
UHM (ultra high modulus)	> 500	-
HM (high modulus)	> 300	< 1
IM (intermediate modulus)	< 300	> 1
LM (low modulus)	< 100	Isotropic structure
HT (high strength)	Tensile strength > 3 GPa	1.5 - 2

Table 1.2. Classification of carbon fibers based on their tensile strength and modulus [17]

Type	**Diameter (μm)**	**Tensile strength (MPa)**	**Tensile modulus of elasticity (GPa)**
General purpose (GP)	(7 – 15)	700	40
High performance (HP pitch)	(9 – 11)	5000	350
High performance polyacrylonitrile (HP PAN)	(4 – 8)	2000	200-800
Activated carbon fibres (ACF)	(7 – 15)	200	1500

transform from a liquid to a solid. In its liquid form, the material has unlinked monomers. The addition of a second material as a curing agent, catalyst, and/or the presence of heat will initiate the chemical reaction. During this reaction, the molecules cross-link and form significantly longer molecular chains and cross-link networks, causing the material to solidify. The change of the thermoset state is permanent and irreversible. Thermosets remain rigid when heated and are quite strong and stiff but exposure to high heat will cause the material to degrade, not melt [12]. The polyester matrix is used due to its lower cost but is mainly employed in glass fiber composites. With carbon fiber-based products, epoxies are usually selected for their lower shrinkage on curing, which allows for high fabrication accuracy, mechanical properties, and environmental resistance.

Contrary to thermosets, thermoplastics are melted process-able plastics. When heat is added to bring the temperature of the plastic above its melting point, the plastic melts, liquefies or softens enough to be processed. When the heat source is removed and the temperature of the plastic drops below its melting point, the plastic solidifies back into a solid. This process can be repeated.

Both thermoset and thermoplastic materials have their place in the market. Thermosets provide easy wetting of reinforcing fibers and easy forming to final part geometries than thermoplastics. On the other hand, thermoplastic polymers offer an easy solution to recycling composite components. Within the composite market, thermoset represents about 80% of the total material used [3].

Table 1.3 details various mechanical properties for the most commonly used CFRP composites against equivalent Glass fiber reinforced polymer (GFRP) and Aramid fiber reinforced polymer (AFRP) composites. Based on the presented data, it can be concluded that CFRP composites provide beneficial mechanical properties such as low density, strength, and modulus of elasticity over other compared FRP composites. However, the high cost of the CFRP products may be expected.

Nevertheless, today CFRP based composites are one of the perspective advanced materials. Aerospace projects have been the primary drivers of the CFRP industry for most of their history. Recently, CFRP composites became basic structural material in the development of electric vertical take-off and landing (eVTOL) aircraft and unmanned aerial vehicles with electric propulsion systems. Therefore, aerospace applied CFRP composite is the choice for this study, as a workpiece material in cutting performance investigation.

Table 1.3. Mechanical properties for the common CFRP laminates against GFRP and AFRP composites [12]

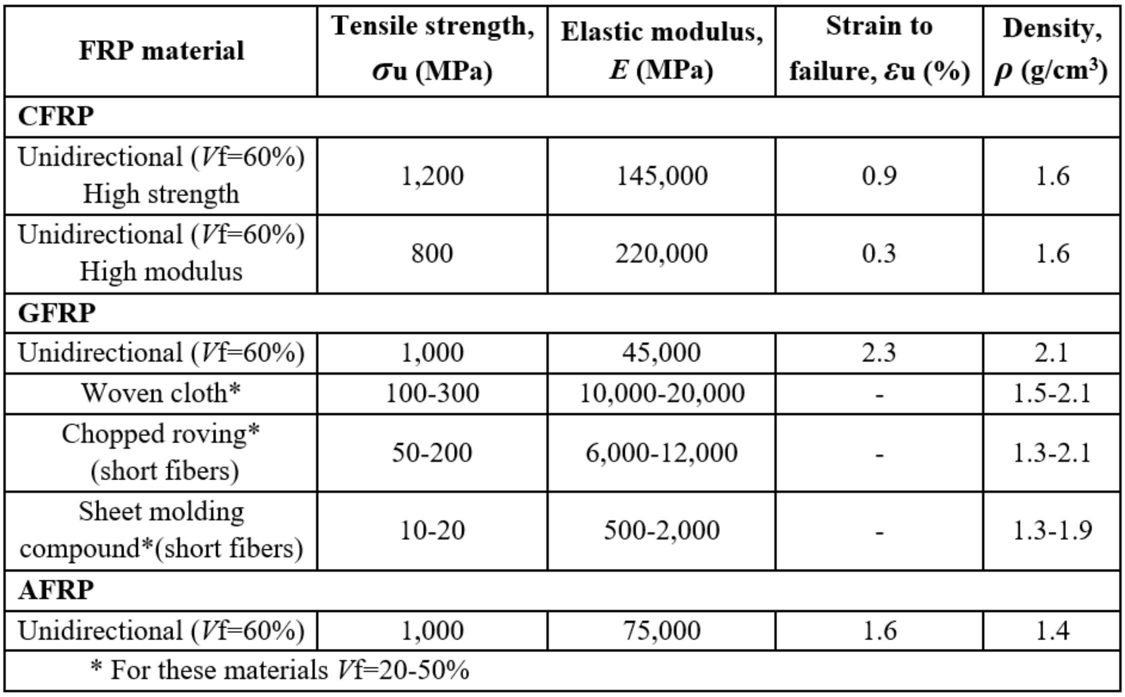

FRP material	Tensile strength, σu (MPa)	Elastic modulus, E (MPa)	Strain to failure, εu (%)	Density, ρ (g/cm^3)
CFRP				
Unidirectional (*V*f=60%) High strength	1,200	145,000	0.9	1.6
Unidirectional (*V*f=60%) High modulus	800	220,000	0.3	1.6
GFRP				
Unidirectional (*V*f=60%)	1,000	45,000	2.3	2.1
Woven cloth*	100-300	10,000-20,000	-	1.5-2.1
Chopped roving* (short fibers)	50-200	6,000-12,000	-	1.3-2.1
Sheet molding compound*(short fibers)	10-20	500-2,000	-	1.3-1.9
AFRP				
Unidirectional (*V*f=60%)	1,000	75,000	1.6	1.4
* For these materials *V*f=20-50%				

1.2.3 Description of CFRP composite components

The basic element of a continuous fiber composite part is a single unidirectional layer or ply, which behaves orthotropically [5]. Usually, the properties of an individual layer are identified by the material supplier.

Laminates are typically fabricated by stacking unidirectional or woven fabric layers at different fiber orientations according to the planned application [2]. For *N* layer laminate, each ply has a distinct fiber orientation which is numbered from the top surface. The laminate is coded according to the angles of the reinforcing fibers within the plies from a reference axis (0°), with either (+) and (-) signs representing the orientation of a single ply on the stack from the reference axis. The designation used for describing the stacking sequence of a FRP laminate includes brackets, parentheses, slashes, and subscripts. Brackets “()” are used to indicate all the fiber orientations present within a laminate in accordance with the stacking sequence, while slashes “/” are used to separate layers or groups of layers in a particular direction, and the subscript *s* (outside the brackets) denotes a symmetric laminate. For instance, UD laminate layup, shown in Figure 1.7, can be described as (0/+45/-45/90/-45/+45/0) started at the top surface.

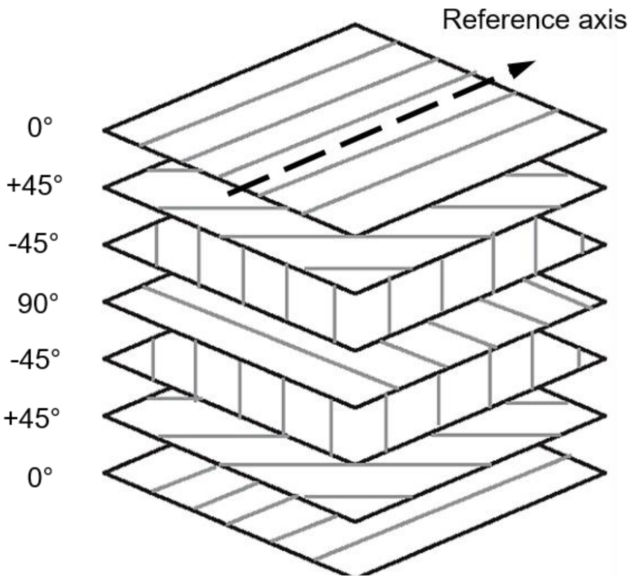

Figure 1.7. Different possible ply orientation for UD laminate layup

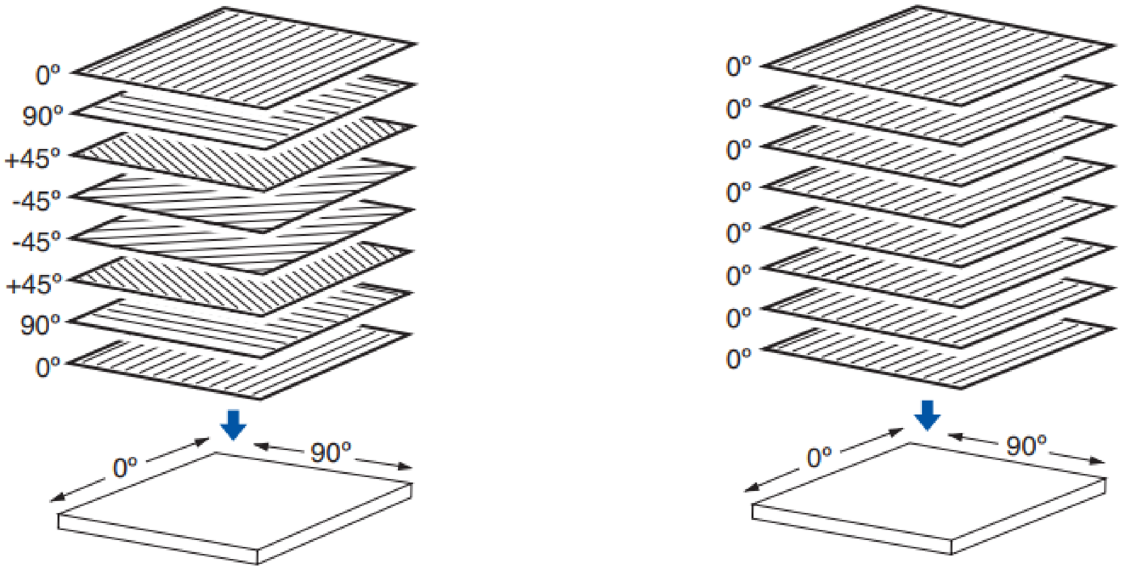

■ Quasi-isotropic lay-up

■ Unidirectional lay-up

Figure 1.8. Quasi-isotropic vs. unidirectional lay-up [18]

Symmetric laminate should have an even number of plies with only half the layers quoted. For example, (02/90/90/02)s refers to a laminate consisting of 12 plies, the first in the 0° orientation and repeated twice and the laminate is symmetric concerning a middle plane. If the laminate has an equal number of plies at each principal fiber orientation, e.g. (0/45/-45/90)s, it is known as a quasi-isotropic laminate structure, as shown in Figure 1.8.

1.2.4 Manufacturing of CFRP composites

As mentioned previously, various methods can be used for the manufacture of advanced composite components including vacuum bag molding, autoclave molding, filament winding, press molding, pressure bag molding, thermal expansion molding, and pultrusion [8]. Prepreg lay-up is used to produce high-performance composites. The process can involve manual hand lay-up (HLU) or automatic layup using a robot or CNC machine as in the automatic tape laying (ATL) process. The prepregs require a vacuum bag and curing in an autoclave to harden the matrix. The curing process can be done in an oven for marine and railway applications while highest-performance aerospace composites are cured in an autoclave [8]. Inspection of fiber reinforced composite parts typically focuses on the fiber arrangement and defects such as matrix cracks (e.g. voids, porosities), fiber cracks, interface cracks, delamination, or inclusions which may significantly affect its properties [17]. Inspection methods include metallographic examination, X-ray analysis, infrared thermal imaging, and the C-scan techniques.

1.3 Drilling of CFRP composites

1.3.1 Introduction

Conventional machining of CFRP composites requires tools with sharp cutting edges to cut abrasive fibers effectively, while relatively low operating parameters are specified to achieve the required surface quality and limit cutting temperatures [8]. Among the conventional machining methods, drilling represents one of the most important machining operations that are carried out on composites.

Drilling, with following countersinking and reaming, is the most frequently used process for preparing composite parts for joining and assembly, especially in the aerospace industry. It is a known fact that more than a hundred thousand mounting holes on a single small aircraft and more than a million holes on larger ones. Moreover, manufacturers reported that about 40% of the material removal volume is done by drilling operations in the aerospace industry [9]. Consequently, hole production is a key process in composite manufacture with drilling normally conducted as a final operation.

Despite its extensive use, drilling also remains one of the most challenging machining operations. Among the key issues to be considered are thermal management, tool wear, and delamination. Since poor hole quality accounts for an estimated 60% of all part rejections [9], considerable attention should be paid to all factors affecting the drilling of the composite material.

For comparison, milling is a lower-used material removal process in manufacturing composite parts, unlike the milling of metals. The reason is that CFRP components are largely made near net shape and any subsequent milling is limited mainly to deburring and edge trimming to achieve contour shape accuracy.

In addition to conventional drilling operations, several developed high-performance drillings and non-conventional machining processes show promising results.

Vibration-assisted drilling (VAD) has received great interest in past few years by both academic and industries. Based on conventional drilling system, a low (<1000 Hz) or high (>1000 Hz) frequency and low amplitude vibration is imposed on a drill along the feed direction during drilling [19]. Therefore, VAD is a pulsed intermittent cutting process, while conventional drilling is a continuous cutting process. As a result, a reduction of thrust force and an improvement of chip evacuation can provide a decrease in delamination during VAD. Indeed, on the same drilling conditions, the thrust force induced by VAD are reduced by 20–30%, compared with conventional drilling [20, 21]. Also, reduction of about 50% of delamination area, as well as better circularity and surface roughness, were achieved in this process [22]. Although VAD is promising CFRP drilling technique, industrial application of VAD requires market available machining centers equipped oscillation systems and etc. Nowadays, such kinds of the equipment are absent on a market.

A number of researchers have investigated the feasibility of using water jet machining for the cutting of FRPs. This machining uses an erosion mechanism by water jet under high pressure with abrasive slurry which cuts the target composite material. Until to date, abrasive water jet (AWJ) machining has been the only method used in industry for trimming CFRP composite materials among non-conventional machining processes like laser cutting, ultrasonic machining, etc. due to its small sensitivity to material properties, and flexibility [23]. Also, the obvious advantage is the lack of thermal damage however, severe delamination and chipping are still present at the hole exit [24, 25].

Laser machining is a noncontact machining process, which has a good application prospect in CFRP drilling because of its advantages of low stress, small damage, high precision, etc. However, due to the sensitivity of the CFRP resin matrix to the heat, the formation of a heat-affected zone (HAZ) around the hole is the main limitation of laser cutting, which influences the matrix recession, distortion of fibers, and delamination [26, 27]. Also, the machining taper exists, which affects the depth drilling ability in CFRP components. Recently, a promising picosecond laser “double rotation” cutting technique was proposed by Ouyang et al. [28]. The results show that there is no interlaminar tearing, cracks, or burrs on the cutting section, and the

HAZ was significantly reduced.

Nevertheless, this study is focused on the cutting performance of CFRP will be discussed with emphasis on conventional drilling to highlight research trends.

1.3.2 Drilled hole quality

Hole quality is one of the most important measures when assessing drilling performance because it influences the service life of composite parts post assembly. First, König and Graß [14] described a methodology for assessing hole quality by classifying defects commonly associated with drilled holes in FRP, as shown in Figure 1.9. Here, quality criteria include cracks, damage to surface layers, damage within a peripheral zone, workpiece surface roughness, hole roundness error, and dimensional errors. Similarly, Abrão et al. [29] reviewed the main hole quality defects, which include surface delamination, fiber pullout, and insufficient surface roughness when drilling CFRP. Damage to surface layers is further divided into spalling, edge chipping, delamination, and fuzzing. Tool wear, the presence of powdery chips, workpiece surface delamination, internal delamination, fiber pullout and decreased flexural strength significantly affect composite part strength and fatigue life. Whereas spalling was observed as

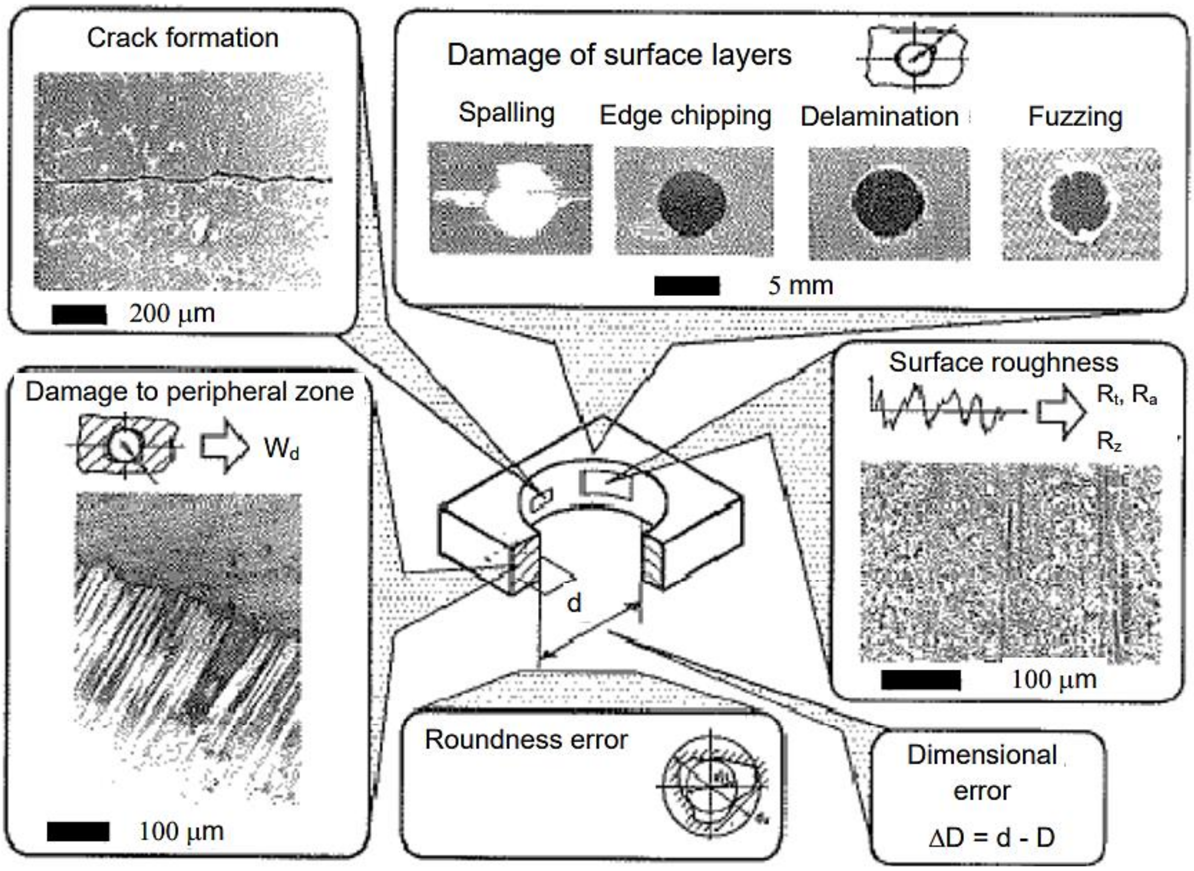
Crack formation
200 μm
Damage of surface layers
Spalling
Edge chipping
Delamination
Fuzzing
5 mm
Damage to peripheral zone
W_d
100 μm
Surface roughness
R_t, R_a
R_z
100 μm
d
Roundness error
Dimensional error
ΔD = d - D

Figure 1.9. Quality criteria when drilling FRPs [14]

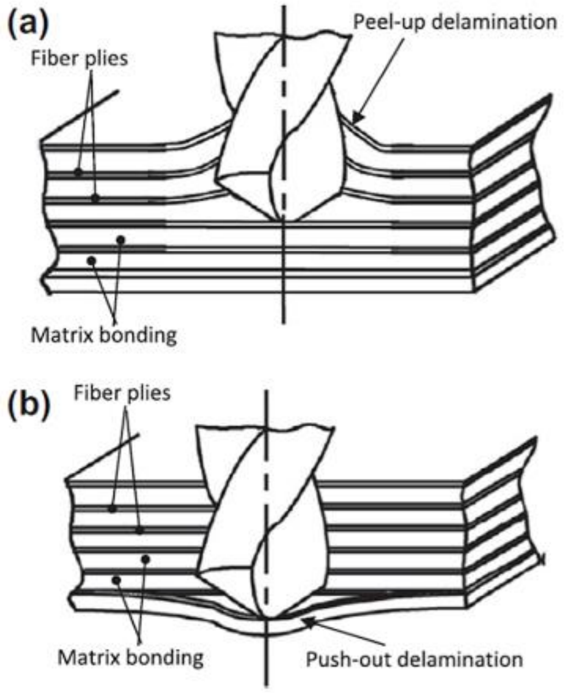

Figure 1.10. Delamination forms: (a) peel-up at entrance and (b) push-out at exit [16]

the primary hole defect in a study by Zhang et al. [30], surface delamination was reported to be the dominant damage criterion when drilling CFRP in a number of other publications [9, 30-34]. Delamination is generally acknowledged to be the main reason for stiffness/strength reduction in composite structures leading to catastrophic failure of the laminate under bending or shear loading conditions [29]. Therefore, evaluation of drilling-induced delamination is important for delamination control and reaching the required hole quality.

Delamination can take two different forms, either push-out at the hole exit and/or peel–up at hole entry, as illustrated in Figure 1.10. Peel-up occurs at hole entry when the tool pulls away from the upper layer of the composite laminate resulting in separation and the formation of an entry delamination zone. As the drill approaches the bottom end of the hole, the uncut laminate thickness is not able to resist deformation and the tool acts like a punch that separates the thin uncut layers from the remainder of the laminate. Subsequently, push-out delamination initiates at the hole exit when the thrust force exceeds the interlaminar bond strength of the material.

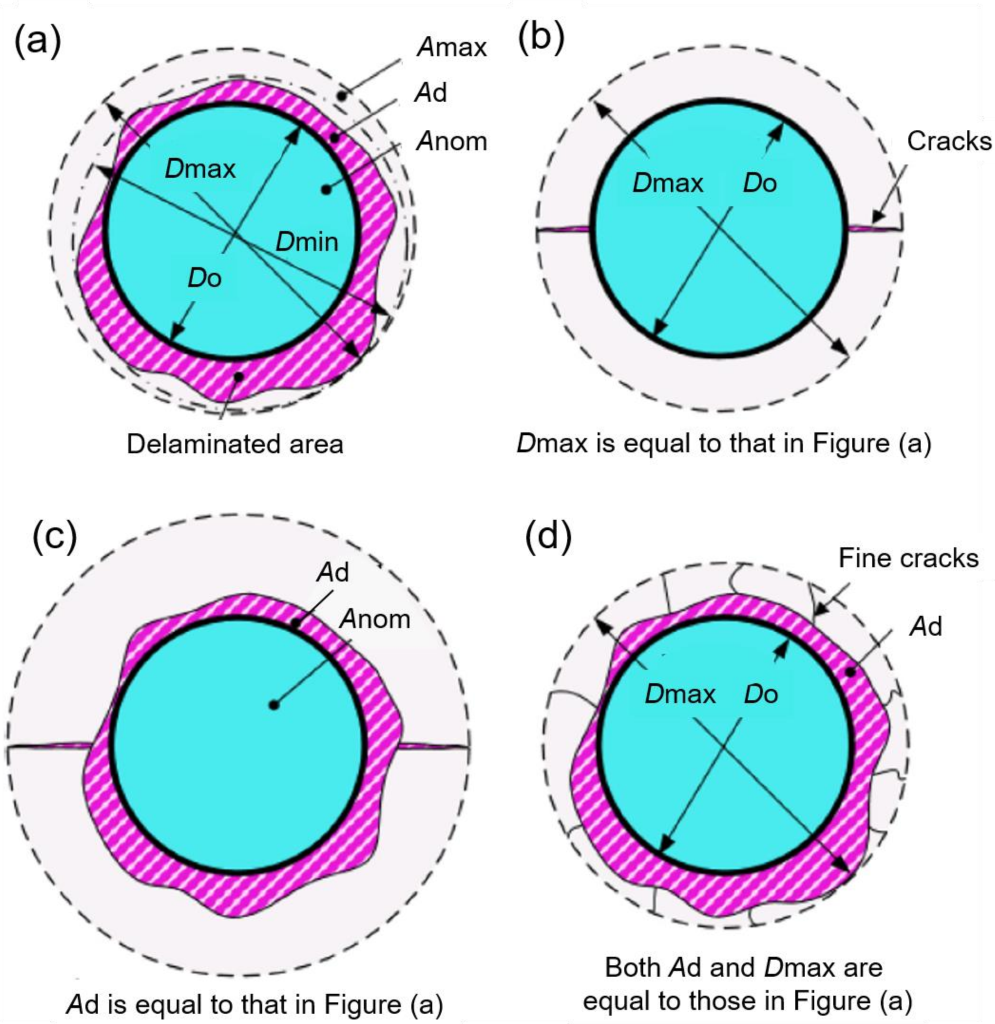

*D*max is equal to that in Figure (a)

*A*d is equal to that in Figure (a)

Both *A*d and *D*max are equal to those in Figure (a)

Figure1.11. Diagram of the delamination damage: (a) uniform damage, (b) cracks, (c) uniform damage with cracks and (d) uniform damage with fine cracks [34]

The most used delamination evaluation method was proposed by Chen [35]. The delamination factor *F*d is defined as the ratio of the maximum diameter of the damaged area (*D*max) to the nominal diameter of the hole (*D*o), and two circles are concentric, as illustrated in Figure 1.11(a). This delamination factor presents satisfactory results when delamination possesses a regular pattern. However, if the delamination presents ruptures and fine cracks, the delamination factor might not be appropriated due to the lack of indication of the delamination area during calculation. Indeed, comparing Figure 1.11(a) with (b), it can be observed that the same *F*d is recorded for two distinct conditions with the same *D*max. However, it is obvious, that the former condition is more damaged. Afterward, Da Silva [34] proposed a similar assessment parameter named the minimum delamination factor (*F*dmin). This delamination factor is calculated by a ratio of the diameter of the minimum delamination area (*D*min) to the

*D*o, whereas the two circles may not be concentric, as shown in Figure 1.11(a). This approach can accurate the delamination factor results when the delaminated area does not locate around the drilled hole uniformly. On the other hand, it ignores the damage area contribution in the delamination assessment as well.

Faraz et al. [36] proposed a Two-dimensional delamination factor (*F*a). It is defined as the ratio of the delamination area (*A*d) to the nominal hole area (*A*nom) and is expressed as a percentage, as shown below:

$$F_a = \left(\frac{A_d}{A_{nom}}\right)\% \tag{Eq.1}$$

The *F*a seems to be better than mentioned above delamination factors due to the consideration of the delamination area. However, it is still not accurate when the delamination damage occurs accompanied by long cracks, as shown in Figure 1.11(c).

In order to improve the accuracy of delamination assessment, several combination parameters were proposed [34]. One of them is the adjusted delamination factor (*F*da) which is proposed by Davim et al. [37] and calculated as shown below:

$$F_{da} = F_d + \frac{A_d(F_d^2 - F_d)}{A_{max} - A_{nom}} \tag{Eq.2}$$

Where *A*max is the area corresponding to *D*max. The adjusted delamination factor is designed to take account of both the contributions of the maximum crack length and damage area. The adjusted delamination factor indeed appears to be more accurate than the earlier mentioned delamination factors. However, it may still be inaccurate in some special cases where many fine cracks occur, as illustrated in Fig. 1.11(d).

The aforementioned delamination factors are limited to the quantification of an in-plane delamination extent. With the advances in non-destructive delamination detection technologies (e.g. ultrasonic scanning by an acoustic microscope), the delaminated damages inside the inner composite layers can be easily and accurately measured. Recently, Xu et al. [38] proposed a new delamination factor (*F*v) capable of quantifying the interlaminar delamination inside a composite laminate based on the *F*a. This novel delamination factor is defined as the cumulative volume (*V*d) to the nominal hole volume (*V*nom) of the delaminated layers to be independent of the composite thickness.

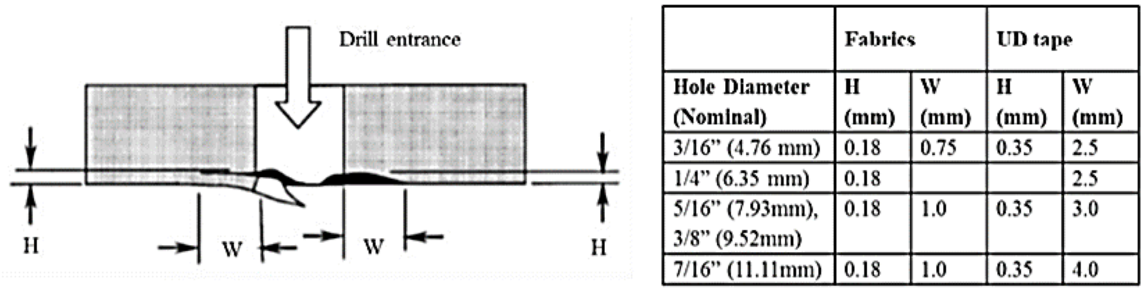

	Fabrics		UD tape	
Hole Diameter (Nominal)	H (mm)	W (mm)	H (mm)	W (mm)
3/16” (4.76 mm)	0.18	0.75	0.35	2.5
1/4” (6.35 mm)	0.18			2.5
5/16” (7.93mm), 3/8” (9.52mm)	0.18	1.0	0.35	3.0
7/16” (11.11mm)	0.18	1.0	0.35	4.0

Figure 1.12. Acceptable damage (courtesy of Bombardier Aerospace) [39]

The *F*v can be determined as follows:

$$F_v = \frac{V_d}{V_{nom}} = \frac{1}{p}\sum_{k=1}^{p}\frac{A_d^k}{A_{nom}} \qquad \text{(Eq.3)}$$

where *p* is the total number of the delaminated plies and *k* is the number of specific delaminated ply.

Nevertheless, there is no common agreement in assessing the delamination till now. Also, the mentioned above delamination factors are mainly used for drilling-induced delamination evaluation in the research fields.

From industrial points of view, determination of interlaminar failure and interfacial debonding among adjacent plies is important due to possible product rejection. This type of damage is often induced by the thermo-mechanical coupling effects following a drilling operation, occurring not only in the outermost layers of a composite but also inside the interior layers forming an out-of-plane imperfection because of its inherent capability to propagate across interlayer plies [38]. Therefore, a non-destructive diagnostic system is widely used for quality control of manufacturing products, especially in the aerospace industry. In the case of evaluation mentioned above peel-up and push-out delamination, breakout damage shall not exceed limits. For example, Figure 1.12 presented drilled hole damage limits applied for commercial product manufacturing.

Uncut fibers and fiber pull-out can occur on the machined edges of CFRP composites due to their elastoplastic recovery and bouncing-back effects while tearing is featured by fibers split from a hole periphery. Defects of these two types occur depending on the fiber cutting angle of an examined composite laminate, showing symmetrical distribution characteristics [31, 40]. Uncut fibers usually do not negatively impact the mechanical properties of machined CFRP parts, but they require additional machining operations and, consequently, cost in case of their elimination. The appearance of uncut fibers around the edge of the hole shows usually two burr

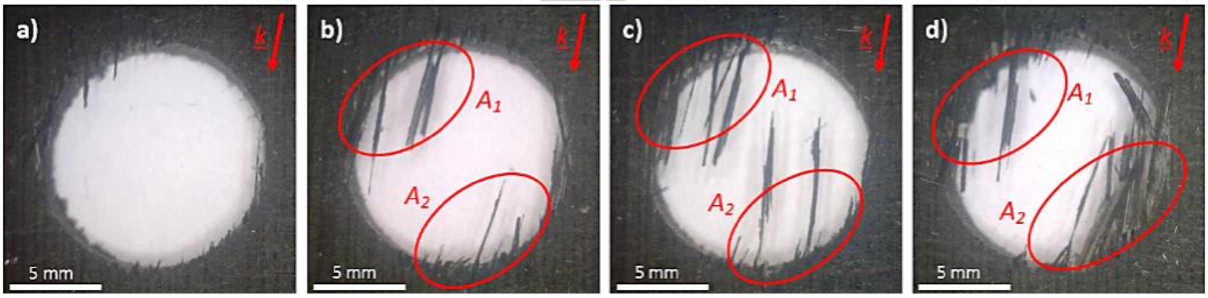

Figure 1.13. Uncut fibers at the exit of drilled holes in UD-CFRPs [42]

areas, can be observed at the exit of the hole where uncut fibers occur, as demonstrated by Xu et al. [41]. For instance, such uncut fibers at the exit of holes and their burr areas, named A1 and A2, can be seen in Figure 1.13.

1.3.3 Tool shapes, materials, and coatings applied for drilling of CFRP composites

1.3.3.1 Tool shapes

A cutting tool shape has one of the significant effects on the mentioned above CFRP damages. A wide range of different drilling tools is used in composite product manufacturing. The most common drilling tools applied in CFRP drilling are illustrated in Figure 1.14.

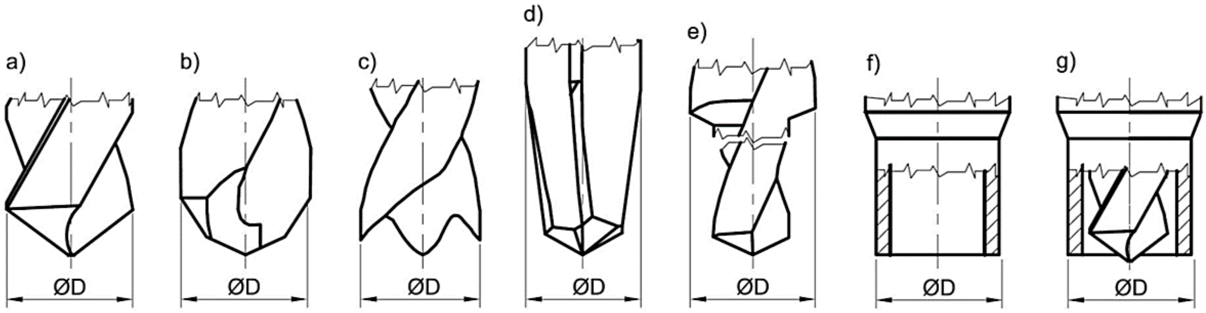

Figure 1.14. Schematic drawings of different drilling tools for CFRPs: (a) conventional twist drill, (b) double point angle twist drill, (c) brad & spur drill (candlestick drill), (d) dagger drill (one-shot drill), (e) step drill, (f) core drill and (g) the special core drill [42]

Point angle is one of the key angles for conventional twist drill, presented in Figure 1.14(a). An increase in point angle leads to an extrusion effect on the uncut layers of the laminates and consequently increases higher thrust force, which may provide delamination and the appearance of uncut fibers on machined surfaces. Therefore, it is considered that the point angle of the twist drill has a main effect on drilled hole quality. Gaitonde et al. [43] reported that the delamination factor at the hole exit was reduced up to 45% by using a lower point angle of 85°. Also, Heisel and Pfeifroth [44] reported a small point angle of a twist drill can reduce the push-out delamination for CFRP laminates. However, the effect of point angle on peel-up delamination has a different tendency. Shyha et al. [33] achieved lower delamination at hole entry with an angle point of 140° rather than 118°. The application of low feed rates and optimized process parameters, such as cutting speed, etc., makes possible to drill holes with lower delamination. Presently, conventional twist drills still represent an industrial standard due to the comprehensive consideration of drilling performance and tool cost.

Double point angle twist drills, shown in Figure 1.14(b), produce lower thrust force and delamination, compared with conventional twist drills due to the presence of a second point angle. The second point angle could decrease the axial force and lead to the better wear resistance of outer cutting corners compared to previous ones due to a lower cutting force acting on the secondary cutting edges.

Brad & spur drills, presented in Figure 1.14(c), show excellent performance results as far as the delamination of the FRP materials is concerned. According to Su et al. [45], this is due to the cut-push effect of sharp flank cutting edges, when the drill first cuts the last layer of the composite and then pushes this layer off. As result, the number of uncut fibers, as well as delamination, can be minimized.

Dagger drill, frequently named as the one-shot drill, is a special double-point angle drill with straight flutes, as shown in Figure 1.14(d). The small point angle of the secondary edges reams the final surface of the hole. This drill shows low axial force compared to other drills. Therefore, one-shot drills show good results concerning push-out delamination and uncut fibers located at the exit of the holes. The cutting ability of such drills was investigated by a number of researchers [31, 32, 38, 41, 46, 47]. Recently, Jia et al. [48] proposed a novel intermittent - saw tooth drill based on the geometry of conventional one-shot drill. An upward cutting, was achieved by this intermittent – saw tooth structure to effectively reduce hole exit delamination. The number of high quality holes drilled by this novel drill is nearly 6 times of that by conventional one-shot drill.

Step drills, as shown in Figure 1.14(e) are designed on a step-control scheme: first, a pilot hole is drilled using a smaller diameter drill, then the final surface is reamed by applying a wider diameter tool [34]. In the scope of this process, the goal of the first step is to create a pilot hole quickly and efficiently, whereas the goal of the second step is to make the final surface of the hole causing minimal geometrical damage. The latter goal is feasible partly due to the low thrust force of the second drilling stage, according to Tsao and Hocheng [49]. With the application of step drills, the effect of the chisel edge can be minimized on delamination. Also, different diameters and countersunk shaped holes can be drilled using one single step drill. Although the step drill is a good choice for decreasing both entry and exit delamination, the ratio of the diameters of the first and second drilling steps is limited.

Core drill is a hollow grinding drill with a bonded diamond cutting surface, as can be seen in Figure 1.14(f). It directly machines the final surface of the hole by abrasive cutting. Due to the resulting small chip section during cutting, the thrust force is minimal, and consequently, entry and exit delamination are minimal as well. However, chip removal is a troublesome problem, as compared with helical flute drills. To resolve this problem of chip removal, conventional compound core-special drills are designed to avoid the chip removal clog in drilling, as shown in Figure 1.14(g). Conventional compound core-special drills can be considered as a combination of an outer drill, a directly core drill, and an inner drill, including various twist drills, saw drills or candlestick drills, etc. The main problem of special core drills is the kinematic constraint of the inner and the outer drills. The application of diamond grinds for the outer drill requires a higher cutting speed for effective machining compared with the inner drill ability. Such cutting speed leads to fast inner drill wear. As a solution to the problem, Tsao and Chiu [50] developed a novel experimental environment to combat the problem of relative motion and chip removal between the inner and outer drills. Nevertheless, special core drills based approaches for CFRP machining are not applied for the manufacturing of commercial products.

1.3.3.2 Tool materials

The choice of tool material is governed by several factors including workpiece specification, productivity requirements, product design, machine tool condition, and tooling cost. According to [8], tool materials more suitable for machining composites include cemented carbides and polycrystalline diamond (PCD).

Cemented carbide tools comprising hard carbide particles, mainly WC, are joined by a cobalt (Co) binder, which is generally in a liquid phase at the sintering temperature of above 1573 K [8, 51]. The cobalt content is typically between 4-12 %, depending on the grade of carbide. The mechanical and physical properties of WC-Co tool materials are highly dependent on the cobalt content and carbide grain size. In general, a smaller grain size results in higher hardness and wear resistance while both hardness and compressive strength also improve with lower cobalt content. Therefore, submicron/fine grain-sized carbides are preferred for the machining composites in order to withstand abrasion attacks from the reinforcement. On the other hand, it has been reported that WC-Co based cutting tools will be rapidly worn out, and perform very short tool lifetime. Their wear resistance still cannot meet the requirements of the long-duration machining of CFRP materials [52].

Synthetic polycrystalline diamond is produced by sintering diamond grits (2-50 μm) at high temperatures and pressures of 1773 K and 60 GPa respectively [51]. A metal catalyst, main cobalt, is used to promote diamond intergrowth and ensure a suitably dense product. The resulting material typically has high hardness (8,000-10,000 HV) with more uniform mechanical properties than natural diamond. Polycrystalline diamond blanks are normally produced in a disc format up to 75 mm in diameter with a 0.5-0.7 mm thick diamond layer bonded onto a WC substrate. The various insert shapes are produced by fabricating tools using segments/sectors of PCD cut from the initial disc or blank [53]. The properties of PCD tools depend upon the diamond grain size, the degree of diamond intergrowth together with the quantity and distribution of the catalyst material. Contrary to tungsten carbide tools, larger diamond grit products have higher hardness while finer grains are preferred when edge sharpness is of importance. At temperatures above ~ 1073 K, the diamond changes to graphite, and consequently cutting temperatures must not be allowed to exceed this level [51]. Since the cutting temperatures of CFRP composites are generally below this value, PCD tools can be successfully employed. Main disadvantage of the PCD tools is limited numbers of the tool shapes.

1.3.3.3 Tool coatings

It is well known that the application of tool coatings gives benefits in machining a wide range of materials in terms of wear resistance, productivity, etc. Presently applied tool coatings are divided depending of coating deposition technologies on physical (PVD) or chemical (CVD) vapor depositions. One or more layers are deposited and bonded to the substrate to provide a hard, wear-resistant surface capable of increasing performance and ensuring chemical stability. Coating performance depends on the coating material and its adhesion to the substrate. Therefore, coating thickness is a compromised decision based on experimental results. Indeed, thicker coating retards tool wear, however, thicker coatings are prone to brittle fracture and flacking.

The PVD method covers a broad family of vacuum coating processes in which the employed material is physically removed from a source by evaporation or sputtering. Then, it is transported by the energy of the vapor particles, and condensed as a film on the surfaces of appropriately placed parts under vacuum. Chemical compounds are deposited by either using similar source material, or by introducing reactive gases, such as nitrogen, oxygen, or simple hydrocarbons, that is reacted with metal from the PVD source [54].

The CVD process involves a gas-phase chemical reaction such as methane, nitrogen, etc. in an excess of hydrogen above a solid surface such as a carbide cutting tool, and is typically performed at temperatures of 1073 - 1373 K [55]. Several microns of a single layer or multilayer coating which can include hard metals (TiC, TiN, etc.) or polycrystalline diamond, are deposited on the tool surface in order to improve their wear resistance [8]. CVD diamond coating, with its high hardness level (10,000 HV), relatively low coefficient of friction, low chemical reactivity, except for ferrous workpieces, and high compressive strength makes it an ideal material for the machining of non-ferrous materials. The properties of the diamond or hardmetal layer are determined to a large extent by the gas mixing ratio and the process temperature of the tool surface. However, the main limitation of the CVD diamond coating process is the poor adhesion of diamond film due to the presence of cobalt in the carbide tool substrate [38].

Diamond-like carbon (DLC) is a mixture of hard carbon atoms, commonly referred to as sp^3 and sp^2 hybrid carbon-based bonded arrangements respectively, which are linked together in an amorphous structure [56, 57]. Unlike CVD diamond products, DLC coatings are produced using the PVD technique involving sputter deposition or an ion-beam system operating at lower temperatures (up to 773 K) [57], which does not cause any difficulties with the cobalt binder in carbide tools. The hardness of DLC depends on the sp^3 element concentration in the mixture. Where the element concentration approaches 100%, the coating hardness approximates that of natural diamond (8,000-10,000 HV), but drops by ~50% (3,000-5,000 HV) when the sp^3 diamond concentration is reduced to ~ 15-20% [56]. DLC layer thickness is typically of the order of several microns, whereas diamond coatings can be up to 25 μm.

Since CFRP composites became popular, various coatings differing in coating types or deposition modes are widely applied as wear-resistant protective coatings on cutting tools for their machining. For instance, Mkaddem et al. [58] compared the tool performances of CVD and PVD multilayer coatings. Three types of coatings, consisting of CVD-TiCN/Al_2O_3/TiN, PVD-TiAlN/AlCrO and PVD-TiN/TiAlN were deposited on turning inserts and compared in dry cutting CFRP. Results showed that fiber abrasiveness dominates wear mechanisms irrespective to coating type. Wang et al. [59] have investigated the tool wear of uncoated, CVD diamond-coated and AlTiN coated carbide drills when drilling the CFRP. It was observed that the diamond coating significantly reduced the tool wear, while the AlTiN coating performs no visible improvement over the uncoated drill. To date, the use of DLC-coated tools for the machining of CFRP composites is still limited. Murphy et al. [47] found limited benefits in using DLC coatings over uncoated tools in terms of tool wear when drilling CFRP. Moreover, they reported that TiN and DLC coatings had no beneficial effect on reducing delamination or

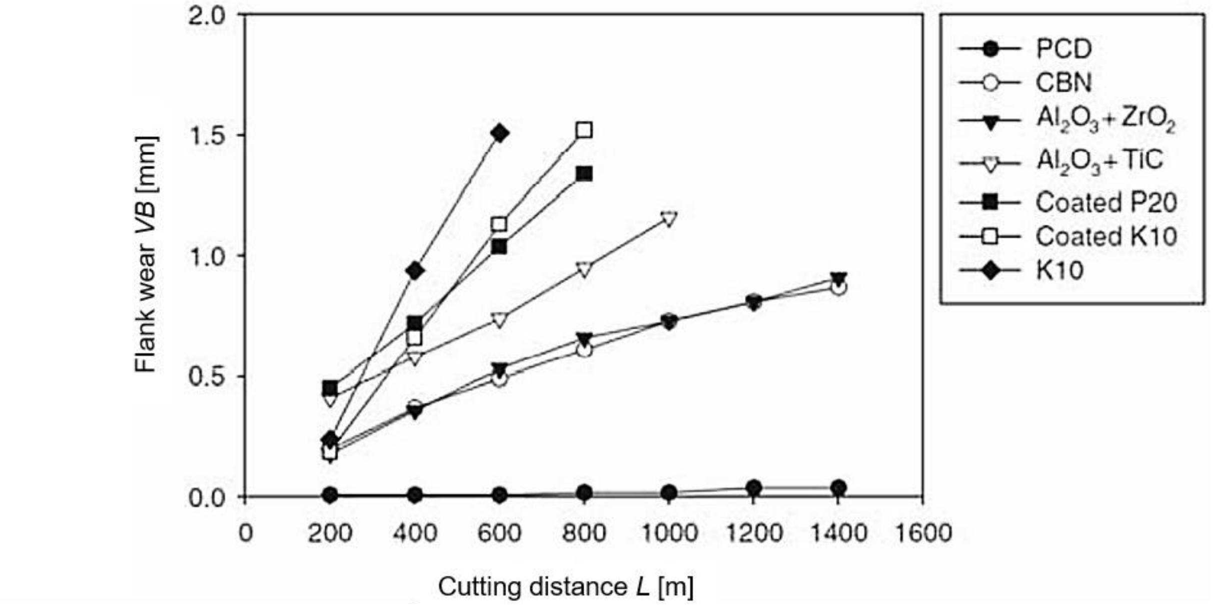

Figure 1.15. Flank wear results of different tool materials when turning CFRP [13]

thrust forces. Ferreira et al. [13] reported that tools with PCD insert significantly performed all compared competitors, include sintered cubic boron nitride (CBN), the ceramics, the coated and uncoated WC-Co based tools, when employed in turning CFRP, as shown in Figure 1.15. In conclusion, it is evident that the improvement effects provided by discussed coatings, except for the diamond, are all limited.

Nowadays, CVD diamond-coated tools have been evaluated by a number of researchers for cutting composite materials with encouraging results [31, 36, 38, 41, 60, 61]. Davim and Mata [60] measured lower cutting forces with CVD diamond coated tools compared to WC and PCD inserts when turning composites, although the surface roughness produced was approximately the same. Further benefits of CVD diamond coatings compared to equivalent solid ultra-hard tool materials are their lower cost (~ 30% cheaper than brazed PCD) and relative ease of implementation on complex tool geometries. It is known that the hot filament CVD (HFCVD) presents rather great practicality for the uniform deposition of the diamond films on the complex surfaces and the mass production of complex shape diamond coated cutting tools. Based on the advantages of HFCVD, Zhang et al. [62] have accomplished research on new types of doped diamond coated cutting tools, indicating that developed diamond films can significantly enhance the cutting performance of the drill for CFRP machining, in particular, the combination of the nano-scale grain size, lower surface roughness and better adhesion leads to the best performance of the Si-doped diamond coated drill. Further, Wang et al. [63] compared the cutting behaviors of different types of diamond coated drills in CFRP drilling,

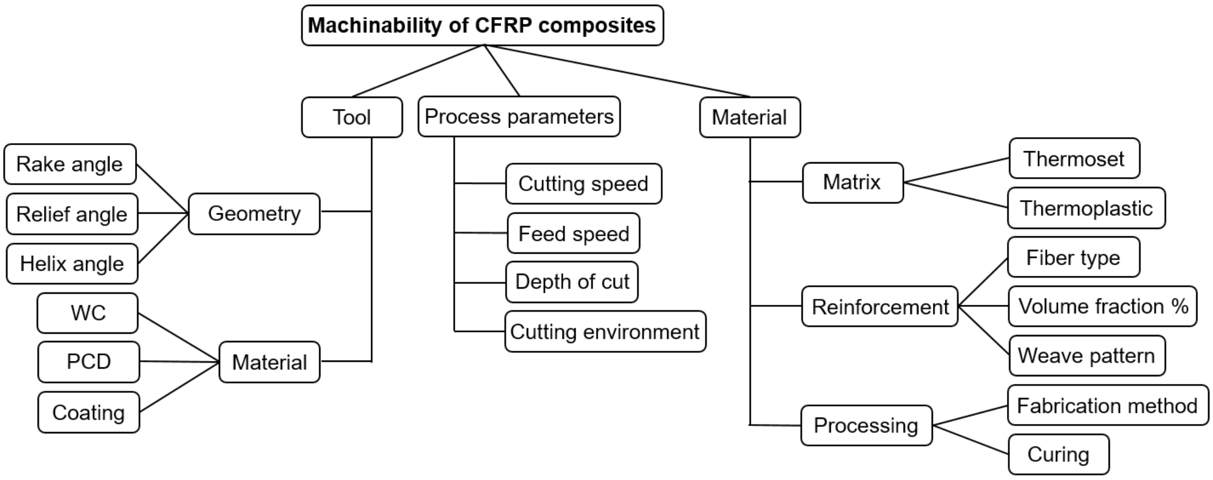
Machinability of CFRP composites
Tool
Process parameters
Material
Rake angle
Relief angle
Helix angle
Geometry
WC
PCD
Coating
Material
Cutting speed
Feed speed
Depth of cut
Cutting environment
Matrix
Thermoset
Thermoplastic
Reinforcement
Fiber type
Volume fraction %
Weave pattern
Processing
Fabrication method
Curing

Figure 1.16. Factors affecting machinability of CFRP composites

and indicated that boron-doped microcrystalline and nanocrystalline composite diamond coating performs better than any monolayer diamond coating.

In summary, influence of the tool coating on the cutting performance of the coated drills is obvious. Moreover, although varieties of high-performance diamond coatings, including some composite diamond films, have been extensively used on drills for CFRP machining, the tool failure should be further clarified, because the wear, fracture and film removal still exist.

1.4 Machinability of CFRP composites

Machining performance when cutting CFRPs is dependent on the composite specification including fiber and matrix properties, fiber orientation, type of weave, and curing conditions, in addition to the appropriate selection of cutting parameters and tool geometry, as summarized in Figure 1.16 [10, 11, 13, 14, 64].

1.4.1 Effect of material properties

Fiber orientation (denoted here by θ) has been found to be the main factor when cutting FRP. It significantly affects cutting forces, torque, machined surface quality, and chip formation [10, 11, 64]. Unlike metal workpiece, material removal in FRP workpiece is typically the result of a series of mini-fractures owing to the brittleness of the material elements. Wang et al. [64] were among the first to describe the various types of cutting mechanisms involved in chip formation observed when machining FRP composites and classified them into five categories, which were determined by the primary fiber orientation of the workpiece concerning the cutting

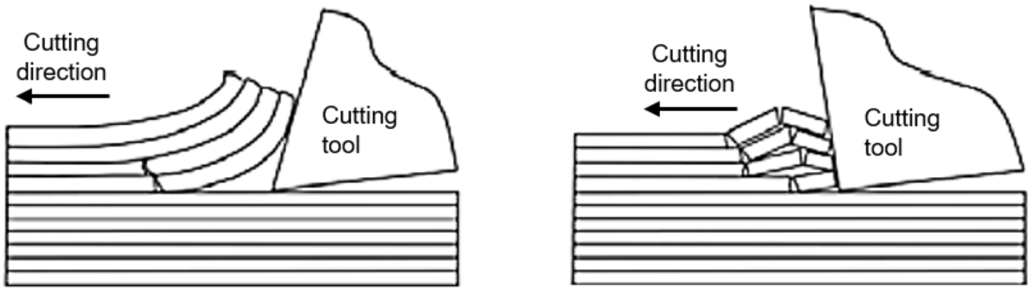
Cutting
direction
Cutting
tool
Cutting
direction
Cutting
tool

(a) Type I; θ=0° (180°)
Delamination

(b) Type II; θ=0°, negative rake angle
Fiber buckling

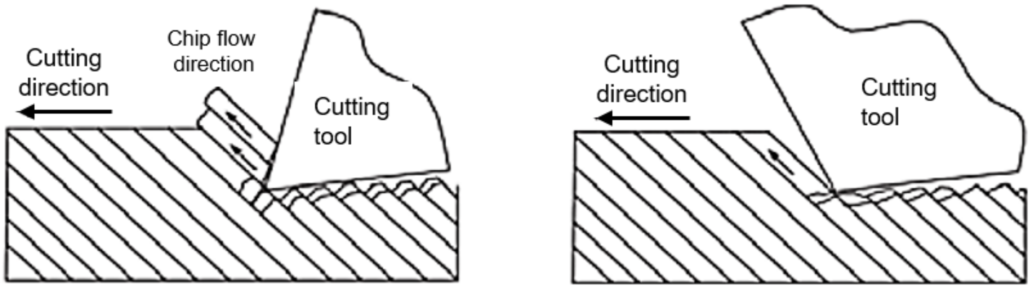
Cutting
direction
Chip flow
direction
Cutting
tool
Cutting
direction
Cutting
tool

(c) Type III; θ=45°
Fiber cutting

(d) Type III; θ=45°, negative rake angle
Fiber cutting

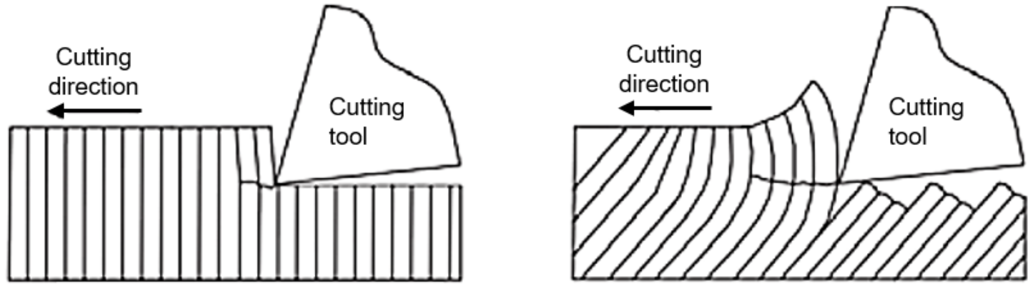
Cutting
direction
Cutting
tool
Cutting
direction
Cutting
tool

(e) Type IV; θ=90°
Deformation

(f) Type V; θ=135°
Shearing

Figure 1.17. Cutting mechanisms in the orthogonal machining of FRP composites [64]

direction and tool rake angle. These were designated as delamination (Type I), fiber buckling (Type II), fiber cutting (Type III), deformation (Type IV), and shearing (Type V).

Type I was seen to occur when cutting parallel to the fiber direction ($\theta = 0^{\circ}$) with positive rake geometry as shown in Figure 1.17(a). Following crack initiation at the tool tip, the damage propagates along the fiber/matrix interface. As the tool advances into the workpiece, the peeled layer slides up the rake face, causing it to bend like a cantilever. Bending-induced fracture then occurs ahead of the cutting edge perpendicular to the fiber direction. Small, discontinuous, and irregular chips are typically produced under these conditions. Additionally, the cutting forces generally fluctuate with the repeated cycles of peeling, fiber bending, and fracture.

Fiber buckling (Type II) becomes prevalent when zero or negative rake angle tools are employed to cut along the fiber direction, as shown in Figure 1.17(b). Here, fibers are subjected to compressive loading along their axis resulting in buckling loads. Progress of the cutting edge causes cracks at the fiber/matrix interface and eventually fractures the fibers perpendicular to their axis under intense bucking. This also results in small discontinuous chips. While the fluctuation in cutting forces is smaller than in Type I, the machined surface is comparable.

Fiber cutting Type III mechanism occurs when θ is between 0° and 90°, irrespective of tool rake angle. Here, the chip formation is a combination of fracture from compression-induced shear across the fiber axis together with fiber/matrix interfacial shearing along the fiber direction. During compression, cracks are generated in the fibers above and below the cutting plane, with the latter remaining within the machined surface, as presented in Figures 1.17(c) and (d). Under these conditions, the chip morphology may be continuous or discontinuous.

When cutting perpendicular to fiber orientation (θ = 90°), increasing interlaminar shear leading to fracture of the chip segments along the fiber/matrix interface becomes the dominant chip formation mode (Type IV), as shown in Figure 1.17(e).

Shearing (Type V) occurs at a fiber orientation of 105°–150° and is typically dominated by macro-fracture, see Figure 1.17(f). As cutting progresses, severe fiber deformation occurs resulting in excessive interlaminar shear along the fiber/matrix interface. Then chip formation is produced by the extensive elastic bending which results in cracks in both fibers and matrix producing relatively long chips. Here, the machined surface is irregular and the fiber ends have different lengths because fracture occurs at different points along their length. Elastic recovery also takes place following fiber shearing and leaves an irregular cut surface, as shown in Figure 1.18.

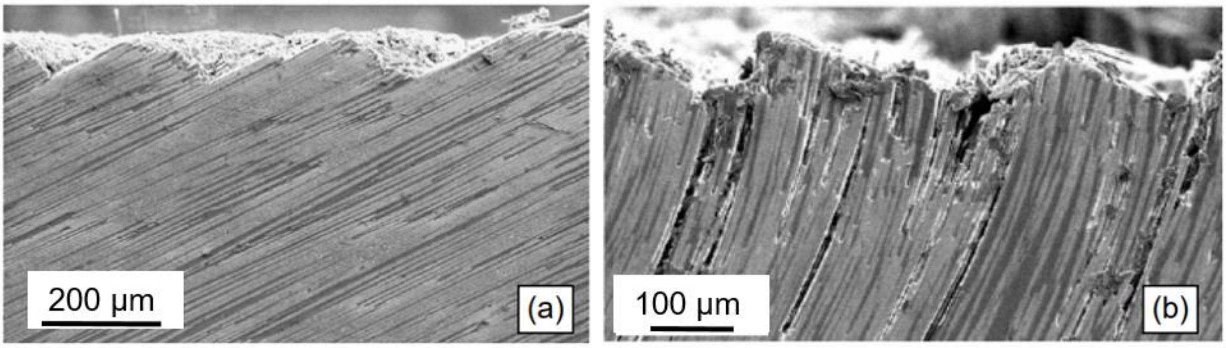

Figure 1.18. Microstructure when orthogonal cutting of graphite/epoxy composite: (a) θ =150° and 0.05 mm depth of cut and (b) θ = 120° and 0.1 mm depth of cut [8]

Proposed above the cutting mechanisms related to the UD laminates. Multidirectional (MD) CFRP composites are commonly used in many applications contrary to the UD ones.

When drilling MD CFRP composites, variations in cutting forces are common as the tool edge moves through different fiber angles throughout the composite workpiece causes to discontinuous machining and detrimentally influence the cutting tools through their edges micro-chipping. On the other hand, laminate design depends on the required CFRP product properties. Thus, the combination of the tool shape, material and coating should minimize the wear effects of this mechanism.

1.4.2 Effect of process parameters

The drilling thrust force and torque are affected by the cutting speed and feed rate. Both thrust force and torque increase significantly with increasing feed rate due to its direct influence on uncut chip size [10]. A high correlation has been reported between feed rate, thrust force, and delamination when drilling high-strength CFRP [31]. Whereas the effect of cutting speed on thrust force and torque is not significant. Also, the feed rate had a detrimental effect on surface roughness as an increase from 2.0 to 5.0 μm Ra was measured when the feed rate was raised from 0.05 to 0.25 mm/rev [13].

The majority of published research has highlighted the strong correlation between thrust force and delamination, particularly at hole exit. Chen [35] reported that cutting speed had a negligible effect on thrust force and torque when drilling UD and MD CFRPs, while feed rate influenced both aspects. Similar results were also obtained by Tsao [65]. Estimated thrust force results were in close agreement with experimentally measured data. In work by Fernandes and Cook [46], thrust force and torque were shown to grow with cut distance increased. Obviously, that thrust force increased in relation to the drilled hole number, which was attributed to the chipping and wear of the cutting tool. In another research, Durão et al. [66] studied the influence of different tool geometries, such as twist drills with various point angles, brad & spur drill, dagger drill, and step drill, on thrust force, surface roughness, and delamination. They reported that a low feed rate can decrease thrust force and delamination. Also, they noted that thermal degradation may be considerable at low feed rates.

The effect of process parameters on the characteristics of uncut fibers was investigated by researchers to develop methods for machining composites without leaving uncut fibers. For instance, Xu et al. [31] observed that the burr area increases with the increase in thrust force. Furthermore, Xu et al. [38] conducted detailed drilling experiments on CFRPs using different tools, such as dagger, brad & spur, and twist drills, and concluded that feed rate has the most significant influence on the extent of defects. Also, it was observed that the brad & spur drill produced the best performance on damage reduction.

According to cutting force optimization, the minimum peel-up and push-out delamination occurred at a minimum feed. On the other hand, drilling CFRP composites with very low feed seems ineffective due to increased machining time and cost. Also, thermal damage to the CFRP material is expected under increased tool/workpiece contact time. Therefore, the selection of process parameters should match both the delamination control and process efficiency. Usually, a high cutting speed (150-200 m/min), as well as a low feed rate (0.01-0.05 mm/rev), is recommended for CFRP drilling in the industry practice to prevent the drilling-induced delamination and guarantee drilling efficiency at the same time [8].

1.4.3 Effect of tool materials and geometries

Tool materials and geometries play an important role in relation to tool life and machined surface quality when cutting CFRP composites. Feito et al. [32] studied three different cutting drill geometries, as brad center, step and reamer, in terms of drilling forces and delamination for woven CFRP. The authors found that the reamer drill showed the best results. Shyha et al. [33] analyzed the drilling of small holes in quasi-isotropic CFRP laminate with two different tool geometries, conventional twisted and stepped. Increases in the feed rate lead to thrust force enhancement. Delamination at the hole entrance was higher for the stepped drill than for the twisted drill. However, the increment of point angle, from 118° to 140°, leads to a decrease in delamination. In another research, Heisel and Pfeifroth [44] conducted drilling experiments in CFRPs, and analyzed the influence of different point angles (155°, 175°, 185°, 178°) on thrust force and delamination. They discovered that an increase in point angle increases delamination at the exit of the holes. It was also observed that delamination decreases at the entry of the holes simultaneously with an increase of the point angle of twist drills.

Wang et al. [61] reported that a diamond coating of the cutting tool can reduce thrust force and delamination. Also, the diamond coating increases wear resistance and tool life. At the same time, they found that the number of uncut fibers increases due to increased edge roundness caused by coating growth. The study of Iliescu et al. [67] shows that the tool life of diamond-coated carbide drills can be 10-12 times higher compared the tool life of uncoated carbide drills. Furthermore, related cutting speed can be 3 times higher when using diamond-coated tools than uncoated ones. Also, the researchers suggested a tool specification for drilling delamination-free in CFRPs, recommends point angle of 125°-130°, helix angle of 35°-40°, clearance angle of 10°-25°, and diamond coating as well. Qiu et al. [68] studied a drilling characteristics of the dagger, the double point angle, and the candle stick drills when drilling CFRPs. The results show that the side edge has poor ability to remove burrs, and the tip structure of the outer corner of the candle stick drill can greatly reduce the entry damage. However, the outer corner small tip structure of the candle stick drill cannot remove the uncut fiber around θ=0° of hole exit. The cutting edges of the dagger drill makes a small thrust force at the drilling exit stage. Then, a novel drill is developed for drilling CFRP based on the advantages of the three kinds of drills. The cutting test result shows that the new compound drill can effectively remove fibers and reduce thrust force at the drilling exit stage, form burr-free and small delamination hole.

1.5 Tool wear phenomena

The most commonly used criterion to determine the end of tool life is maximum flank wear (VB_{Bmax}) which is typically between 0.3-0.6 mm for metals, however, there is no established tool wear criterion concerning cutting FRP composites [8]. When drilling CFRP, both flank and chisel edge wear is evident, which increases with the number of drilled holes. The principal tool wear mechanism experienced when cutting CFRP composites is abrasion with micro-chipping often present as a secondary wear mode. Abrasion occurs when hard workpiece particles progressively indent and erode tool surfaces and remove tiny amounts of material from the cutting tool. In the case of CFRP, this is attributed to the highly abrasive fibers within the material. The presence of micro-chipping is generally a result of force oscillations due to the composites' inhomogeneous nature. Unlike metal machining, diffusion wear is rarely seen when cutting CFRP due to the relatively low temperatures and pressures involved. Gross fracture and

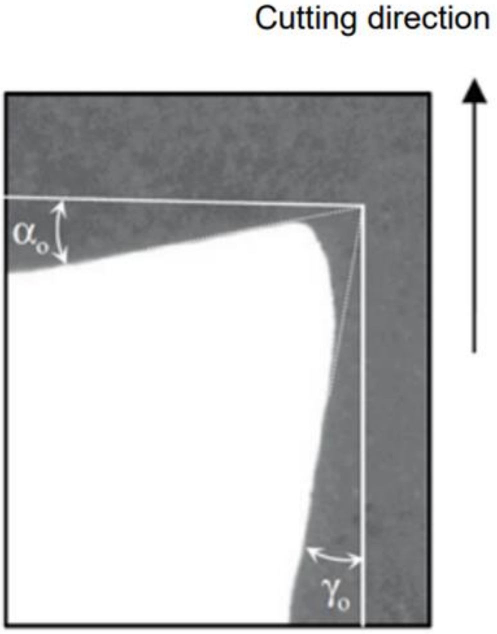

Figure 1.19. A cross section of a replica from a cutting edge when machining FRPs (α_o is the rake angle and γ_o is the clearance angle) [8]

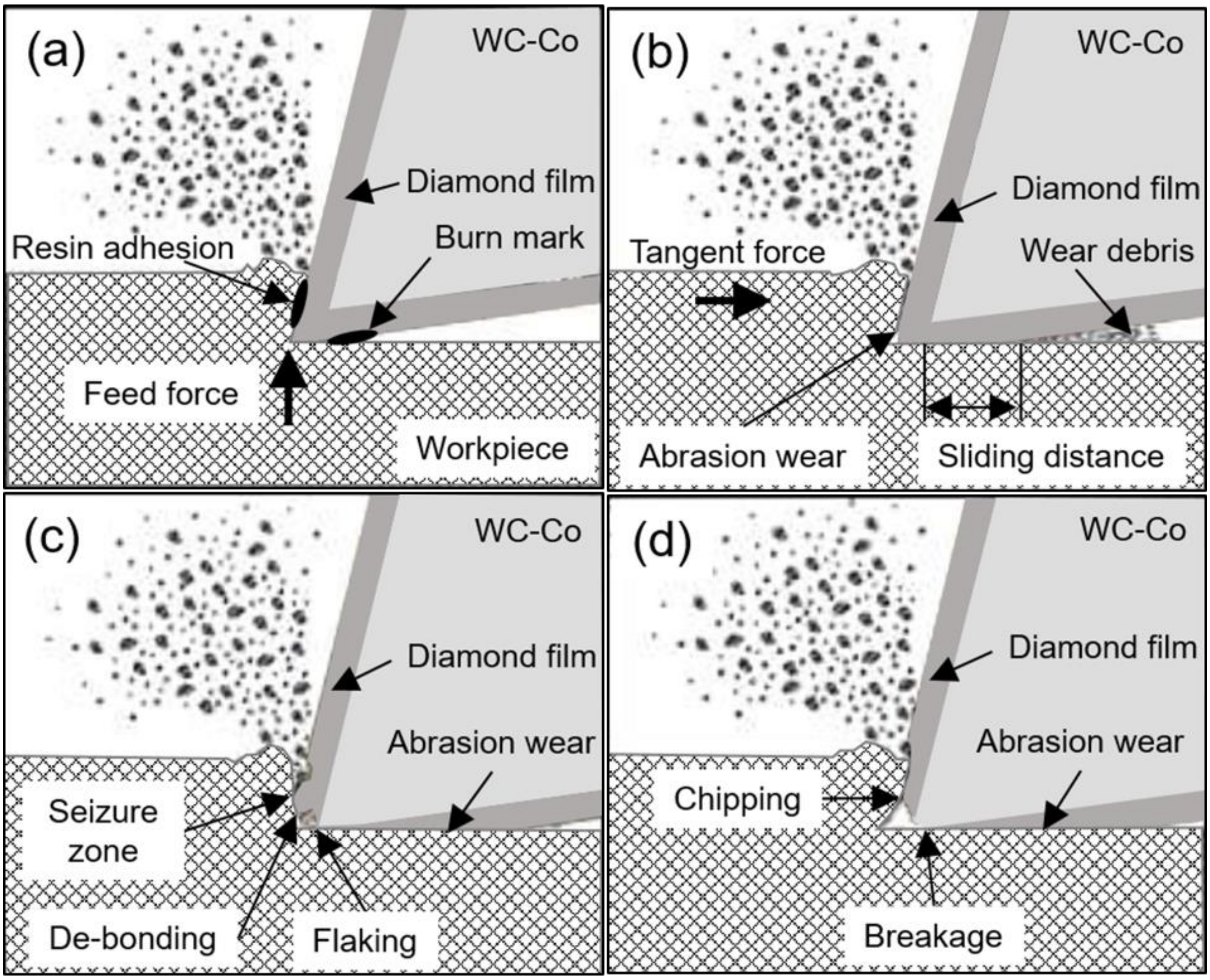
(a)
WC-Co
Diamond film
Resin adhesion
Burn mark
Feed force
Workpiece
(b)
WC-Co
Diamond film
Tangent force
Wear debris
Abrasion wear
Sliding distance
(c)
WC-Co
Diamond film
Abrasion wear
Seizure zone
De-bonding
Flaking
(d)
WC-Co
Diamond film
Abrasion wear
Chipping
Breakage

Figure 1.20. Schematic illustration showing tool wear patterns in (a) adhesion and abrasion wear, (b) extended abrasion wear on the flank face, (c) flaking and delamination and (d) breakage of substrate material [70]

edge chipping can also occur under interrupted cutting conditions due to the variation of mechanical properties between the reinforcement and matrix phase. The typical wear pattern observed however when cutting CFRP is severe edge rounding of the tool [8] as shown in Figure 1.19. The considered above tool wear phenomenon is typical for non-coated WC-Co-based tools. In the case of the application of CVD diamond-coated tools, the tool wear mechanism has an inherent phenomenon. During cutting, the fracture modes associated with diamond-coated tools may involve cyclic flaking and delamination at the cutting edges. This phenomenon usually begins with build-up along the cutting edges, which unbalances forces along the cutting edges, and is followed by fracturing along the chisel edge and peripheral corners. Differences in the thermal expansion coefficient along the interface between the coating and substrate produce unbalanced internal stress, resulting in shear force. Shear stress exceeding the threshold of fracture toughness in the coating layer can trigger flaking and delamination. Low frequency load can also be the source of fatigue failure [69]. Cyclic loading at the cutting edge can lead to the initiation of cracks in the rim area, which tend to propagate rapidly as micro-cracks coalesce into striations, leading to catastrophic failure.

According to the cutting mechanism, Kuo et al. [70] proposed the wear process of the CVD diamond tool during the drilling of CFRP, as shown in Figure 1.20. According to the tool wear evolution, the wear behavior could be classified into four stages. Figure 1.20(a) shows the continued adhesion of polymeric residue on the rake and flank faces of the cutting tool due to a temperature-induced by high cutting speed. The varied geometry at the cutting edge reduces the clearance angle thereby diverting the cutting actions into ploughing and rubbing actions. In Figure 1.20(b), abrasion wear on the flank face increases steadily due to the compression stress on the sliding zone being high and also due to the increase in friction heat and temperature. Scoring wear on the successive flank face may occur due to the removed abrasive mixtures pushing by the fibers bouncing back on the machined surface. The wear process may involve graphitization in the diamond under a high cutting temperature, attrition in the columnar diamond grains, and abrasion wear which is produced by the mixture of the diamond debris and carbon fiber fragment. As shown in Figure 1.20(c), due to the increased intermittent loads on the seizure zone, diamond film failure in terms of flaking and delamination occurs along the cutting edge, which exposes the sharp edge of the tungsten carbide substrate which is simultaneously re-sharpened under the grinding effects of the carbon fiber abrasives. As seen in Figure 1.20(d), when the CVD diamond-coated layer had entirely flaked off, the exposed tungsten carbide edge was rapidly worn away; thereby greatly increasing the cutting force. This was due to the rounding of the cutting edge as well as a loss of clearance and rake angle during cutting.

Finally, it can be summarized, that tool wear in machining CFRP occurs primarily by abrasion and micro-chipping. Abrasive wear is caused by sliding of the tool surfaces under pressure against the abrasive fiber material embedded in the polymer matrix. Abrasive wear is manifested by clear rounding of the cutting edge and in the form of wear lands on the rake and the clearance surfaces of the cutting tool. Micro-chipping is caused by the oscillating cutting forces that result from repeated fracture of the fiber reinforcement. This type of wear is characterized by small and large voids on the cutting edge which are caused by pieces of the tool material being dislodged from the cutting edge. Therefore, the cutting tool material requirements to resist these types of wear are high hardness and high toughness. Unfortunately, cutting tool materials that have high hardness generally suffer from low toughness. Cemented carbides on the other hand offer higher toughness but lower hardness than PCDs. Nevertheless, they remain the most versatile and economically feasible choice of cutting tool material. The ability to hot press these tools from powders of the WC phase and Co binder phase allows them to be produced in different shapes and properties suitable for machining application. The wear of cemented carbides occurs mostly by abrasion. Significant improvement in the wear resistance is achieved by application of the diamond coating, that adds the high hardness required for machining CFRP.

1.6 Research objective

As described in previous sections of the study, CFRP composites became popular for use in a wide range of industries due to their high specific strength and stiffness coupled with damping properties and almost zero thermal expansion coefficient.

Conventional drilling finds great application in manufacturing CFRP products, especially in the aerospace industry as final operation during aero-structure assembly. The quality of drilled holes usually significantly affects the assembly quality and service life of the aircraft.

However, CFRP is one of the difficult-to-cut materials as before. The abrasive effect of hard carbon fibers in CFRP always leads to severe tool wear and, consequently, short tool life. Furthermore, when cutting tool conditions deteriorate due to wear and tear, the CFRP workpiece tends to show material-specific defects, such as delamination, burrs, and tearing of fibers. Besides the tool wear influence, unsuitable tool shape and/or process parameters lead to material defects appearance even new tools are applied.

Nowadays, a well-known method of tool life extension consists in the CVD deposition of polycrystalline diamond films on WC-Co-based cutting tools. Moreover, research data overviews show that the utilization of special shape-designed WC-Co tools with CVD diamond coatings benefits CFRP machining, resulting in less burr formation and delamination effects. Indeed, the diamond-based materials show the highest hardness compared to the present tool materials that provide effective wear resistance against abrasive wear. Research confirmed that special-designed tool shapes are effective to reduce cutting forces, cutting-induced CFRP damage, and decreasing tool wear. Recently, one-shot drills have been significantly interested in researchers in order to develop novel tools with advanced geometries.

Furthermore, the research data overview shows that the interface adhesion between the diamond coatings and WC-Co tool substrates has a fatal effect on cutting performance due to the peeling of the coating during machining. Considering that tungsten carbides contain Co as a binder and detrimental Co interaction with carbon during the diamond deposition process is well studied, many adhesions enhanced approaches were developed. One of the new promising ways of improving interface adhesion is doping into diamond coatings by chemical elements. Preliminary research confirmed that the interface adhesion can be improved by doping CVD diamonds with minute amounts of boron or silicon. Therefore, in this study, the effects of boron doping on the diamond films were investigated with the aims of improving film adhesion to WC-Co substrate and cutting performance one-shot drills with the doped diamond films.

On the other hand, such diamond-coated WC-Co tools with complicated shapes have a higher cost than conventional tools. Therefore, a reconditioning of mentioned above tools is economically attractive. Currently, the tool makers' industry does not have commercially available reconditioning techniques for CVD diamond-coated WC-Co-based tools at all. This is attributed that presently used film removal methods are not effective for the stripping of diamonds due to their high chemical stability.

A practically important method of CVD diamond decoating has been developed before this study. The method consists in the reactive ion beam etching (RIBE) of a CVD diamond film with multiple closed electron drift ion sources(CDIS). The feasibility of the RIBE to remove CVD diamond films from cutting tools with a complex geometry is confirmed. On the other hand, the cutting performance of RIBE-reconditioned tools has not been studied. Therefore, in this study, the effects of RIBE decoating and CVD diamond film deposition on various important tool properties and their cutting performance were investigated from the standpoint of the reconditioning approach.

In other words, the first aim of this research is to carry out a comprehensive study on the application effect of boron-doped diamond coatings in the drilling of difficult-to-cut material, specifically CFRP. Further, the second aim of this research is to improve machining profitability by developing of novel reconditioning technique for the diamond coated tools. The research consists of experimental works on the deposition and/or decoating of such advanced diamond coatings on the WC-Co-based drills with following cutting performance tests.

The specific objectives for the research can be summarized as follows:

- Experimental investigation on the effect of boron-doped CVD diamond coatings with different surface morphologies on cutting performance of WC-Co one-shot drills when drilling CFRP laminates.
- Development of the reconditioning approach for CVD diamond coated WC-Co one-shot drills.
- Experimental investigation of the combined effects of the tool decoating and CVD diamond deposition on the WC-Co surface morphologies, cutting edge geometry, and diamond film adhesion through reconditioning cycles.
- Experimental investigation on the cutting performance of reconditioned drills with the aims of drilled hole quality and tool life.

1.7 Overview and outline of the thesis

This doctoral thesis consists of four chapters, and the content of each chapter is briefly described as follows:

Chapter 1 gives an introduction of the entire study carried out and it also outlines the research background and motivation. It gives brief description of composite materials with emphasizing to CFRP, and clear explanation of the machining CFRP composites by drilling with description their machinability, drilling-induced damages, applied tools and a discussion to tool wear phenomena. Influences of drilling parameters, tools' shape, materials and coatings, on drilled hole quality are considered. This chapter also outlines the objective and scope of the research work.

Chapter 2 presents a comprehensive experimental study on the cutting performance of CFRP with boron-doped CVD diamond-coated drills. Firstly, HFCVD process was described in term of a fundamentals, applied equipment, a deposition parameters and a substrate pretreatment method. Then, experimental work was carried out on cutting performance evaluation of boron-doped and undoped diamond coatings in the drilling of CFRP laminates. The influence of the diamond coating properties, such as film morphology, boron doping, and etc., on the film adhesion itself and the drilled hole quality was clarified by evaluating the tool wear, thrust force, torque, CFRP delamination, and etc.

Chapter 3 discusses a detailed study on reconditioning of diamond-coated tools with the aims of creating reconditioning approach, available in industries applications, and evaluate cutting performance of reconditioned tools when CFRP drilling. Experimental works were carried out deposition boron-doped CVD diamond coatings and following tool decoating by RIBE. Further, cutting tests were carried out and repeated to evaluate cutting performance of reconditioned drills and compare with the new drills. In order to estimate an influence of reconditioning procedures on drills' cutting ability, substrate textures were investigated in terms of surface morphology, adhesion, and cutting edge geometries. The entire results of the chapter study were analyzed to present the reconditioning method for increasing CVD diamond -coated tools' efficiency. This aim could be achieved by using an appropriate WC-Co substrate pretreatment approach, and control of surface texture.

Chapter 4 summarizes the main conclusions derived from the entire study. The key results are outlined and ideas for further study are stated.

Chapter 2. Advanced diamond coatings and their cutting performance in drilling of CFRP laminates

2.1 Introduction

It is well known that only application of diamond-based materials gives benefits in CFRP machining. Furthermore, combinations of specially designed WC-Co based cutting tools with polycrystalline diamond coatings are one of the best ways to increase the tool life and to reduce the CFRP product defects. There are two kinds of material in the market for diamond cutting tools, high pressure - high temperature (HPHT) polycrystalline diamond (PCD), and low pressure chemical vapor deposited micro and nanocrystalline diamond.

As briefly described in previous chapter, in PCD tools, diamond grits produced by HPHT synthesis are compacted and sintered with cobalt as a binder to form a PCD tip with 150 – 1,000 μm of thickness, which is subsequently attached to the substrate material, commonly cemented carbides like WC-Co. In contrast, the low pressure approach produces a diamond thin-film coating with 5 - 35 μm of thickness that is directly deposited onto the surface of the carbide by the CVD technique. Moreover, compared with PCD insert, a diamond film produced by the CVD is lower-cost and is suitable for diamond deposition on complex-shaped cutting tools.

Since artificial diamond synthesis by the HPHT method was first introduced in 1955 by General Electric, a researchers have tried to deposit diamond from the gas phase [55]. In 1956, the former U.S.S.R. scientists B. Spitsyn and B. Deryagin proposed the growth of diamond at low pressures through the thermal decomposition of carbon tetraiodide (CI_4) and carbon tetrabromide (CBr_4). Subsequently, B. Spitsyn et al. [71] explored direct CVD from hydrocarbons and in 1969 it was stated that diamond was synthesized from pure methane at pressures from 13 to 40 Pa and temperatures from 1223 to 1323 K.

A major breakthrough on the CVD diamond process was achieved in the early 1970s. It was the use of atomic hydrogen during growth to remove graphite formation, based on the phenomenon that atomic hydrogen etches graphite much faster than diamond. This gave a much higher growth rate and it permitted the nucleation of new diamond crystals on non-diamond substrates.

The modern era of CVD diamond started in the early 1980s, since Matsumoto et al. [72, 73] first published a series of papers in which different techniques, hot-filament CVD process, RF-plasma CVD, and microwave plasma CVD were described. They reported that diamond particles and films could be deposited on various substrates heated around 1123 K, using a mixed gas of methane diluted by hydrogen, and preferred partial pressures in the range 4×10^3 to 5×10^3 Pa. A growth rate higher than several microns per hour was achieved. These studies contributed that deposition of diamond by CVD has been largely studied by different research groups worldwide. As result, the CVD diamond coated carbide tools were initially introduced to the market at the 1994 International Manufacturing Technology Show in Chicago by four tool-making companies, as Crystallume, Sandvik Coromant, Kennametal, and Teledyne, fulfilling expectations about the practical use of the tools.

However, besides all the benefits brought by CVD diamond coated tools, new challenges emerged in terms of how to improve the adhesion of the diamond coating and extend the cutting tool life, and still remain today.

2.2 Diamond synthesis by CVD

2.2.1 CVD systems

The growth of diamond films from vapour phase on non-diamond substrates at practical rates was accomplished with the development of thermal- and plasma-enhanced CVD methods, in which a hydrocarbon gas mixed in low concentrations with hydrogen is energized thermally or in a plasma, prior to contact with a heated substrate. Between these methods, hot filament-assisted thermal CVD (HFCVD), microwave-plasma CVD, combustion flame-assisted CVD, and direct-current (DC) arc plasma jet CVD are predominant for commercial using [74, 75]. The various CVD techniques, although different in their process details, have a several common features, the most important are the following:

- Growth in the presence of atomic hydrogen. The deposition of polycrystalline diamond film in the presence of atomic hydrogen was based on phenomena that diamond is more stable towards atomic hydrogen influence than graphite.
- Dissociation of carbon-containing source gases. In the various CVD methods, the carbon-containing compounds are dissociated by thermal, plasma or combustion processes to produce the reactant species responsible for the diamond nucleation and growth. The film growth rate depends on the ability of these reactant species to be transported to the substrate.
- Growth at moderate substrate temperatures. In all CVD methods, diamond growth takes place at substrate temperatures between 773 K and 1473 K. Growth at temperatures above or below this range often leads to graphite deposit.

2.2.1.1 HFCVD

In this method, as shown in Figure 2.1, diamond particles are deposited on a heated substrate from a mixture of methane and hydrogen dissociated by hot refractory metal filament placed close to the substrate. The filament temperature may reach around 2473 K during this process. The main role of the hot-filament is to dissociate molecular hydrogen into atomic hydrogen. The dissociation mainly occurs near the filament due to the high gas temperature.

Besides atomic hydrogen creating, it was discovered that during diamond deposition the tungsten filament reacts with methane and undergoes carburization. This results in consumption of carbon from the methane, and thus a specific incubation time is needed for the nucleation of diamond films. Therefore, this process may affect the early stages of thin film growth. In addition, the resistance of the filament should be monitored and adjustments to the supplied voltage and current made in order to maintain the temperature of the filament constant.

Due to the temperature upper limit of the filament material, hot-filament processes operate at significantly lower gas temperatures than plasma processes, and consequently produce less atomic hydrogen. The low gas phase concentrations give relatively low growth rates compared to the plasma methods.

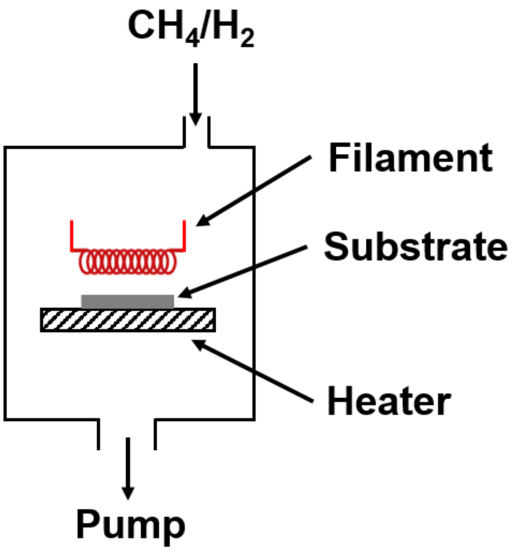

Figure 2.1. Schematic diagram of HFCVD method

Despite these drawbacks, hot-filament assisted deposition has remained popular because of its low capital cost and simplicity. Also, hot-filament reactors are directly scalable to large sizes and can be used to coat complex shapes and internal surfaces.

2.2.1.2 Plasma-enhanced CVD methods

These methods of diamond growth involve various forms of plasma-assisted CVD using carbon-containing species mixed in low concentration with hydrogen. Plasma is generated either by various forms of electrical discharges or by induction heating. The role of the plasma is to generate atomic hydrogen and to produce proper carbon precursors for the growth of diamond. Atomic hydrogen is produced by electron impact dissociation of molecular hydrogen. Such atomic hydrogen produced in plasmas generally has high kinetic energy due to the difference between the hydrogen dissociation energy and the electron kinetic energy. This accounts reported for the significantly higher growth rates in plasmas, compared with HFCVD.

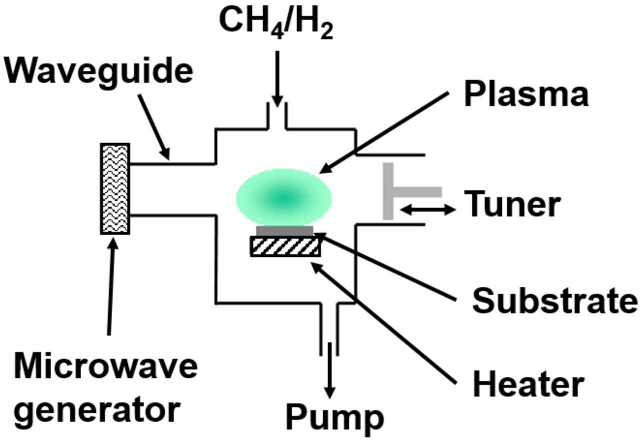

Figure 2.2. Schematic diagram of microwave CVD method

Among the plasma-enhanced methods, microwave-plasma-assisted CVD, as shown in Figure 2.2, has been used much more extensively than others for the growth of diamond films. This method of diamond growth has a number of distinct advantages over the other methods. Microwave deposition, being an electrode less process, avoids contamination of the films due to electrode erosion Furthermore, the microwave discharge at 2.45 GHz produces higher plasma density with energy electrons, compared with the RF discharges at 13.5 MHz, due to higher process frequency. This should result in higher concentrations of atomic hydrogen and hydrocarbon radicals. An additional advantage is that the plasma is confined in the center of the deposition chamber in the form of a ball and this prevents carbon deposition on the walls of the chamber.

Other important plasma-based method is DC arc jet CVD, as shown in Figure 2.3. The DC arc jet is a general name for a high pressure direct-current plasma discharge. Electrical energy is converted to thermal and kinetic energy of a flowing gas mixture by an electric arc discharge.

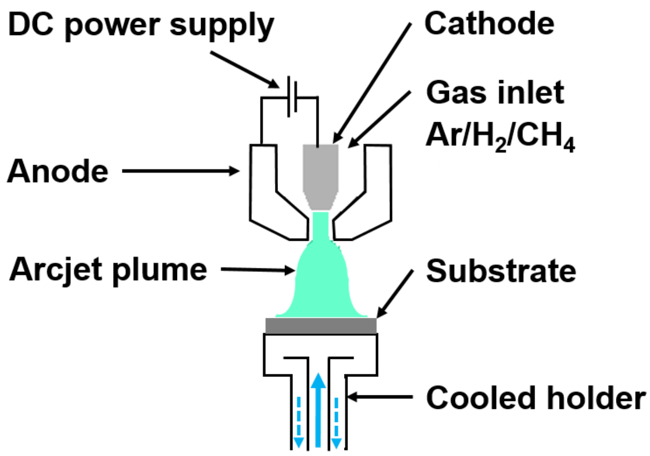

Figure 2.3. Schematic diagram of DC arc jet CVD method

Like other CVD methods, a major constituent of the gas mixture is hydrogen, while methane is introduced into the plasma jet to provide a source of carbon. The plasma temperature is 1000-5000 K as average. The plasma jet containing these reactive species affects onto a cooled substrate surface for film growth. The electric discharge is sustained between a concentric cathode rod and a surrounding cylindrical anode, creating ionized arc column. Extremely high diamond growth rates (~1 mm/hour) can be achieved using this method [55]. In addition, arc jets have a distinct advantage over other diamond CVD methods in that the deposition of diamond can proceed simultaneously with the deposition of other ceramics and metals by introducing powders of various types into the plasma stream. Such a functional gradient material can reduce the thermal stress between the diamond film and the substrate with, consequently, increasing the adhesion strength between them.

2.2.1.3 Combustion-flame assisted CVD

This method allows the growth of diamond at atmospheric pressures using combustion flames from an oxygen-acetylene brazing torch. Because of its simplicity and low cost of the experimental apparatus as well as the high growth rate, this method looks promised in diamond growth.

A schematic diagram of the method is shown in Figure 2.4. It consists of a brazing torch supplied with oxygen and acetylene (C_2H_2), and a water-cooled substrate. The substrate temperature is adjusted by varying distance of the substrate surface position related the torch. Normally the oxygen-acetylene torch is used with an excess of oxygen. The acetylene is

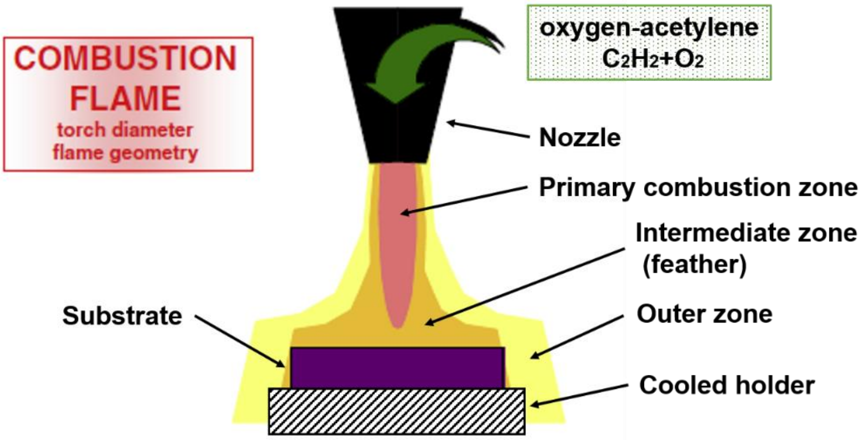
COMBUSTION FLAME
torch diameter
flame geometry
oxygen-acetylene
$C_2H_2+O_2$
Nozzle
Primary combustion zone
Intermediate zone (feather)
Substrate
Outer zone
Cooled holder

Figure 2.4. Schematic diagram of combustion-flame assisted CVD method [75]

completely burned to CO_2 and H_2O. Hydrogen addition to the oxygen-acetylene flame was found to reduce the amount of amorphous carbon in the diamond films [55].

Combustion flames operating in the fuel-rich mode have three distinct regions, as shown in Figure 2.4. The inner cone is the primary combustion zone followed by a diffused intermediate region and an outer zone. The temperature in the primary combustion zone can reach up to 3300 K. The combustion reaction at this region leads to the formation of CO and H_2 with a number of reactive intermediate species (H, OH, C_2, C_2H, etc.). In the fuel-rich mode, the un-burnt hydrocarbons as well as the combustion products form the diffuse intermediate and reaction free region, which is called feather. The outer zone, which is also known as a secondary combustion zone, consists of a flame caused by turbulent diffusion of oxygen from the surrounding atmosphere. In this region, the products of the combustion reaction are oxidized to CO_2 and H_2O. The substrate is usually placed in the feather region of the flame, where there is an abundance of atomic hydrogen and hydrocarbon radicals as required for diamond film grows.

2.2.1.4 Summary

All mentioned above CVD methods were evaluated in terms of diamond coating deposition on cutting tools for CFRP machining. Such criteria as coating growth rate and its uniformity, scaling feasibility for commercial application were compared. Some conclusions are considered below.

The deposition area of a microwave reactor is limited by the frequency of the plasma generator. The maximum deposition area in modern microwave systems is limited to about 150 mm in diameter [76]. Some DC torches are capable to deposit areas up to 200 mm in diameter. Therefore, scalability of the plasma approaches is quite difficult engineering task for large deposition area compared with HFCVD. Indeed, the hot filament reactors are simple in their design. DC power supplies are used, control mainly comprises gas ratios and flow rates, vacuum level, and the amount of DC power in the filaments.

In growth rate point of view, HFCVD reactors typically grow diamond at 0.3 to 2.0 µm per hour, microwave systems from 1.0 to 5.0 µm per hour, and the DC arc jets have demonstrated growth rates exceeding 20 µm per hour [76]. On the other hand, a film uniformity is an area where hot filament reactors have demonstrated their superiority over both microwave and DC arc jet approaches. HFCVD reactor has the advantage of uniform temperature across the entire deposition area. In contrast, microwave reactors and DC arc jets create a sphere or plume of energy that is hotter at the center compared its periphery. Such plasma temperature effects can be compensating by rotating the substrate in an attempt to normalize deposition temperatures. This rotation adds complexity and cost, reduces reliability and often is a source of contamination. Another phenomenon observed is that substrates in microwave reactors and torch reactors tend to get hot spots on sharp corners of the tool substrates. The hot corners accelerate film growth on the ones, with the result film thickness non uniformity. Hot filament reactors have demonstrated uniform temperature across large deposition areas and uniform coatings across an individual substrate. Since a temperature control is critical to diamond deposition, it is much easier to adjust the voltage on a hot wire than to try adjust the plasma sphere proximity to a substrate in ordinary microwave system. Comparison overview of the CVD methods is summarized in the Table 2.1.

Therefore, it can be concluded that HFCVD approach is most suitable for coating complex shaped tools, as a drills for CFRP machining. Based on the mentioned above conclusions, the HFCVD method was chosen for deposition advanced diamond films in the framework of this study.

Table 2.1 CVD methods comparison:

Method	Growth rate [μm/hour]	Deposition area [mm^2]	Advantages	Drawbacks
Hot filament	0.3-2	Up to 100,000	Large area at low pressure Scalability Simple setup	Low growth rate Degradation of the filaments Chamber is required
Microwave plasma assisted	0.1-5	Up to 80,000	Excellent quality of diamond layers Stable deposition parameter Large deposition area	Simulation of chamber is required Low scalability Chamber is required
DC arc jet	<20	Up to 10,000	Highest growth rate	High power and gas consumption Contamination Chamber is required
Combustion flame assisted	10-200	Up to 5,000	High growth rate No chamber is required Simple setup	High heating of the substrates Small deposition area Unstable process

2.2.2 CVD diamond coatings for cutting tool applications

As discussed in previous sections, the HFCVD process is the most suitable process technology for tool coating with CVD diamond thin films. In this technique, the required atomic hydrogen is produced with electrically heated glowing filaments made from refractory metals (Ta, W, or Re). An appropriate spatial filament arrangement provides distribution of the required species, even when processing substrates with complex geometry.

The basic principle of the HFCVD process, illustrated in Figure 2.5, can be briefly described as following. Atomic hydrogen is produced in the filament activation zone. Then atomic hydrogen diffuses to the tool substrate, recombines at the methane (CH_4) molecule and forms the methyl radical CH_3, which is the actual growth species for CVD diamond deposition. Further recombination of atomic hydrogen at the substrate surface etches graphitic carbon at the growth front. Growth of the diamond film initially starts with crystallization at nucleation sites, the finally closed film forms when small nuclei islands intergrowth. Crystals with beneficial orientation to the substrate gradually overgrow adjacent crystals. Conventional deposition of CVD diamond therefore forms characteristic columnar structures with rough surfaces.

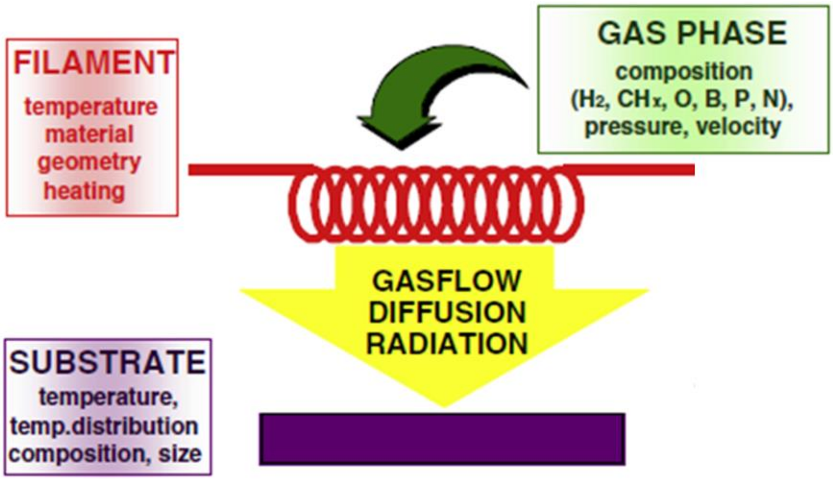

Figure 2.5. Principle of the HFCVD process [75]

Control of gas concentration ratio between H_2 and carbon-containing gas, such as CH_4, during the CVD process, determines the crystal shape and grain size of the deposited diamond coating [77]. The coating morphologies play an essential role in the properties of the deposited film, and consequently, the cutting performance of the diamond-coated tools. According to the grain size, diamond films applied for cutting tools can be divided into a microcrystalline diamond (MCD) coating and a nanocrystalline diamond (NCD) coating, presented in Figure 2.6(a) and (b) respectively [63, 78, 79]. Both types of coatings have their own strong and weak points in adhesion with WC-Co substrate, mechanical properties, and wear behavior. For instance, MCD film with high diamond quality and hardness can effectively resist abrasive impact carbon fibers. But its micro-sized diamond grains and high surface roughness may cause remarkable mechanical scratches on the machined surfaces of CFRP parts. On the other hand, the diamond grain refinement on the surface of NCD film reduces the surface roughness, while this diamond film contains more non-diamond impurities that may deteriorate their wear resistance.

Beneficial properties of the MCD and NCD coatings can be combined in multilayer structure, illustrated in Figure 2.6(c). This concept increases fracture toughness and the growth of cracks is prevented. In pure MCD or NCD structures, as shown in Figure 2.6(d) and (e), a crack in the coating, caused by tensile residual stress, may overcome the crystal boundaries and reach the carbide substrate below it during the machining.

By contrast, in the case of diamond multilayer coatings, any crack is “absorbed” by the next layer and cannot progress to the interface between the substrate and the first diamond layer. Thus, failure of the entire coating does not happen. Formation of compressive stresses due to different coefficients of thermal expansion between substrate and coating, and between micro-

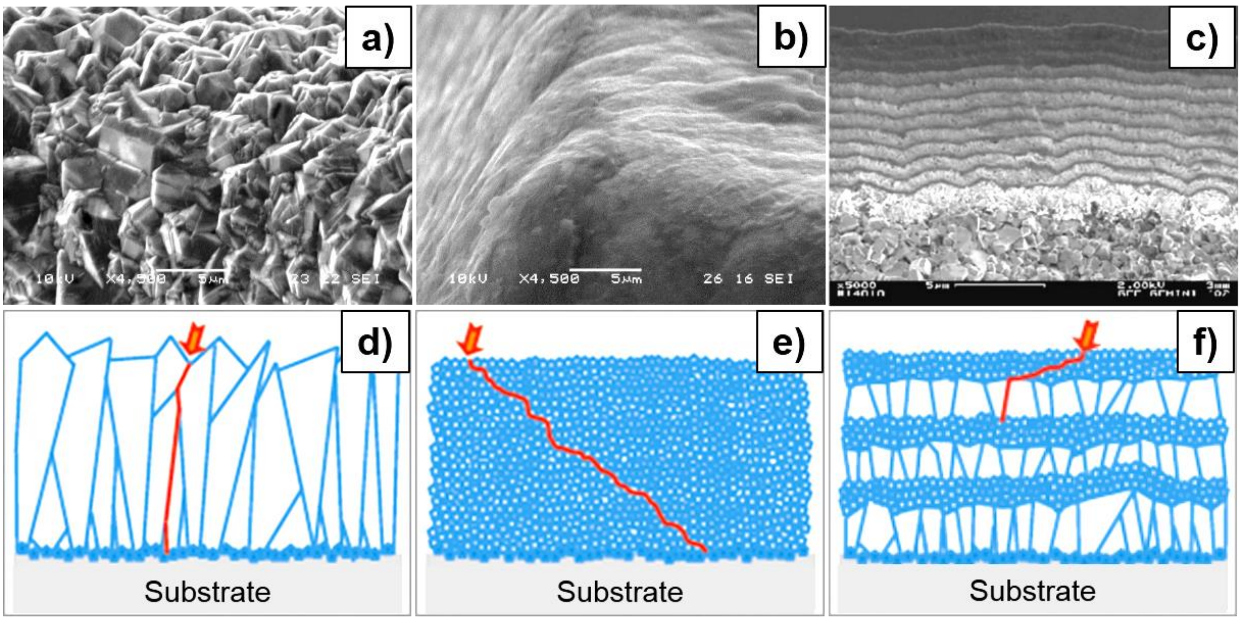

Figure 2.6. Kinds of HFCVD diamond coatings applied for cutting tools: (a) MCD, (b) NCD, (c) Multilayer and schematic representation of crack propagation (red line marked) for (d) MCD, (e) NCD, (f) Multilayer, respectively

and nanocrystalline diamonds, has the positive effect that vertical cracks change direction and rather grow parallel to the substrate at multilayer interfaces [80].

But it should be noted that such crack propagation stability of the multilayer diamond coating is not evidently confirmed by research society. On the other hand, application of dual-layer diamond films has widely described. Usually, the dual-layer film consists MCD layer, grown on a substrate directly, and NCD outlayer, grown in order to create smooth diamond film surface [76].

2.2.3 Optimizing adhesion of CVD diamond coatings to cutting tools

As discussed in Chapter 1, when diamond is deposited in cemented carbide materials such as WC-Co substrates, the cobalt will play a detrimental catalytic role in the diamond film adhesion. Any proposed solution must suppress the detrimental effect of cobalt and increase the mechanical interlocking between the film and the substrate in order to enhance the film interfacial toughness. The diamond-substrate interface requires the formation of strong interfacial chemical bonds between the diamond crystallites nucleated at the surface and the atoms of the substrate.

The most successful techniques, discussed in the corresponding papers, can be briefly divided on chemical etching procedures, creating intermediate layers, and selective thermal treatment [81]. The chemical etching procedures are related to the cobalt removal in depths ranging in about 3 – 10 μm from the substrate surface by etching the cobalt out of the surface. Intermediate layers halt the cobalt effect on the surface by interdiffusion barrier effects. Also, the layers reduce the thermal stresses caused during the diamond growth. Thermal treatment of the tool substrates applied to decrease the cobalt concentration on the substrate surface and to increase the surface roughness.

2.2.3.1 Wet-chemical etching method

The wet-chemical etching (WCE) in the surface of WC-Co substrates represent the most applied pretreatment method. This method has the purpose to produce a selective etching of the cobalt binder by using a two-step chemical process. First step is wet treatment in a Murakami solution with the aim of reconstruct and rough the surface by attacking the WC grains and exposing the Co binder. Then, a second wet etching in an acid solution to reduce the exposed cobalt at a certain depth determined by the etching time [82, 83]. Other methods have been proposed as well. Surface pretreatment with Copper Sulfate ($CuSO_4$) solutions involves a combination of Co etching and Cu depositing by a cementation reaction. During diamond deposition, the Cu dissolves into the Co binder resulting in a homogeneous interface [84].

Cobalt removal involves complicated processes that have to be matched carefully to each hardmetal type. Indeed, if the binder etch depth extends further into the substrate than the dimension of free-surface WC grains, the toughness of the interface will be severely degraded. By contrast, the removal of the binder to a depth less than the dimension of free-surface WC grains may allow chemical interaction between Co and diamond, during deposition process, with result poor bonding between the film and substrate.

2.2.3.2 Intermediate layers

Interlayer materials, used to avoid the cobalt-diamond interdiffusion, are normally deposited by PVD methods. The interlayer material must remain stable during the diamond deposition, provides a diffusion barrier between carbon and cobalt, and has a low thermal expansion coefficient to minimize internal stresses. A wide range of interlayer materials (amorphous carbon, metallic Cr, Ti, Ta, and ceramic CrN, TiC, and TiN) can be successfully applied by PVD on WC-Co substrates [85-87]. Although the application of interlayers becomes effective way of improving the adhesion of CVD diamond to hardmetals, this approach is rare in tool coating due to the high costs involved. Moreover, the interlayer leads to increase a cutting edge rounding, and consequently, thrust force and torque induced by a cutting process. Such phenomenon is undesired to CFRP machining point of view.

2.2.3.3 Thermal treatment

Thermal treatments of the hardmetal substrates can be applied to decrease the Co-concentration on the hardmetal surface and to increase the surface roughness. To avoid an additional process step, the thermal treatment can be applied prior to the diamond deposition in the CVD equipment. Using the hot-filament process Co evaporation, the tool substrates reach high temperatures (~1273 K) at low gas pressure. Ullram et al. reported [88] that the cobalt content on the substrate surface can be decreased from 6% to 1.5% within 3 hours and the surface roughness is similar to the WCE process results. The surface roughness is influenced by the temperature treatment due to the cobalt evaporation and WC crystal growth.

On the other hand, some tool substrate warp is expected due to the heat impact. It can be concluded, that thermal treatment is not suitable for tools with complicated shape.

2.2.3.4 Doping into diamond coatings

It is well known that boron doping technology was firstly proposed for modifying the electrical properties of the diamond film, mainly changing the insulating diamond film to a conductive film.

Nowadays, a mechanical properties of doped diamond films and its industrial applications have significant interest by related research society. For instance, Wang et al. [89] reported about improving in the solid particle erosion behavior of a boron-doped diamond (BDD) film compared with undoped ones. Recently, Gaydaychuk et al. [90] investigated wear and friction of heavily BDD films against steel at elevated temperature, as well as influence of boron concentration on diamond film oxidation resistance. The obtained data indicated that the coefficient of friction and the oxidation resistance decrease with increasing of boron concentration. The boron doping level also affects the growth rate, grain size, and diamond purity of deposited BDD films [91]. Regarding application doped films for cutting tools, Zhang et al. [62] reported that the adoption of boron and silicon could enhance the adhesion between the diamond coating and WC-Co substrate. Kalss et al. [92] reported in their study that the additive boron element can react with the Co and W to form stable Co-W-B compounds that only minimally affect the nucleation of the diamond.

Moreover, the covalent radius of the B atom (0.085 nm) is larger than the radius of the carbon atom (0.077 nm). Thus, the incorporation of B into the diamond structures may induce a certain amount of intrinsic tensile stress [93]. Because the residual stress in diamond film, deposited on the WC-Co, is mainly compressive residual stress, reducing of the absolute value of the total residual stress can be expected due to implement boron doping during film deposition.

Therefore, in addition to the mentioned in the previous sections pretreatment techniques, boron-doping technology can be considered as attractive method for enhancing the interfacial adhesive quality between the diamond film and the substrate.

2.2.3.5 Summary

Many solutions have been developed to increase the diamond adhesion when deposited on cobalt cemented carbide substrates, however, the majorities do not evaluate the practical conditions encountered when using commercial carbide tools existing in the market as the required substrate material. In most of these research studies, substrate samples correspond to WC-Co coupons with surface conditions that differ from the commercial tools. Moreover, the grinding effects in the surface/subsurface modifications of the carbide tool materials used as a substrate for further diamond deposition have not been evaluated enough. This analysis may exist as the internal know-how of CVD diamond tool makers, who normally optimize the process variables for particular customer applications.

One of the new ways of improving interface adhesion is doping into diamond coatings by chemical elements, as was described in previous section. However, indicated above results related to were obtained using conventional or modified WC-Co based twist drills, coated doped diamond films [59, 62, 63].

It is possible to conclude that the application of diamond-coated one-shot drills shows advantages in machining CFRP laminates, such as hole quality through lower delamination and burr defects, compared with the conventional twist drills. Nevertheless, not enough data is available regarding the cutting performance of the mentioned above one-shot drills, especially in terms of required film thickness, morphology, and its influence on drilled hole quality. Also, adhesion enhancement of diamond coatings deposited on such tools is essential to reach optimal tool life in economic aspects.

Therefore, the study aims at investigating the effect of boron-doped microcrystalline (B-MCD), boron-doped nanocrystalline (B-NCD), and commercial used undoped nanocrystalline (NCD) diamond coatings on cutting performance of WC-Co drills when drilling CFRP in terms of cutting forces, flank wear, drilled hole quality. Also, the adhesion of the mentioned above diamond coatings to the WC-Co drill's substrate is evaluated.

2.3 Experimental procedures

2.3.1 Applied drills

Drills of cemented tungsten carbide with cobalt (K01, WC-6 wt.% Co) specially designed for drilling CFRP, as shown in Figure 2.7, were selected for the experiments as substrates. The drill with a nominal diameter of 3.28 mm consists of two straight flutes with two-point angles of the cutting edges, as 103° and 28°, respectively. Other drill sizes: total length is 83 mm, cutting edge length is 36.5 mm, and shank diameter is 6 mm. The shown cutting edges are described as primary, secondary, and tertiary, following the frequently used terminology [94].

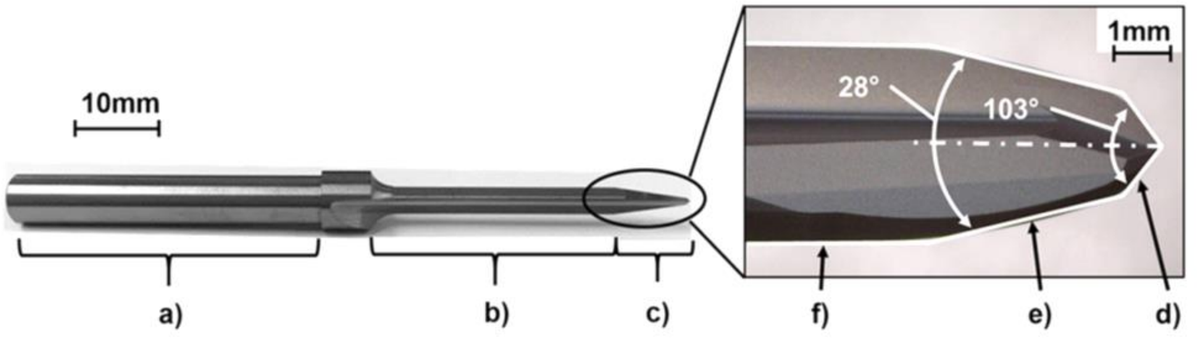

Figure 2.7. WC-Co drill for CFRP drilling: (a) drill shank side, (b) reamer cutting side, (c) drill cutting edge side, (d) primary cutting edge, (e) secondary cutting edge, and (f) tertiary cutting edge.

Compared with conventional twist drills, the drilling process provided by the selected drills has inherent features. The primary cutting edges perform pre-drilling. Then the secondary cutting edges remove CFRP workpiece defects induced by the drill primary cutting edges with a chisel and make the holes close to the nominal size. Afterward, the tertiary cutting edges perform reaming the holes to final diameter with acceptable roughness of hole walls. Therefore, such drill shape can be described as the one-shot drill.

2.3.2. Substrate preparation and deposition of the diamond coatings

Before a diamond deposition, the selected drills were pretreated. The frequently used WCE method was optimized for selected substrates and included several steps as presented in Figure 2.8. Initially the drills were ultrasound cleaned in acetone with the aim to remove a grease contamination. Then the drills were etched with Murakami reagent (1:1:10 $KOH+K_3Fe(CN)_6$ $+H_2O$) and nitric acid solution (1:9 HNO_3+H_2O), consequently. Followed 4rd step consists scratching surfaces by diamond powders solution in an ultrasonic bath in order to remove "deformed" layer remains. Further 5th and 6th steps create required tool surface roughness and Co depletion outer layer, respectively. The 2nd and 5th steps carried out immersion the tool substrates into Murakami reagent by special rotatable holder. The tool substrate decobaltation was performed on the steps 3rd and 6th, by immersion ones into an ultrasonic bath with nitric acid solution. After each the process step, the treated substrates were cleaned ultrasonically by immersion into purified water.

Finally, the etched drills were seeded with diamond seeds ≈4 nm of average particle size by ultrasonically in a suspension of diamond powder in purified water.

Figure 2.9 presented SEM images of original and WCE treated drill surface for comparison. It can be concluded that the applied WCE process provided uniform rough tool surfaces without grinding traces.

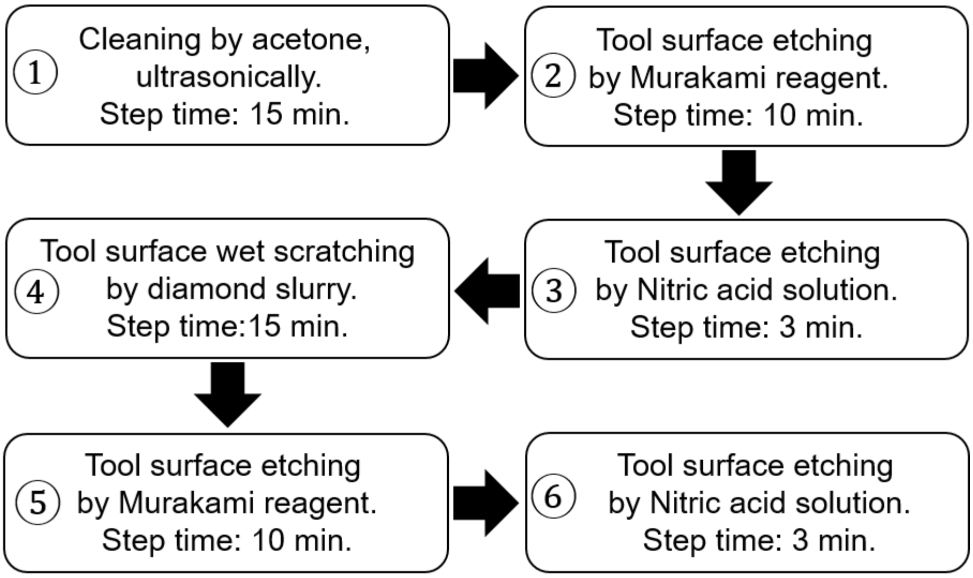
① Cleaning by acetone, ultrasonically. Step time: 15 min.
② Tool surface etching by Murakami reagent. Step time: 10 min.
③ Tool surface etching by Nitric acid solution. Step time: 3 min.
④ Tool surface wet scratching by diamond slurry. Step time:15 min.
⑤ Tool surface etching by Murakami reagent. Step time: 10 min.
⑥ Tool surface etching by Nitric acid solution. Step time: 3 min.

Figure 2.8. The WCE process for WC-Co substrate pretreatment.

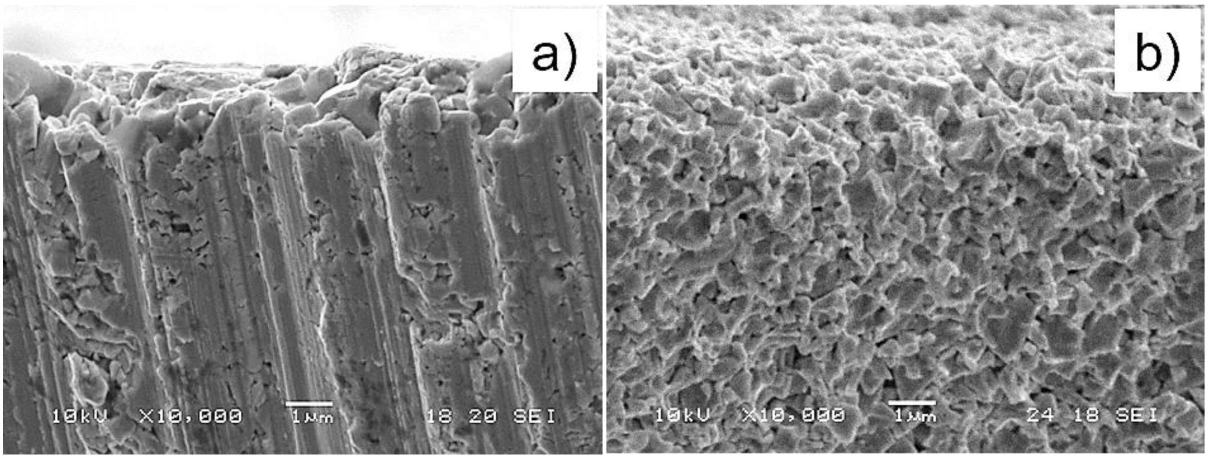
a)
10kV X10,000 1μm 18 20 SEI
b)
10kV X10,000 1μm 24 18 SEI

Figure 2.9. The WC-Co substrate morphology: a) original, b) after WCE process

The three types of required diamond coatings, boron-doped MCD (B-MCD), boron-doped NCD (B-NCD), and undoped NCD (NCD), were grown on the drill WC-Co substrates using the HFCVD method in a home-made experimental setup shown in Figure 2.10. For this study, a reactor with six parallel linear tungsten wire filaments is mounted in the chamber. The diameter and length of the filaments were 0.2 mm and 280 mm, respectively. The filament - substrate distance was kept 10 mm for all deposition processes. Figure 2.11 shows schematic

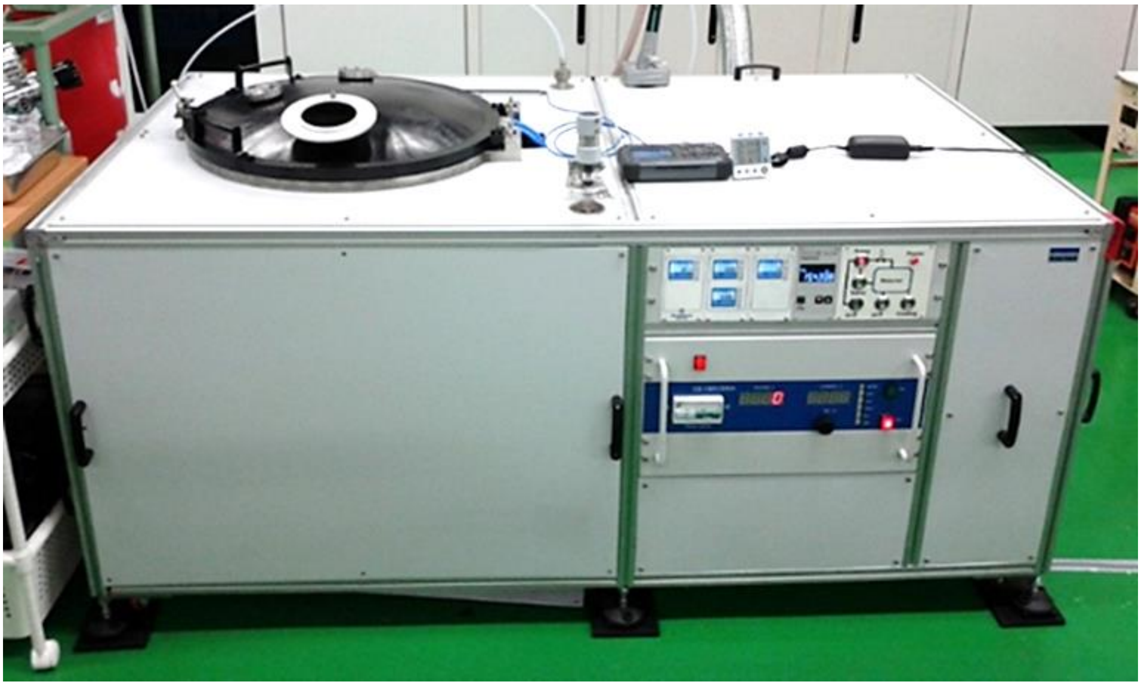

Figure 2.10. HFCVD experimental setup

diagram of the filament's arrangement and drill setting into the chamber of the HFCVD setup. A substrate temperature was monitored by Type K thermocouples installed to the reactor, as shown in Figure 2.12.

A mixture of CH_4 and H_2 was used as precursor gas in the main growth and nucleation deposition process stages. Boron species were incorporated into the coating during the growth process stage by adding a mixture of an evaporated liquid solution of trimethoxyborane ($(CH_3O)_3B$) with acetone and H_2. All gases and the evaporated liquid solution are directly introduced into the chamber, flow rates of it are controlled by mass flowmeters. Common deposition parameters are shown in Table 2.2. The B/C atomic ratio is determined by pre-mixing the acetone and the $(CH_3O)_3B$ according to a certain proportion. In NCD and B-NCD growth processes, relatively lower pressure is selected in order to increase mean free paths of active radicals forming around hot filaments. Such radicals will have fewer collisions when moving to substrate surfaces and induce much higher nucleation density. Moreover, mainly owing to the more exothermic reactions caused by the more radicals moving to the substrate surfaces, especially the recombination of H atoms that contributes much to the substrate temperature, at the same filament temperature, substrate temperatures in NCD and B-NCD growth processes are higher than in B-MCD growth process [77, 95]. After each deposition process finished, the diamond coated drills were cooled down under the H_2 atmosphere into the chamber.

As a result, the required types of diamond coating with a film thickness of about 8 μm were deposited on all tested drills.

In this study, the pretreated substrates and deposited layers were examined in terms of surface morphology, grain sizes by scanning electron microscope (SEM JSM5510, JEOL), and carbon structure by Raman microscopy (RAMAN-11, Nanophoton). Coating surface roughness was measured by a laser microscope (OLS4100, Olympus). Indentation tests were carried out to evaluate adhesion strength between the deposited coatings and WC-Co (Rockwell hardness testing machine ARK-600, Mitutoyo).

Table 2.2 Deposition process parameters:

Parameters:	NCD	B-MCD	B-NCD
Flow of H_2 [sccm]	700	700	700
Flow of CH_4 [sccm]	26	30	24.5
B/C atomic ratio [ppm]	-	8000	1600
Process pressure [Pa]	600	2660	600
Substrate temperature [K]	1123±323	1073±293	1123±323
Duration [h]	21	16	21

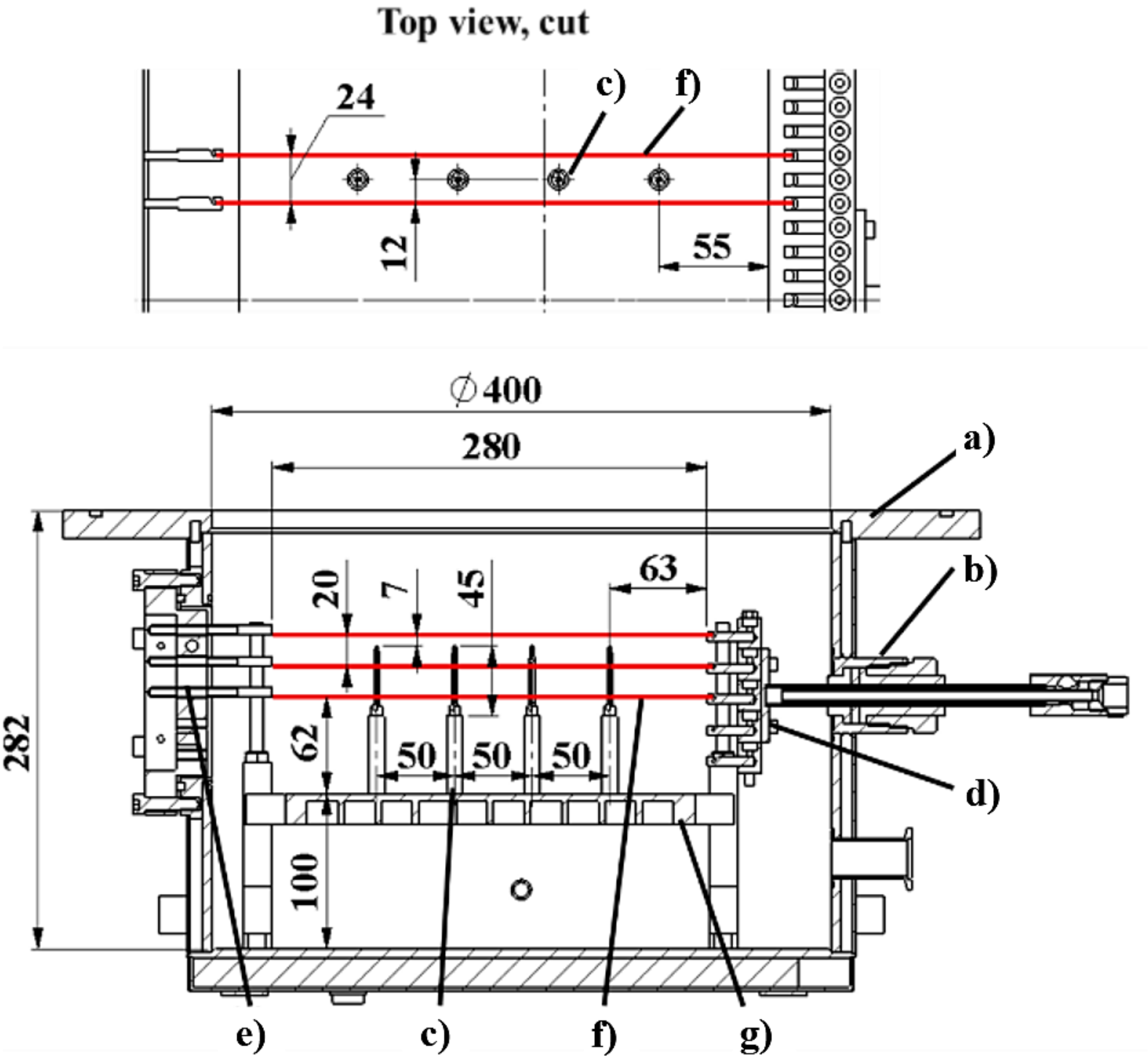
Top view, cut
24
c)
f)
12
55
∅400
280
a)
b)
20
7
45
63
282
62
50
50
50
100
d)
e)
c)
f)
g)

Figure 2.11. Schematic diagram of hot filaments arrangement and drill setting into the HFCVD setup chamber: (a) Chamber; (b) Current feedthrough; (c) Drills with ceramic holders; (d) Filament holder; (e) Grounded filament holder; (f) Hot filaments; (g) Table

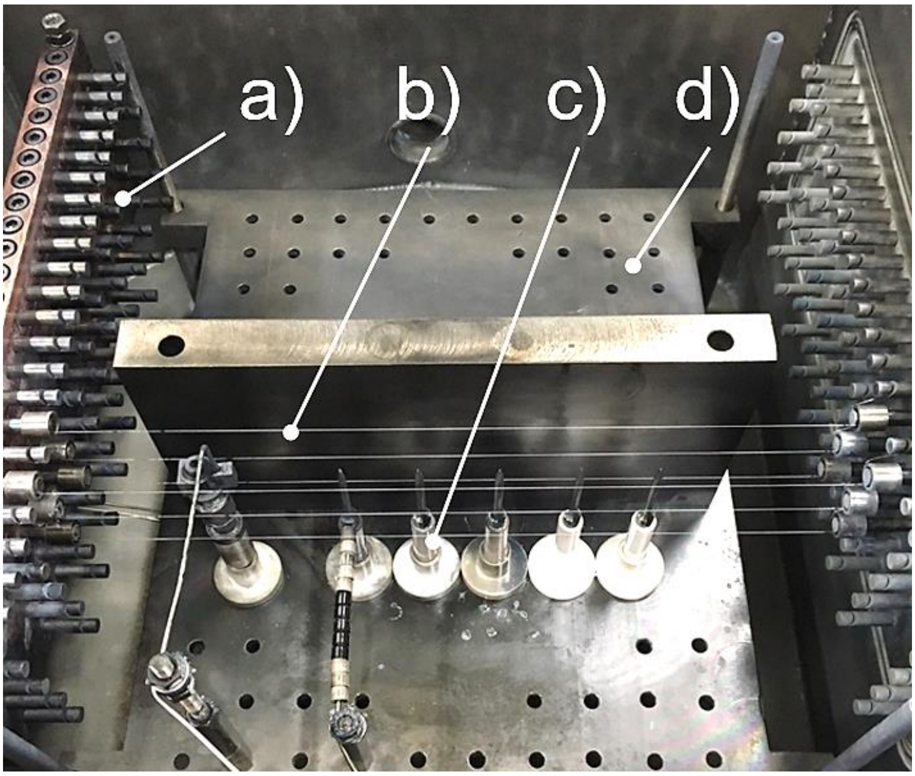

Figure 2.12. Experimental CVD setup chamber with installed drills: (a) Reactor, (b) Filaments, (c) Drills with ceramic holders, (d) Table

2.3.3. Drilling tests

In this study, CFRP laminates with a thickness of 8 mm and dimensions 250 mm x 100 mm were used as workpieces. The workpiece consists of 42 unidirectional pre-impregnated (prepreg) layers of P2352W-19 (T800SC/3900 series, TORAY) with (0/90/-45/0/45/90/-45/0/45/90/-45/0/45/90/-45/0/45/90/-45/02)s lay-up, in which the volume content of the carbon fiber is about 60%. The composition of applied prepreg and mechanical properties of the CFRP laminate is presented in Tables 2.3 and 2.4. These CFRP laminates were produced as part of an industrial manufacturing process and according to requirements of the aviation sector. Such laminates are currently used in multiple structural elements of commercial aircraft. The mechanical properties, stated in technical specifications defined by Boeing, had ensured by the testing on representative coupons of the manufacturing process. Before drilling, the laminates were cut by a waterjet machine according to the mentioned before sizes.

All drilling tests were performed using a vertical milling center OKUMA MD-45VA with the following cutting parameters: feed rate f = 0.06 mm/rev, drill rotation n = 8,000 rpm with corresponding cutting speed *V* = 82.4 m/min. These cutting parameters already utilize for machining CFRP commercial products by the NCD coated one-shot drills applied in the current study tests. No coolant was used during the tests. The experimental setup for the drilling tests is shown in Figure 2.13. For comparison of cutting performance, non-coated WC-Co drills were applied as well. Their drill shapes, angles, and dimensions are identical to the coated drills.

The cutting performance was evaluated through the drilling of series of consecutive holes in the workpiece. During the experiments, thrust force and torque were measured using a rotating dynamometer "Kistler 9125A" with a charge amplifier "Kistler 5237" and monitored on a personal computer using data acquisition software DynoWare 2.5. In addition, drill flank wear was measured periodically using a digital microscope VHX-1000SP (Keyence).

Table 2.3 Composition of prepreg P2352W-19 (TORAY):

Resin content	35%
Fiber type	T800SC-24000
Fiber diameter	5 μm
Fiber tensile strength	5880 MPa
Fiber tensile modulus	294 GPa
Strain	2%
Fiber density	1.8 g/cm^3
Fiber areal weight	192 g/m^2

Table 2.4 Mechanical properties of the CFRP laminate:

Fiber volume content	60%
Flexural strength	456 MPa
Flexural modulus	39 GPa
Strain	1.25%
Density	1.54 g/cm^3

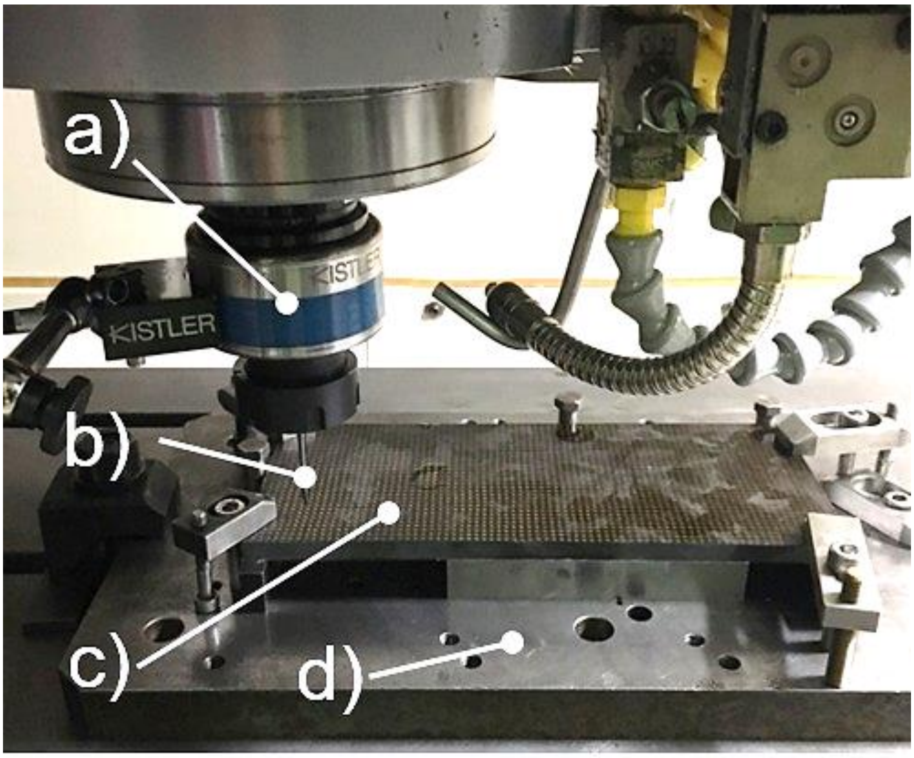

Figure 2.13. Experimental setup for drilling tests: (a) dynamometer, (b) tested drill, (c) CFRP workpiece, and (d) fixture

2.4 Experimental results and discussion

2.4.1 Characterization of deposited diamond coatings

SEM images of the surface morphology of the diamond-coated drills are shown in Figure 2.14. Figure 2.14(b) shows that the undoped NCD coated drill has a smooth film surface with ultrafine grains, which are not clear resolvable with the applied magnification of used SEM. On the other hand, Figure 2.14(c) shows the morphology of the B-MCD coated drill. With an average size of ≈ 2 μm, randomly oriented faceted diamond grains were observed at different points of cutting edges of the drill. Further, Figure 2.14(d) shows an SEM image of the B-NCD coated drill with the smooth wavy surface of ultrafine grains.

In continuation, Figure 2.15 shows diamond surface morphologies observed on the flank area of the coated drills by the laser microscope. Compared the surfaces shown in Figure 2.15(a) and (c), a significant distinction between the NCD and B-NCD diamond films can be seen. The B-NCD film has a homogeneous smooth surface with low visible fine ballas grains. In contrast, the NCD film shows a non-uniform surface with larger ballas grains. The observed phenomenon

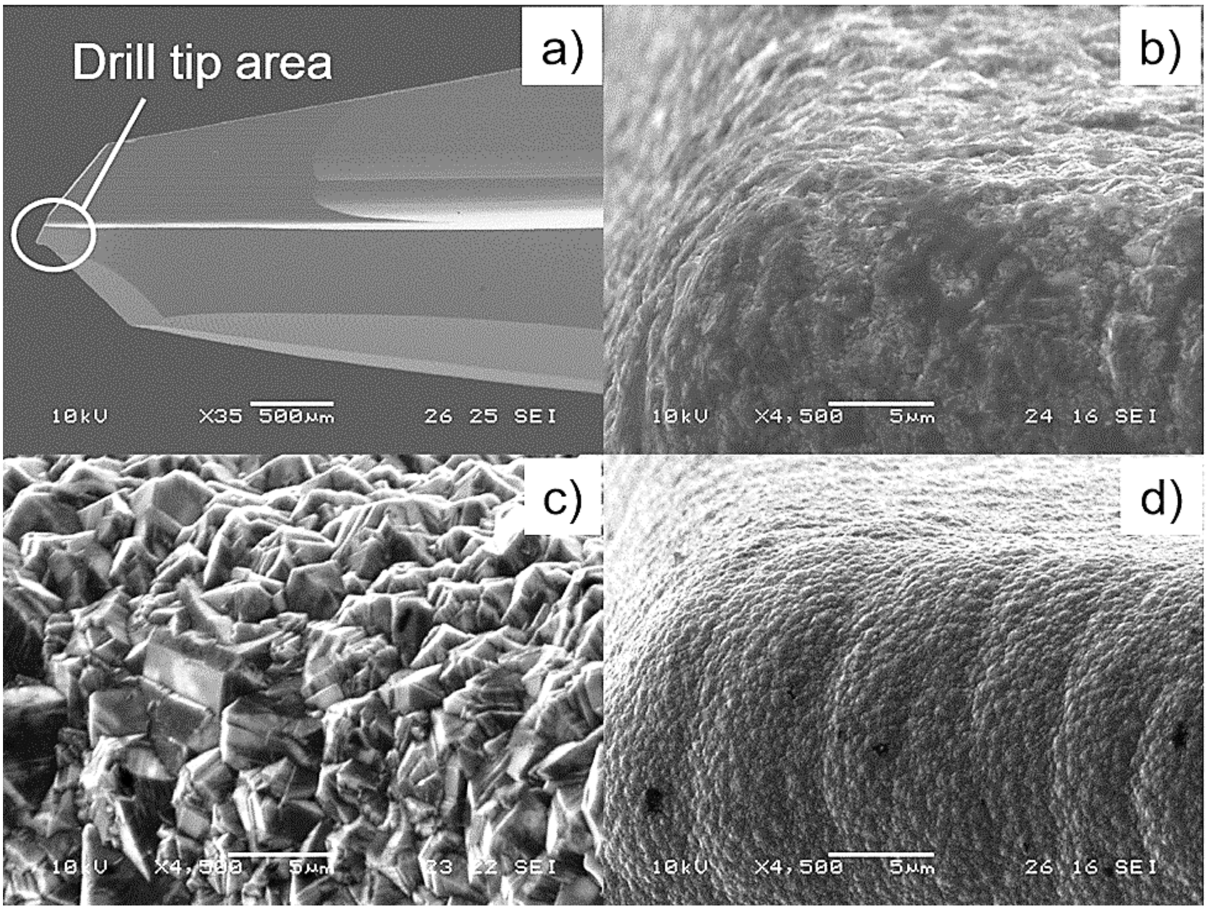
a)
Drill tip area
10kV X35 500μm 26 25 SEI
b)
10kV X4,500 5μm 24 16 SEI
c)
10kV X4,500 5μm 23 22 SEI
d)
10kV X4,500 5μm 26 16 SEI

Figure 2.14. SEM images of surface morphologies observed on drill tip area of the coated drills (a) for: (b) NCD, (c) B-MCD, and (d) B-NCD coatings.

can be described difference in the deposition process parameters. Application liquid solution of trimethoxyborane with acetone for boron doping increased the oxygen/carbon ratio during the growth duration of the B-NCD film and provided decreasing in the grain size. The B-MCD film, as shown in Figure 2.15(b), exhibits a uniform rough surface with sharp grains. After, diamond film surface roughness was measured in different points of the coated drills, and the average value of the roughness was considered. Surface texture parameter *S*a, as arithmetical mean height, based on ISO 25178 ‘‘Surface Texture,’’ is applied for evaluation. The scan size was determined by the optical magnification of the system (100 ×) in resulting surface area of 129 mm × 129 mm. The B-MCD coated drill has a rough surface with a *S*a value around 340 nm due to large and faceted micro-sized diamond grains. However, the *S*a values of the nano-sized diamond surfaces are near 131 nm of NCD and 74 nm of the B-NCD coated drills, respectively, due to the film’s grain refinement.

Raman spectra of the deposited diamond coatings are displayed in Figure 2.16. In the Raman spectra of the NCD coating, several visible peaks can be identified. The peak at 1337.3

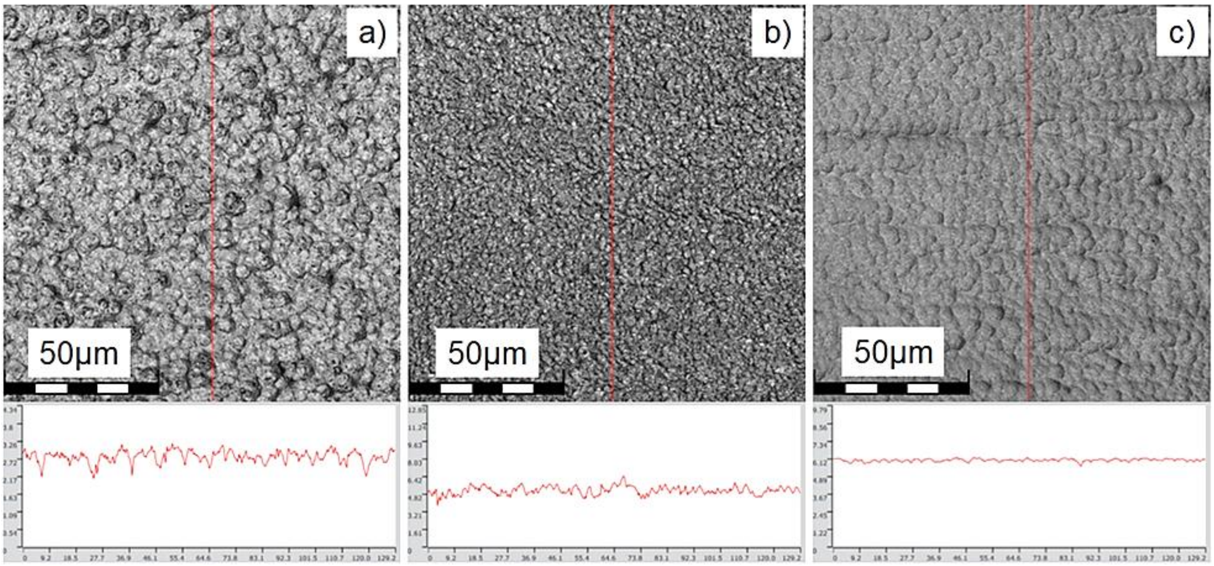

Figure 2.15. Topographic images with surface profiles, observed on a flank area of cutting edge, for: (a) NCD, (b) B-MCD, and (c) B-NCD coated drills, respectively.

cm^{-1} is a small diamond peak, while the peaks at 1385.6 and 1550 cm^{-1} are D and G peaks of amorphous carbon, respectively [96]. Then, two peaks, as 1152 and 1489.2 cm^{-1}, are confirmed to trans-polyacetylene [97]. Regarding the B-MCD coating, the Raman spectra show two broad peaks at 500.7 and 1223.8 cm^{-1} associated with boron doping. Also, it shows the diamond peak at 1329.1 cm^{-1}, and G peak at 1532 cm^{-1} as amorphous carbon [98, 99]. On the other hand, Raman spectra of the B-NCD coating show a relatively weaker peak at 517.8 cm^{-1} and not a clear visible peak near 1200 cm^{-1} compared with the B-MCD coating. Such difference may be caused by lower boron incorporation in the B-NCD film due to the low B/C atomic ratio during the deposition process. Besides associated with boron doping peaks, the Raman spectra of the B-NCD coating have a diamond peak at 1335.3 cm^{-1}, D and G peaks at 1360.5 cm^{-1}, and 1561.4 cm^{-1}, respectively. Also, two peaks associated with trans-polyacetylene at 1140.9 and 1472.1 cm^{-1} were observed.

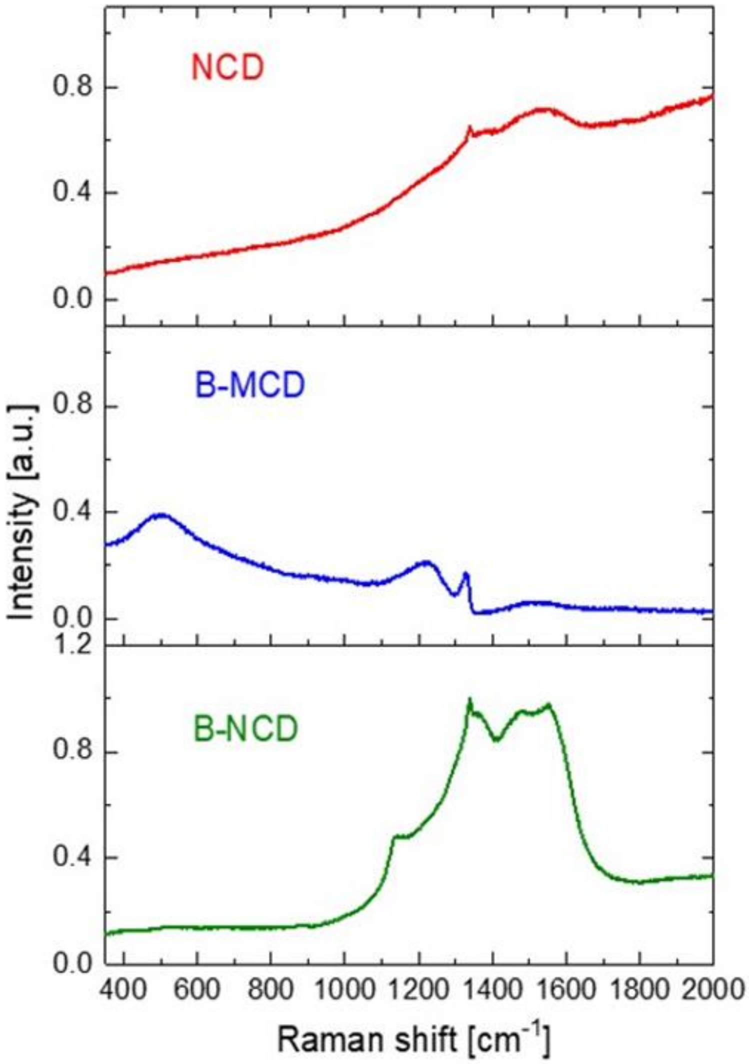

Figure 2.16. Raman spectra of NCD, B-MCD and B-NCD coated drills, using green (λ = 532 nm) excitation

In order to evaluate the adhesive strength between the deposited diamond coatings and the drill's substrate, indentation tests were carried out using a Rockwell hardness testing machine with a diamond indenter, which has a conical angle of 120° and radius of curvature at the tip 0.2 mm. Each diamond coated drill was tested under the load of 1471 N. It should be noted that applied drill shape with planar faces allows performing the indentation tests directly on it. Figure 2.17 shows SEM images of surface morphologies of the coated drills after indentation tests. For the NCD coated drill, a large area of coating peeling around the indenter trace was observed. Compared with the NCD coated drill, the peeled areas on B-MCD and B-NCD coated drills were relatively more minor. On the other hand, the B-NCD coating does not show an

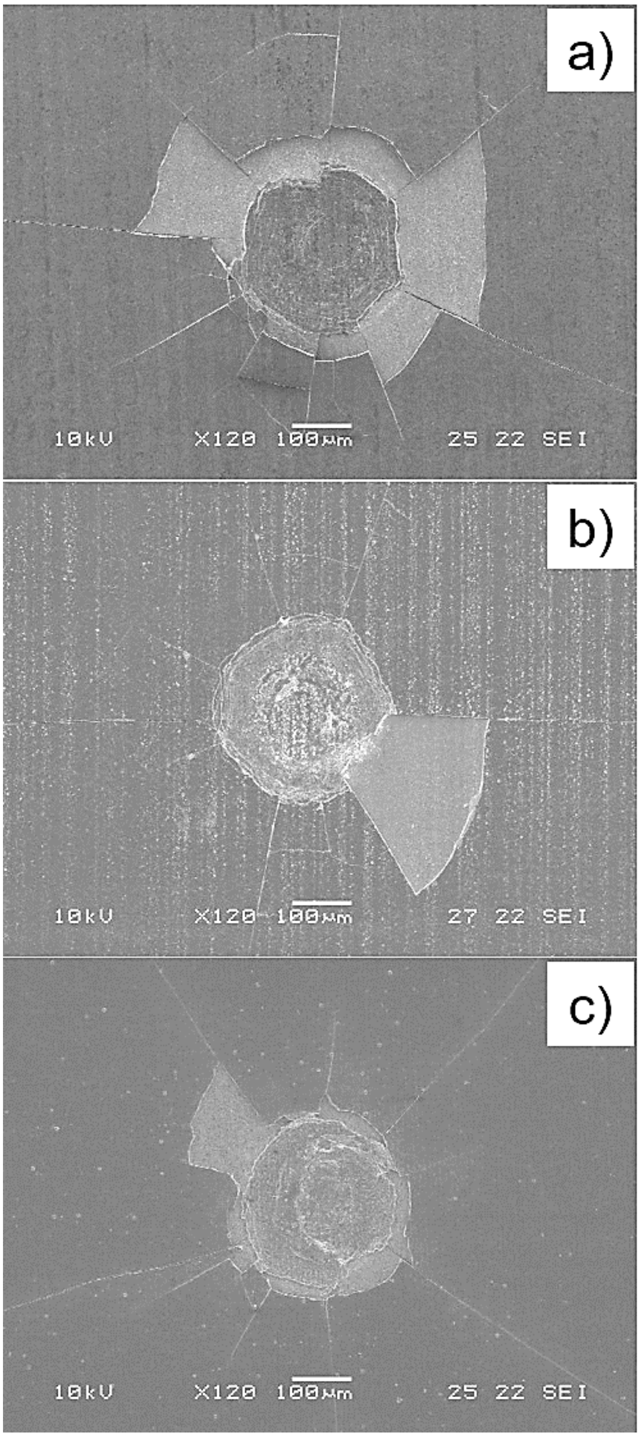
a)
10kV X120 100μm 25 22 SEI
b)
10kV X120 100μm 27 22 SEI
c)
10kV X120 100μm 25 22 SEI

Figure 2.17. SEM images of indentation morphologies, obtained by Rockwell testing machine with a load of 1471 N, on: (a) NCD, (b) B-MCD, and (c) B-NCD coated drills, respectively

advantage in adhesion. For incomplete agreement, other reasons for such adhesion phenomenon can be proposed. Wang et al. [95] reported in their study that boron-doped NCD film, in which the compressive residual stress is lower than in undoped MCD film, shows a larger film removal area compared to the undoped MCD due to its poor mechanical cohesion. Therefore, a reduction in the residual stress caused by boron doping cannot compensate for the influence of diamond film impurities on its adhesion.

Based on the Raman spectra characterization and indentation test results, it can be concluded that the adoption of boron can enhance the adhesion between the diamond films and the WC-Co substrates.

2.4.2 Drill flank wear evaluation

Usually, tool wear performance reflects the tribological and physical properties at the tool-workpiece interface in the actual cutting process and is a critical point in the tool life durability and cutting performance. In the drilling tests, tool wear was evaluated as maximum flank wear land width (*VB*max) as a function of drilled hole number, as shown in Figure 2.18. The results, shown in Figure 2.18, indicate that progress of the *VB*max values for all diamond coated drills can be divided into three typical stages, as the initial wear under drilling ~ 150 holes, gradually increased wear between ~ 150 and 500 of drilled holes and rapid wear stage, respectively.

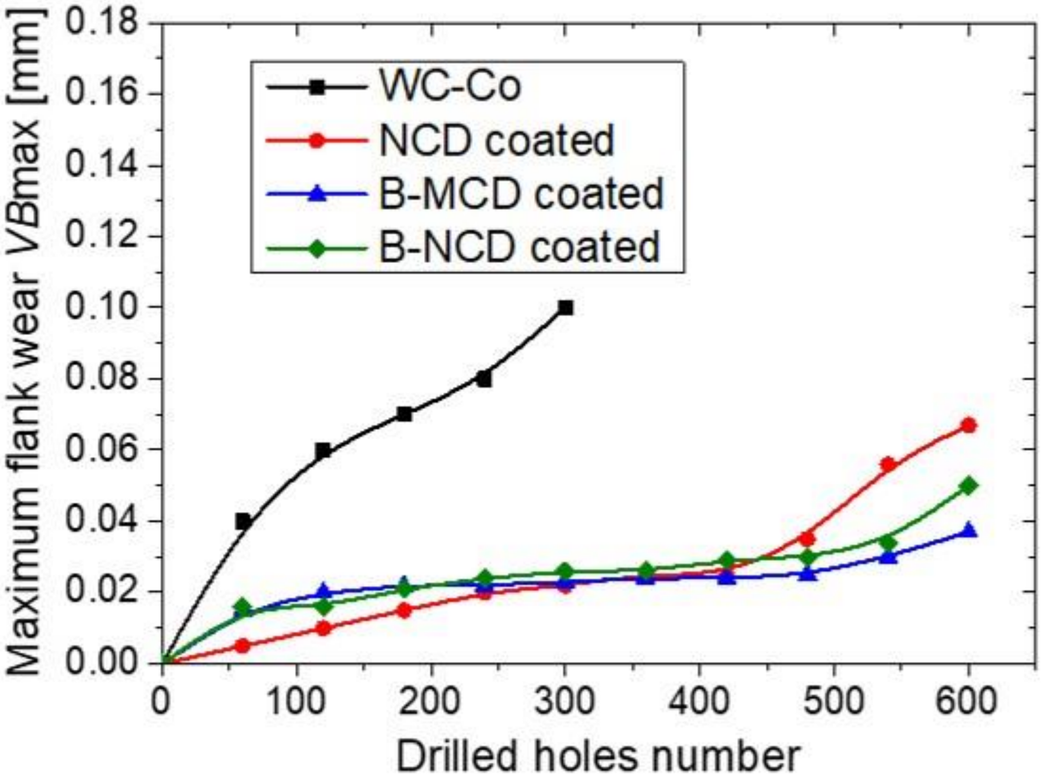

Figure 2.18. Variations of maximum flank wear as a function of drilled hole number

On the other hand, flank wear progress of the non-coated WC-Co drill is rapidly increased and achieved a value of 0.1 mm after drilling 300 holes. Then, drilling test with the drill was stopped due to poor drilled hole quality, described in the following section.

Some minor differences between the flank wear values associated with their different diamond coating properties were observed until achieving 500 holes regarding the diamond-coated drills. Hereafter, the flank wear values have rapidly increased, especially for NCD and B-NCD coated drills, while the B-MCD coated drill kept a lower flank wear value. Previous cutting tests confirm that coating peeling occurs for the diamond-coated drills during the drilling duration. The diamond film begins to peel off, depending on the applied load upon the film surface and the film-substrate adhesion. According to the impact dynamic models based on Hertz's theory of contact, continuous or intermittent impacts on the coated cutting edge can induce shear stress and minor cracks beneath the film surface. Because adhesion of the diamond film and the substrate is weaker than inside the same material, the formation and propagation of cracks along with the film-substrate interface during the drilling of CFRP occurs. Moreover, the thickness of the diamond films is decreased during drilling under the abrasive effect of the carbon fibers, and, therefore, film durability against crack propagation is reduced as well. Thus, enhanced film-substrate adhesion is essential for increase the tool lifetime. In contrast, abrasion of the edges due to the hard carbon fibers without observed chipping or micro-fracture is seen as the predominant wear mechanism on the non-coated WC-Co drills. The cobalt binders have removed during drilling, and many carbide grains dislodged out from the tool surface. Moreover, the tool wear phenomena that were observed in this study are in good accordance with references [59, 100].

Figure 2.19 shows the wear morphologies of the diamond-coated drills after drilling 600 holes. For NCD coated drill, the diamond film was removed along the cutting edge under the cutting, and the worn substrate has been observed clearly, as shown in Figure 2.19(a) and (b). On the other hand, for both boron-doped diamond coated drills, the worn diamond films with localized film flaked areas are visible, as shown in Figure 2.19(c) to (f).

Moreover, the B-MCD coated drill showed an advantage in the tool wear durability. This phenomenon could be attributed to enhanced adhesion between the diamond film and WC-Co substrate by application of appropriate boron doping level [101].

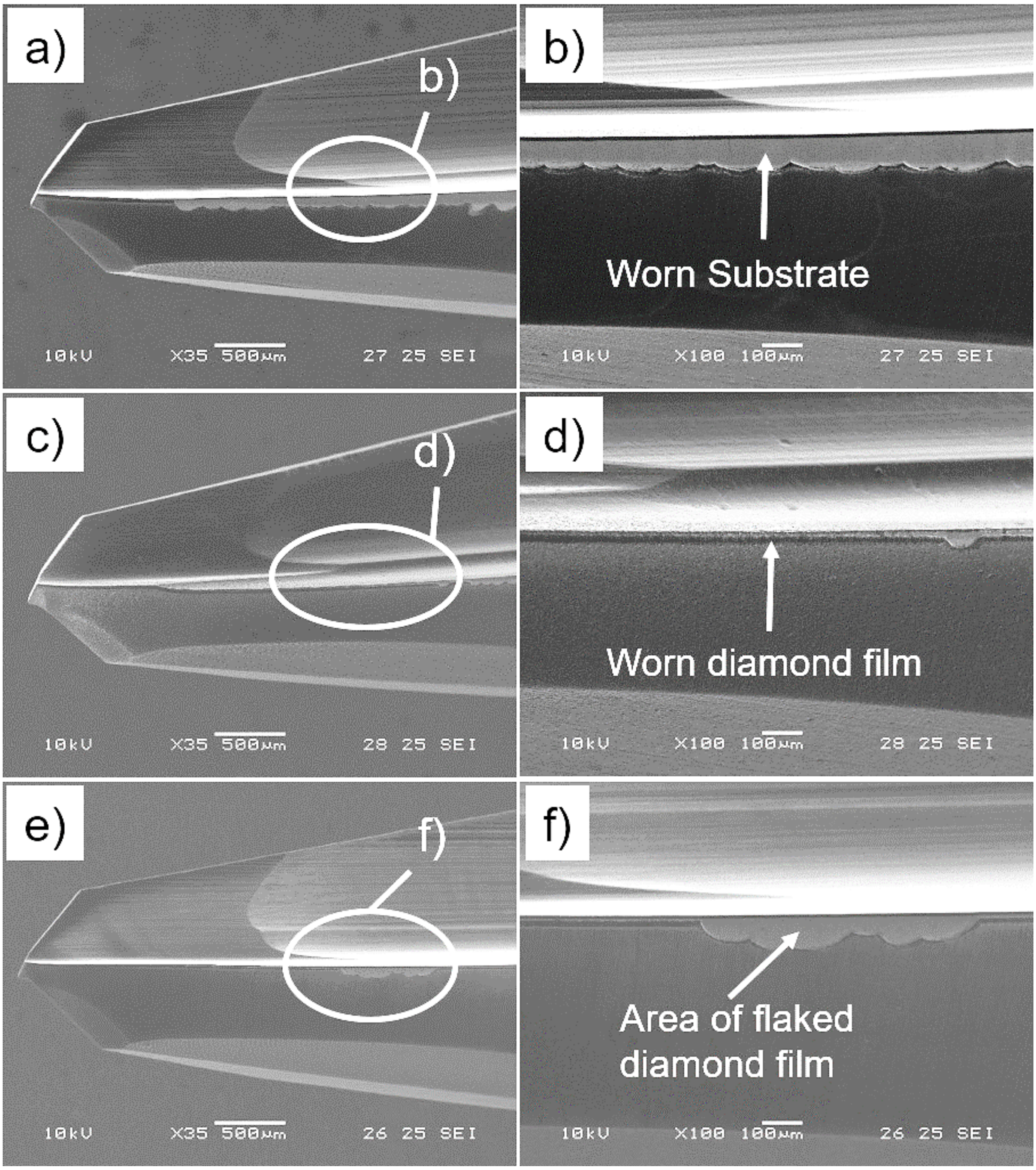
a)
b)
10kV X35 500µm 27 25 SEI
b)
Worn Substrate
10kV X100 100µm 27 25 SEI
c)
d)
10kV X35 500µm 28 25 SEI
d)
Worn diamond film
10kV X100 100µm 28 25 SEI
e)
f)
10kV X35 500µm 26 25 SEI
f)
Area of flaked diamond film
10kV X100 100µm 26 25 SEI

Figure 2.19. SEM images of the drills after drilling 600 holes: (a, b) NCD coated drill, (c, d) B-MCD coated drill and (e, f) B-NCD coated drill

2.4.3 Thrust force and torque evaluation

It is known that a thrust force and torque induced during drilling are key factors that influence CFRP hole quality. The source of these cutting forces may be a combination of two factors. First is the drilling resistances, including the composite's matrix shear force and fiber breaking resistance, generated when drilling the workpiece. The second factor is frictional resistances, which occur between the tool's surfaces and the hole sides of CFRP. As already reported, that tool wear behavior mainly influences the thrust force and the torque values through increased cutting edge rounding under abrasive action of the CFRP fibers. Further, cutting edge with large roundness has provided more significant cutting force by increasing the feed direction's contact area. Therefore, the thrust force and torque have high sensitivity to tool flank wear.

Figure 2.20 shows thrust force variations as a function of drilled hole number. Thrust force induced by the WC-Co drill increased rapidly as the number of holes increased, which correlated with flank wear results shown in the previous section. On the other hand, thrust forces induced by the NCD and B-NCD coated drills have increased until ~ 200 drilled holes. Further, the forces gradually decreased to the rest of the tests. In comparison, the thrust force induced by the B-MCD coated drill is progressively reduced during the drilling test. Such results could be associated with epoxy matrix softening effects from cutting heat caused under dry friction between diamond surfaces of the coated drills and CFRP workpiece. Xu et al. [41] described the CFRP matrix softening effect in their study. The difference with approximate value ~ 5 N has occurred between thrust forces induced by the NCD and B-NCD coated drills, as shown in Figure 2.20. That can be assumed due to the difference in coating surface roughness. Indeed, as described in Section 2.4.1, the NCD film shows Sa=0.131 µm against Sa=0.074 µm, measured on the B-NCD film. Rougher surfaces of the NCD coated drill, especially in drill flutes, hindered evacuating CFRP chips from the hole outward.

Figure 2.21 shows torque induced by the examined drills as a function of drilled holes' number. As shown in Figure 2.21, the torque values are not increased significantly during the drilling tests, except for the WC-Co drill, and they have almost similar trends with the thrust forces. Also, the torque curves have sensitivity to friction effects between the hole surface and CFRP chips accumulated in flutes of the examined drills.

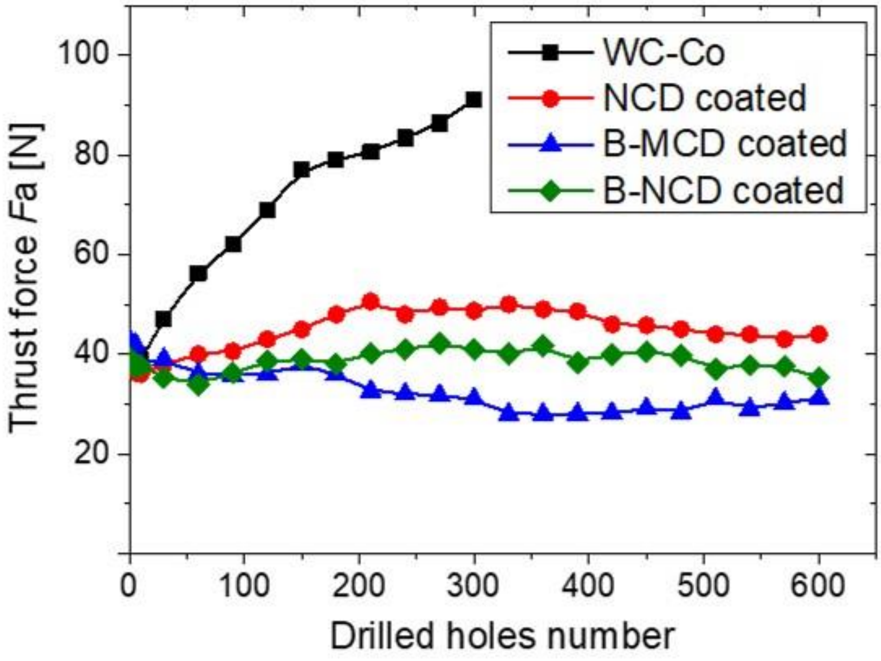

Figure 2.20. Variations of the thrust force as a function of drilled hole number

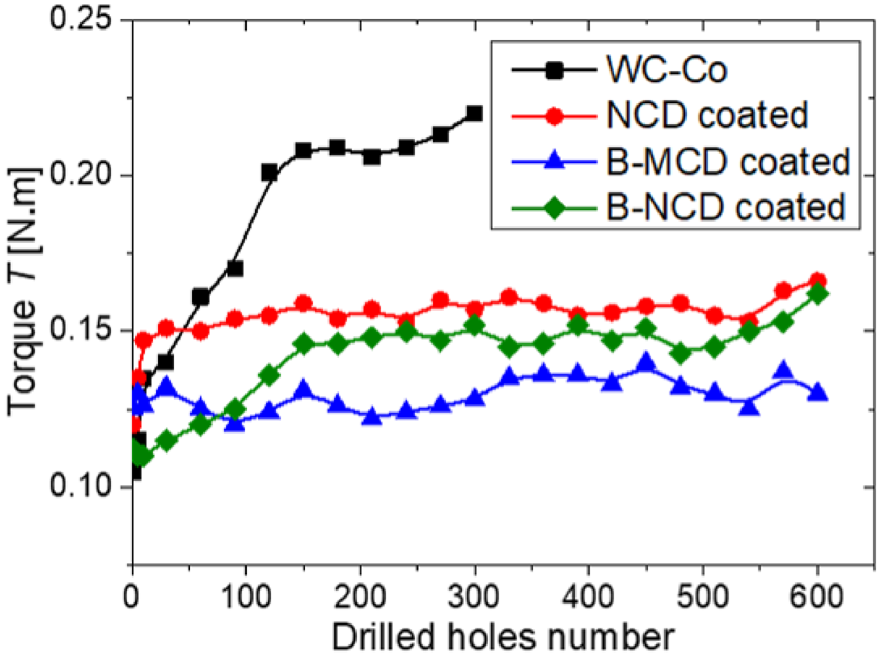

Figure 2.21. Variations of the torque as a function of drilled hole number

It can be suggested that the diamond-coated drills have produced lower thrust forces and torque values compared with the non-coated drill. The B-MCD coated drill produces the lowest thrust force and torque compared to the coated drills.

2.4.4 Hole quality evaluation

As discussed in Chapter 1, drilling-induced CFRP delamination commonly occurs at the hole entry and hole exit of the drilled hole periphery. According to the formation mechanism, the hole entry damage is usually named peel-up delamination, while the hole exit damage is called push-out delamination. In this study, both types of CFRP delamination induced by the compared drills were evaluated through the method proposed by Chen [35]. Delamination factor *F*d is defined as the ratio of the maximum diameter of the damaged zone (*D*max, mm) to the nominal diameter of the hole (*D*o, mm), and two circles are concentric, as shown in Figure 2.22.

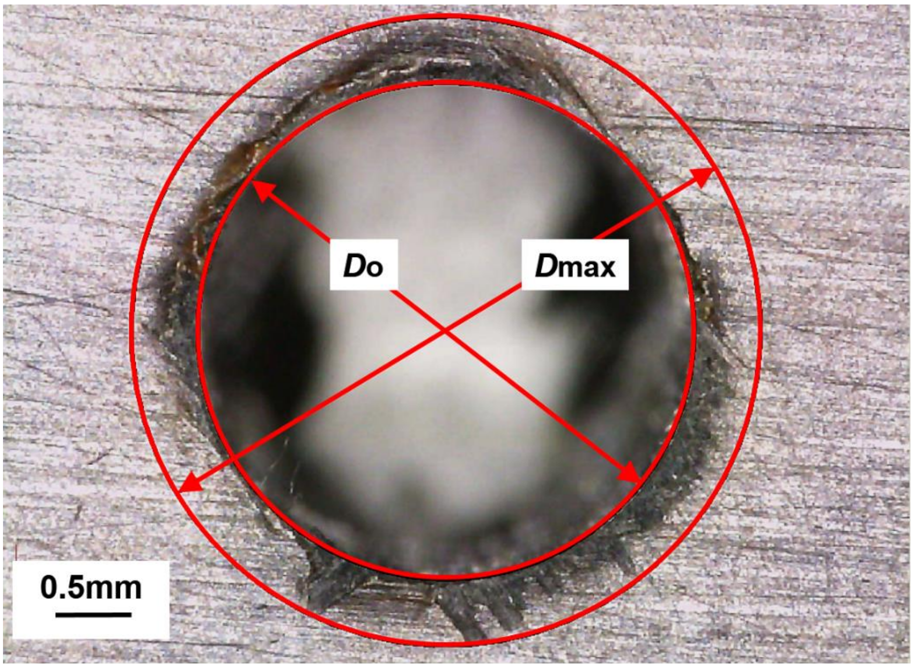

Figure 2.22. Schematic diagram of delamination factor (*F*d)

Then, the value of *F*d can be expressed as:

$$F_d = D_{max}/D_o, \qquad \text{(Eq.1)}$$

The maximal diameter of the damaged zone around each hole was measured with a digital microscope (VHX-1000SP, Keyence). Figure 2.23 shows a variation of measured *F*d at hole entry of the laminates as a function of drilled hole number. While Figure 2.24 shows the variation of the delamination factor at hole exit sides of the laminates as a function of drilled hole number.

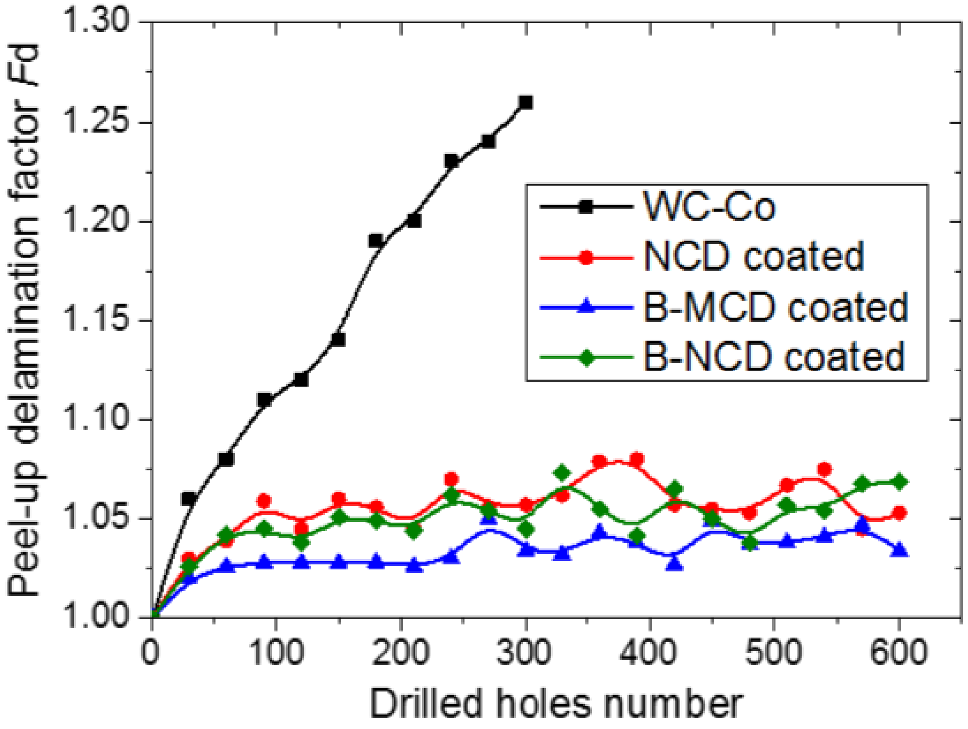

Figure 2.23. Variations of the delamination factor on entry hole side as a function of drilled hole number

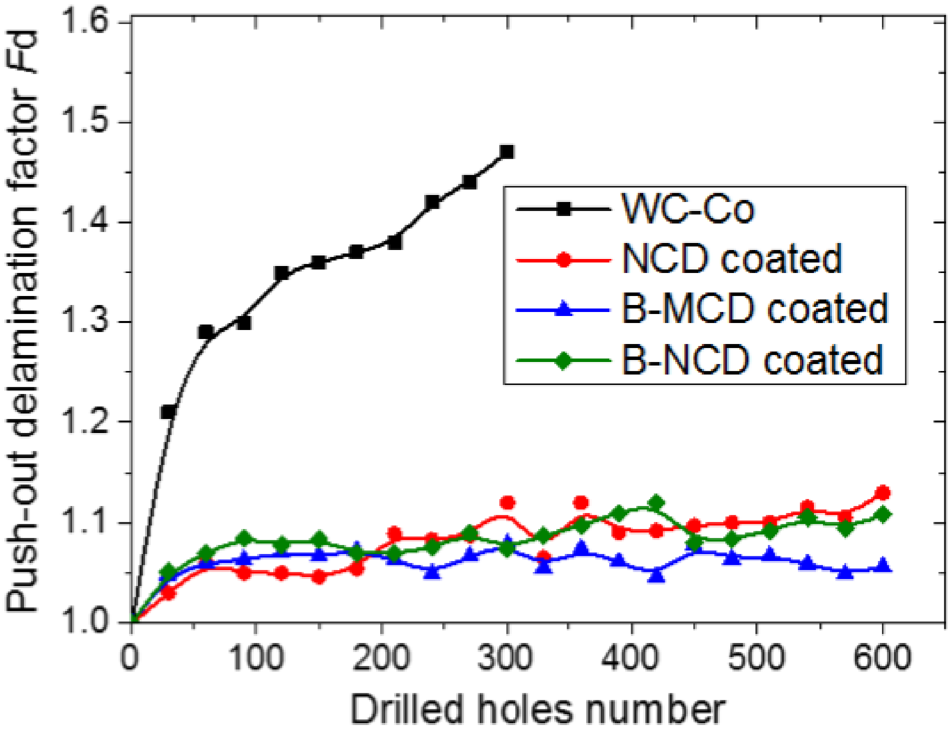

Figure 2.24. Variations of the delamination factor on exit hole side as a function of drilled hole number

These figures show an approximately similar trend for peel-up and push-out delamination with different values of the delamination factors. Also, as shown in Figures 2.23 and 2.24, the peel-up and the push-out delamination have high sensitivity to the drills' flank wear progress. This relationship can be explained as follows. The tool wear progress provided increasing loading through the growth of thrust force and torque during drilling. Subsequently, when the loading exceeds the interlaminar fracture toughness of the laminates, then delamination occurs. Moreover, the peel-up delamination trend has correlated to the torque values of the tested drills. In contrast, the push-out delamination close related to the thrust forces induced by the tested drills.

Besides peel-up and push-out delamination, push-out burr appearance on drilled hole exit is unacceptable defects of CFRP laminates. Used method for determination of *F*d does not evaluate the value of the push-out burrs. Therefore, in this study, the push-out burrs were assessed through the digital microscope observation only. Figure 2.25 shows the images of the hole exits drilled by the compared drills. Many uncut push-out burrs were induced after drilling by the WC-Co drill, as shown in Figure 2.25(a). Because, during drilling, wear of cutting edges has occurred, and carbon fibers could not be cut off. Furthermore, severe push-out delamination with the melting of resin bond was observed on the CFRP laminate's hole exit side. Such a phenomenon suggested that worn cutting edges of the WC-Co drill generated cutting temperature, exceeding the resin bond's glass transition temperature [41]. However, for the holes that produced the diamond-coated drills, shown in Figure 2.25(b) to (d), only some uncut burrs were observed. The least burrs, shown in Figure 2.25(c), are observed on the hole exit produced by the B-MCD drill. Such difference in hole quality could be attributed to the drill's lower flank wear value compared with the NCD and B-NCD coated drills.

Regarding the hole's size comparison, drilled hole sizes were measured with a gauge plug of a nominal diameter of 3.28 mm. The gauge passes through all holes drilled by diamond-coated drills. In the case of the WC-Co drill, the gauge did not go through since the 27th hole. As lower flank wear values of the diamond-coated drill's cutting edges keep the drilled holes into the tolerance zone of the required size, results can be explained compared with WC-Co drill's edges. Therefore, holes made by the WC-Co drill leave the tolerance zone soon due to the tool wear.

Based on the above evaluations, it is suggested that holes produced by the B-MCD coated drill have the best quality in terms of the delamination and push-out burrs appearance.

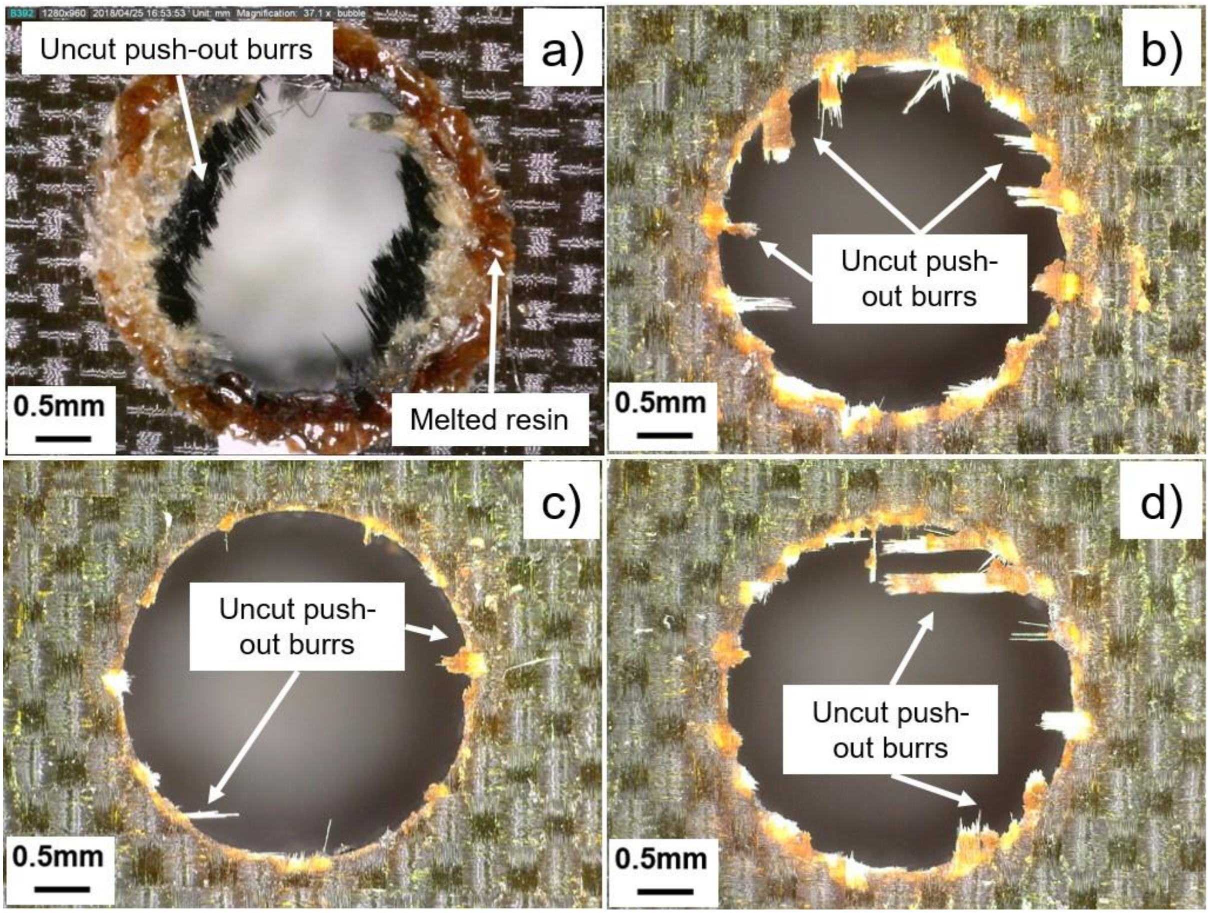
B392 1280x960 2018/04/25 16:53:53 Unit: mm Magnification: 37.1 x bubble
Uncut push-out burrs
a)
Melted resin
0.5mm
b)
Uncut push-out burrs
0.5mm
c)
Uncut push-out burrs
0.5mm
d)
Uncut push-out burrs
0.5mm

Figure 2.25. Images of CFRP hole exit: (a) 300th hole made by WC-Co drill and 600th holes made by NCD (b), B-MCD (c), B-NCD (d) coated drills, respectively

2.5. Conclusions

In this study, the effects of boron-doped and undoped diamond coatings on the cutting performance of WC-Co drills in drilling CFRP laminates have been experimentally investigated. Main conclusions obtained as follows:

(1) Experimental results indicate that appropriate level of boron doping into the diamond coating enhances adhesion strength between the coating and WC-Co substrate of the drill.

(2) Drilling test results show the advantage of the B-MCD coated drill in terms of the flank wear, the thrust force, and torque compared with the NCD and B-NCD coated drills.

(3) The delamination factor (Fd) correlates with the thrust force and the torque induced by the compared drills. All diamond-coated drills generate stable peel-up and push-out delamination factors. On the other hand, delamination factors produced by the WC-Co drill are rapidly increased. It confirms the benefit of the application of diamond coating for tools when drilling CFRP laminates. Moreover, B-MCD coated drill had generated the least push-out burrs between the tested drills.

Chapter 3. Reconditioning of diamond coated tools

3.1 Introduction

It is well-known that the utilization of special shape-designed WC-Co tools with CVD diamond coatings benefits CFRP machining, as resulting in less burr formation and delamination effects [41, 66, 102]. Further, tool wear resistance can be improved by doping CVD diamonds with minute amounts of boron. For instance, the resulting boron-doped microcrystalline diamond (B-MCD) film has shown excellent results in CFRP machining as described in the previous Chapter 2. On the other hand, such diamond-coated WC-Co tools with complicated shapes have a higher cost than conventional tools. Therefore, any effective tool life extension method of such tools is of great interest as before.

Cutting tool reconditioning is one of the most efficient cost-saving strategies in the manufacturing industry and corresponds green manufacturing requirements. For instance, Astakhov [103] reported that drills could be reconditioned and reused up to 10 times, thus significantly reducing costs and tool material wasting. Furthermore, gear cutting sector benefits from the reconditioning extensively, owing to the high cost of the WC-Co and high speed steel (HSS) based gear cutters [104]. Also, Sandvik Coromant concluded that a PVD coated solid carbide drills may be reconditioned three times with tool cost savings around 50% [105].

Conventionally, reconditioning approach for coated WC-Co based tools includes sequential procedures, such as decoating, tool regrinding, and film re-deposition [54]. Electrochemical etching (ECE) is commonly used for the decoating of metal-based and ceramic films, such as TiN, TiAlN, AlCrN, CrN, etc. [106-108]. On the other hand, the ECE method has some known issues such as preferential removal of Co from the WC-Co, so-called cobalt leaching, HSS corrosion, chemical waste disposal, handling hazards, etc. Another disadvantage inherent to the ECE consists in inability to etch chemically inert C-based coatings, such as diamond-like carbon (DLC) and CVD diamond.

Unrelated to the cutting tools reconditioning, diamond reactive ion etching (RIE) has been studied in different types of plasma apparatuses and with various reactive gases, such as oxygen, hydrogen, fluorine and chlorine compounds, and their combinations [109-113]. In the case of oxygen working gas, underlying erosion mechanism of the C-based materials is diversified, because the surface is concurrently exposed to fluxes of energetic O^+ and O_2^+ ions, neutral and excited O_2 and O_3 molecules, and O radicals. All these species may play significant role in the C atoms release. Firstly, energetic oxygen ions bombarding the carbon surface will transfer their momentum to the lattice and cause collision cascades in the surface layers and physical sputtering if the kinetic energy is sufficient. Secondly, reactive sputtering takes place when impinging oxygen ions react with C atoms in the end of their trajectory in the solid target and produce weakly bound molecules which are consequently desorbed into the gas phase. Thirdly, neutral molecular and atomic oxygen can oxidize the carbon surface and desorb as CO and/or CO_2 at elevated temperature. Atomic oxygen is highly reactive towards carbon and has lower reaction activation energy than molecular oxygen and is a very potent carbon eroding component of oxygen plasma, as reported by Cuesta et al. [112]. Carbon release induced by the reaction with neutral molecular and atomic oxygen can be addressed as purely chemical erosion. Therefore, in the presence of energetic ions and neutral oxygen in an ionizing environment one can expect three active carbon erosion mechanisms: physical sputtering, chemical sputtering and chemical erosion. Correlation between intensities of these erosion mechanisms is governed by the energy of impinging ions, ion flux, fluxes of reactive molecular and atomic species, carbon target temperature, etc.

However, from the tool reconditioning point of view, a several studies should be highlighted only. The ashing of CVD diamond films by oxygen plasma has been studied by Yunata et al. [114, 115]. In this approach, plasma extracted oxygen ions bombard the film surface which results in a combustion of the film at an elevated substrate temperature and low pressure. Also, using of a hollow cathode provided high plasma density and film erosion rates. On the other hand, utilization of the hollow cathode places some limitations on the batch uniformity and scalability, due to the localized plasma hot spot. Moreover, increased plasma density results in increased substrate temperature that might result in deterioration of the substrate materials. Another downside of the oxygen ashing method is its inefficiency in the case of metal-based ceramic films. CVD diamond coating removing via 2.45 GHz microwave plasma has been proposed by Liu et al. [116]. In that example, the tools were heated to rather high temperatures of 1073 K and exposed to a rather high density plasma. In all mentioned above approaches, the bulk plasma discharges were utilized, which normally leads to a plasma sheath formation around biased workpiece, in accordance with the Child-Langmuir law and electrostatic focusing of the ion fluxes on cutting edges and peculiarities. Although the aforementioned studies have been focused on rather large and simple shaped tools, where the effect of the plasma sheath might not be decisive, one may expect these methods to be challenging in the case of miniature and/or complex shape tools, where characteristic tool dimension and fine features become comparable to the plasma sheath width. For instance, Remnev et al. [117] has been studied a bulk plasma based etching process in application to simple twist drills decoating and found significant non-uniformity of etching in the concave areas of the tools. In that study, utilization of ~10^{10} cm^{-3} Ar plasma and negative bias of -800

V for 1 mm of diameter drill decoating resulted in a steady-state layer of film residue, caused by self-shadowing and re-deposition effects. Indeed, the film residue is detrimental for the consequent tool reconditioning steps.

A practically important method of CVD diamond decoating has been developed by Remnev [118]. The method consists in the reactively enhanced ion beam etching (RIBE) of a CVD diamond film with multiple closed electron drift ion sources (CDIS). The method has been shown to be able to strip both CVD diamonds and metal-based composite films from cutting tools with a complex geometry. Detail description of decoating by RIBE method and applied setup is provided in following section 3.2. On the other hand, the cutting performance of RIBE-reconditioned tools has not been studied. Indeed, energetic particle bombardment may alter the surface properties and the micro-geometry of the tools, negatively affecting the cutting performance of the reconditioned tools.

Besides the plasma based processes other alternative decoating approaches are reported as well. One example of an alternative decoating process is an ultra-short pulsed laser ablation of diamond films, reported by Shirk et al. [119]. In the reported case, the femtosecond-pulsed laser ablation of the film was exploited, providing a high erosion rate along with possible substrate damage, when the irradiation regime is suboptimal. One can expect that due to different absorption coefficients of various hard coatings, the process is rather sensitive to the coating composition, structure, surface finish and other conditions that may vary from case to case. Therefore, this method did not find wide-spread use in the cutting tool reconditioning field so far.

Based on reported data overview, it is possible to conclude that commercially available reconditioning approach related to diamond-coated tools is absent. Therefore, development of such efficient reconditioning method would be attractive for industrial use.

In order to reuse the cutting tools after the decoating, the CVD diamond film must be re-applied, so the tools recover its mechanical properties. As previously described in Chapter 2, several extra steps are required prior to the film deposition: cleaning, Co wet-chemical etching (WCE) from the surface, and seeding. The WCE is the most aggressive among these surface preparation steps and may negatively impact the WC-Co tool integrity. Therefore, the combined effects of RIBE decoating and WCE on various important tool properties have been investigated in the present work. The surface morphology, cutting edge geometry, B-MCD film adhesion and structure, and finally cutting performance were evaluated and discussed from the standpoint of the reconditioning approach.

3.2 General features of RIBE process

3.2.1 Ion beam definitions

Ion beam (IB) is a directional flow of single or multi charged ions moving with velocities that are much higher than their thermal random velocity. IBs are conventionally used for sputter deposition, ion implantation, sputter etching, semiconductor patterning, etc.

There are focused and unfocused ion beams. Focused ion beam (FIB) has rather small beam spot and is usually scanned in the same manner as electron beam in the SEM. FIBs are widely used in thin film analysis, samples slicing for transmission electron microscopy, micro- and nano-machining, etc.

Unfocused (broad) ion beams have rather large beam cross-section and are not usually scanned. Broad IBs can irradiate large areas and are used for sputter deposition, patterning, surface cleaning prior to deposition, etc. In this study the broad IB is used.

A most important parameter of the ion beam is kinetic energy (Ek) of the ions. Depending on the ion source type, IBs can be mono-energetic or can have a rather wide range of ion energies in the beam.

Another important parameter of a broad IB is an ion current density distribution across the beam cross-section. Many industrial grade ion sources have rather inhomogeneous distribution so scanning or rotation of the target can be used in order to improve the ion fluence homogeneity across the targets surface.

3.2.2 Closed Drift Ion Source “RADICAL”

The “RADICAL” closed electron drift ion source (CDIS), is one of many variants of closed drift ion sources and is categorized as anode layer CDIS. The CDISs were originally developed in the USSR as an electric thruster for space propulsion in the early 1960s [120, 121]. Eventually simplified design, i.e. accelerator with anode layer “RADICAL”, was implemented for industrial application in the micro-electronics, surface cleaning and activation in thin films field, sputter deposition, etc. It features large aperture and relatively high ion current. Due to the grid-less design, the CDIS provides self-neutralization of the ion space charge and doesn't require hot filament neutralizer commonly utilized in the gridded types of the ion sources, such as Kauffman type. Owing to the absence of the hot filament, any gas can be utilized as the working gas, including aggressive gases such oxygen, sulfur hexafluoride (SF_6), carbon tetrafluoride (CF_4), etc.

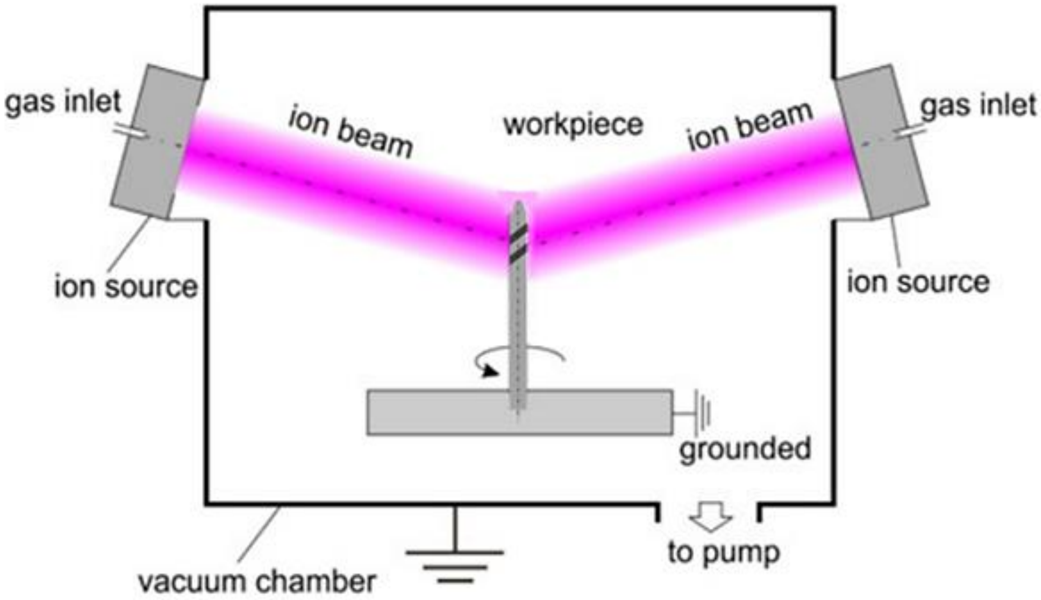

Figure 3.1. RIBE experimental setup [118]

For the tool decoating experiments of this study, a setup equipped with multiple CDISs of “RADICAL” type was used. The CDISs were oriented concentrically in the way that the ion beams converged in the working area, where the tools are situated, as represented in Figure 3.1. In our experiments, the CDIS axes were inclined at average 14° relatively to the horizontal plane, in order to create the required working zone, where ion beam irradiation is taking place. Vertical position of the treated tool tips should lie in the beams intersection plane for the best etching efficiency.

Operating principle of the CDISs, as can be understood from its name, consists in confining the electrons in a certain volume by forcing them to move in closed trajectories. The electrons are trapped in the circular region by crossed magnetic and electric fields, while an ions are not strongly magnetized and can freely be accelerated by the electrical field. On the other words, the electrons, whose mobility across the magnetic field is very limited, slowly move towards the anode. The ions enter the annular gap between poles of the magnetic system from the anode and accelerate without being affected by the magnetic field. The poles of the magnetic system are conductors and have the cathode potential. Resulting ion beam has a tubular shape and is fully neutralized which provides good transportability to a distant objects in the working chamber.

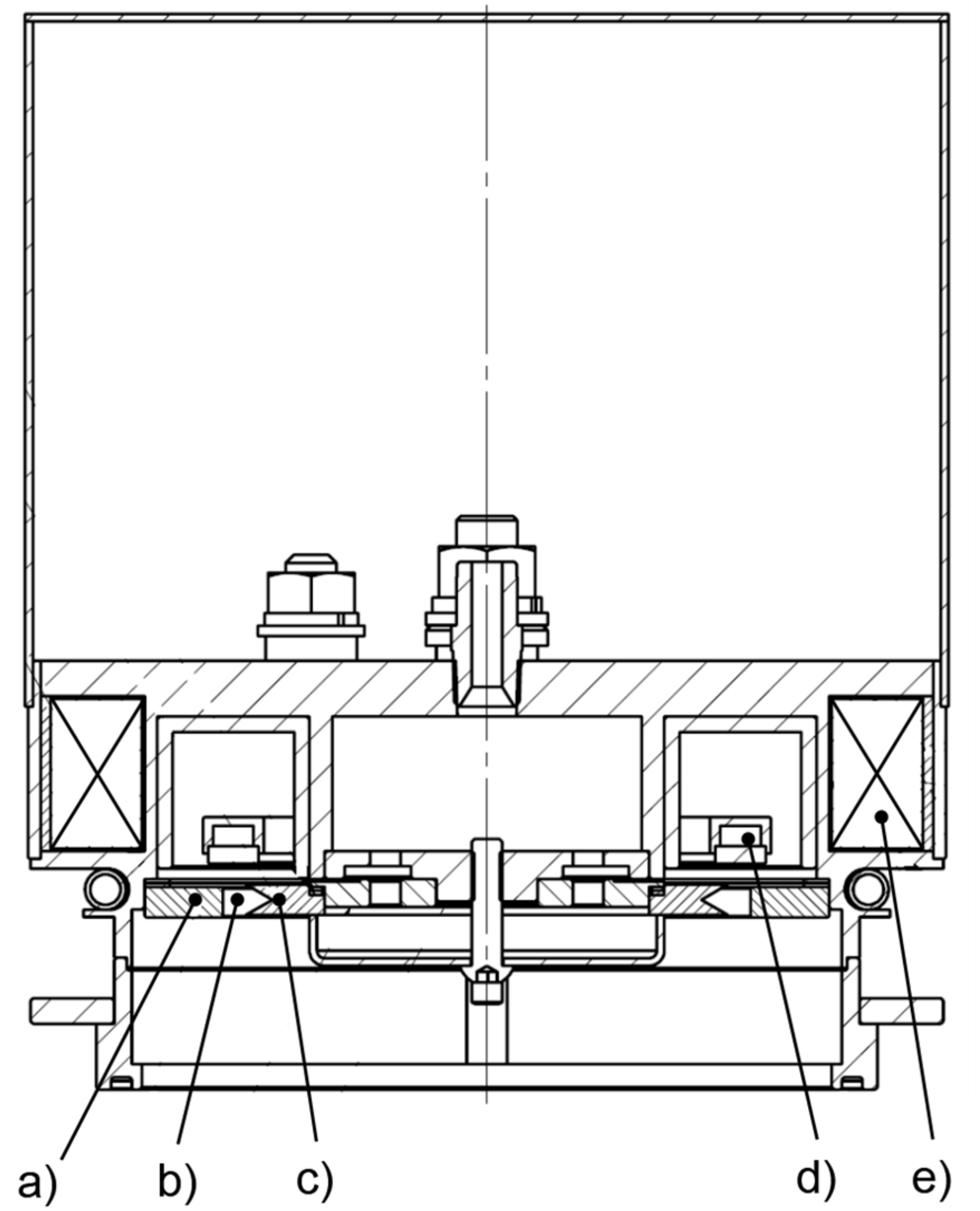

Figure 3.2. Structure of “RADICAL” type based CDIS: (a) external cathode ring; (b) acceleration channel; (c) internal cathode ring; (d) anode; (e) magnetic coil

Structure of the CDIS applied in the current study illustrated in Figure 3.2. Here external (a), internal (c) cathode rings and magnetic coil (e), as shown in Figure 3.2, consist the magnetic system. The CDIS accelerating channel (b) is the annular gap between the cathode rings of the magnetic system, limited on one side by the anode (d).

Regardless the simplicity of the design of the anode layer CDIS, operation principle is rather complex and been studied in a number of works. Comprehensive description of CDIS variants and theoretical analysis of their operation features are given in [121].

3.2.3 “RADICAL” CDIS operation parameters

Fully neutralized ion beam constitutes so called IB plasma, since quasi-neutrality condition is met within the IB transport region. The IB plasma has a strong anisotropy of the ion momentum in the direction of the IB propagation. The e-cloud serves as a space-charge compensator and prevents the IB from coulomb repulsion. The electron energy is usually very low compared to the ion energy and averages about few electron-volts. The wide-area IB can be characterized by the ion current density, average ion kinetic energy, ion energy spectrum and IB divergence. For optimization of the RIBE process the ion current density and *E*k must be maximized. To control these properties of the IB various operating parameters can be used. The parameters operating ranges and their qualitatively judged influence on the RIBE are listed in the Table 3.1.

Table 3.1. “RADICAL” CDIS operating parameters:

Parameter	Value range	Influence on IB
Working pressure [Pa]	0.01 - 1	Increases electron impact ionization and discharge current. Hampers ions transportation to the target due to ion recoils.
Flow rate of working gas [sccm]	0 - 70	At constant working pressure in the chamber increases the discharge current.
Voltage applied to the magnetic coil [V]	10 - 30	Decreases cyclotron radius of electrons in the ionization region, increases discharge current due to better electron entrapment.
Discharge voltage [kV]	0.1 - 4	Increases ionization and ion beam acceleration, resulting in higher discharge current and higher kinetic energy of the ions.
Discharge current [mA]	0 - 500	Dependant parameter. Increases ion current density and population of active species if reactive gas is used.

From the application stand point the "RADICAL" CDIS is a very simple, inexpensive and robust. It generally it has no consumable parts, such as filaments in the Kaufmann ISs, and doesn't require routine maintenance, other than cleaning of the deposits on the anode. Periodical cleaning of the anode allows for operating at the near maximum power, on the other hand, when left untouched, the CDIS will exhibit small arcs formation, due to overheating of the delaminated from the anode film fragments. When operating at moderate discharge currents ~ 100mA, the needs for the maintenance is almost nil and micro-arcing is unusual.

Features of the "RADICAL" CDIS are:

- Relatively high pressure operation, up to 0.3 Pa.
- Self-neutralized ion beam (no neutralizer required).
- Possibility of operation with any working gas, including aggressive gases.
- High discharge current of up to 140 mA in the high voltage mode.
- Large irradiation zone of ~ 400 mm.
- Tubular beam (rotation and scanning of specimens are required for uniform erosion).
- No consumption parts.
- Simple design and low cost.
- Compactness. Possibility to install a number of CDISs.

3.2.4 Application for diamond films etching

Significant difference between purely physical etching with Ar and chemically enhanced etching with O_2 was found for all types of diamond and graphite, which indicates that the RIBE process is governed by the chemical reactions on the surface or in the subplantation layer [118]. This is coherent with the study by Hopf et al. [122] suggesting a model of concurrent sputtering and oxidation of carbon films, where physical bombardment and chemical reactions on the surface play synergistic roles, resulting in high rates of carbon etching. Moreover, molecular oxygen activation is thought to be very intensive due to the relatively high working pressure and large number of trapped electrons in the anode layer of the CDISs. Trapped electrons are drifting azimuthally in the acceleration region and causing molecular excitation and further dissociation of the O_2 molecules with rather low electron kinetic energy threshold of less than 10 eV [120].

In my understanding, the RIBE consists of following steps:

- Ion-induced amorphization of the outermost layers of diamond film with production of surface defects and dangling bonds.
- Reaction between activated carbon and atomic or molecular oxygen.

- Volatilization of reaction products in form of CO and CO_2.

Besides, direct chemical sputtering can play significant role. Since workpiece temperature in our setup was far below 700 K, erosion due to thermal molecular oxygen (combustion) was not realized. Moreover, formation of brittle η-phase and associated reduction of the toughness of the WC-Co material is unlikely at this temperature [123].

Minimal damage inflicted to the substrate material is promising from the standpoint of further tool reconditioning cycles. Indeed, preliminary experiments indicate that commercial diamond coated tools have some film thickness difference measured on outers and flutes tool surfaces. Therefore, it is possible to conclude that tool hardmetal substrate will sputter under ion beam irradiation in order to obtain entire diamond film removal.

Figure 3.3 illustrated etching rates comparison of Ar based physical sputtering, and O_2 based RIBE process, respectively. Due to the fact that W and Co do not form volatile compounds under the RIBE conditions, the WC-Co etching rate was 10 times lower than diamond, confirming excellent selectivity of the method. Moreover, sixfold difference in the RIBE rate compared with Ar etching ones, suggests sputtering inhibition in the presence of oxygen, due to the surface metal oxides formation. This effect was previously studied by Remnev et al. [124, 125] in the context of stainless steel sputtering inhibition by controlled introduction of molecular oxygen during low energy Ar+ bombardment.

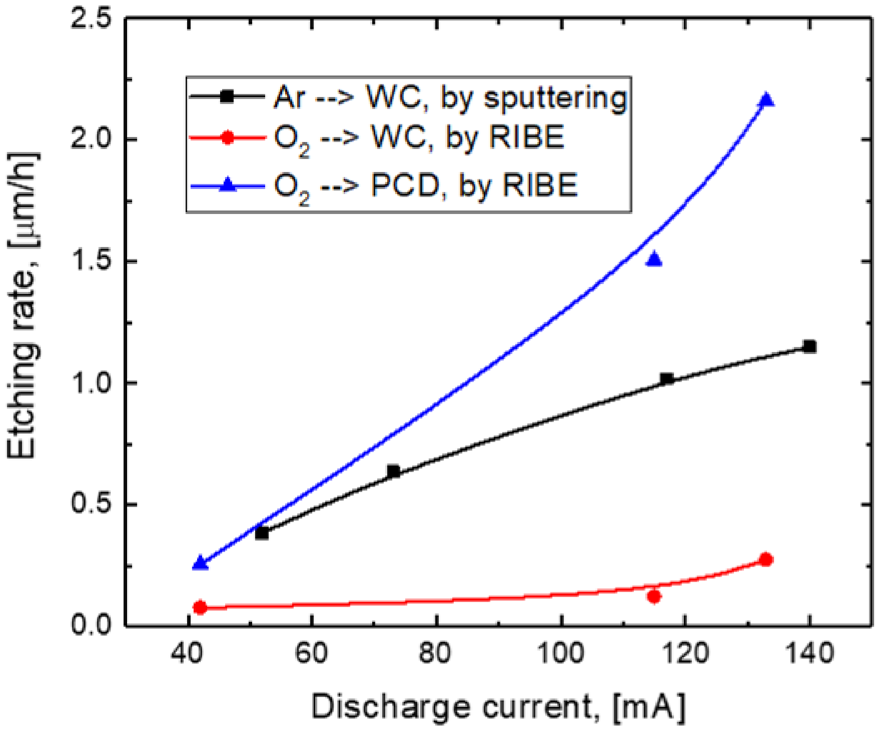

Figure 3.3. Etching rate as a function of CDIS discharge current

Furthermore, minor difference between etching rates at lower discharge current may be neglected. Because, from an industrial point of view, reaching of maximal etching rate looks economically attractive.

3.3 Materials and methods

3.3.1 Experimental procedures

In this study, as shown in Figure 3.4, the substrate pretreatment (WCE), B-MCD deposition (CVD), CFRP cutting (CT), and film decoating (RIBE) were conducted repeatedly on one-shot cemented carbide drills in order to emulate the practically viable tool life cycle (TLC). The tool substrate and the film properties were investigated at each step using a combination of surface characterization techniques such as scanning electron microscopy (SEM), confocal scanning laser microscopy (CSLM), and Raman spectroscopy. Moreover, the cutting performance was evaluated during the CT through flank wear and CFRP hole quality assessment. The evaluation was performed for three consecutive TLCs, including the TLC0 (WCE0, CVD0, and CT0) - a newly deposited tool, the TLC1 (RIBE1, WCE1, CVD1, and CT1) - a first-time reconditioned tool, and the TLC2 (RIBE2, WCE2, CVD2, and CT2) - a second-time reconditioned tool.

The CT0, CT1, and CT2 machining were interrupted prior to the major tool damage occurrence in order to limit the wear to the B-MCD film and not the WC-Co substrate. Due to this tool-saving approach, no tool regrinding was necessary.

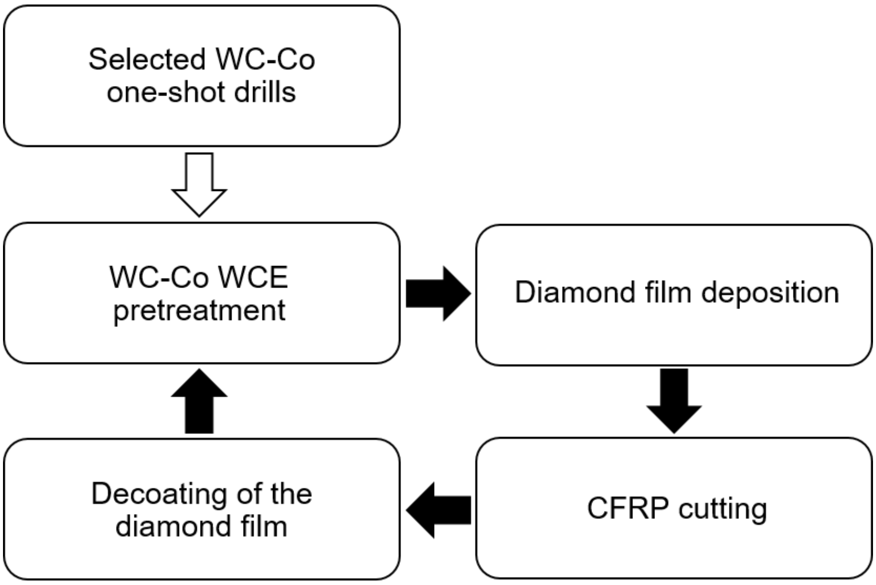

Figure 3.4. Tool life with multiple reconditioning cycles

3.3.2 Cutting tools

One-shot WC-Co drills with a specific geometry optimized for CFRP materials were selected for the experiment. The structure of the drill is presented in Figure 3.5. The drill with a nominal diameter of 6.36 mm had two straight flutes with a tip point angle of 120° and two curve-shaped edges, namely, primary and secondary cutting edges, joined by a rounded corner. A straight tertiary cutting edge (Figure 3.5b) formed a reamer part of the tool, aimed at the smoothing of the drill holes and providing the hole diameter close to the nominal. Such an innovative drill geometry was described in a corresponding patent [126]. Other drill dimensions were as follows: the total length was 88 mm, the cutting edge length was 40 mm, and the shank diameter was 9 mm. All drill substrates were made of K01 graded tungsten carbide with cobalt (WC-6 wt. % Co). This material is commonly used to manufacture complicated-cutting-shape tools and can be coated with CVD diamonds. The total of three drills were investigated with the reconditioning steps.

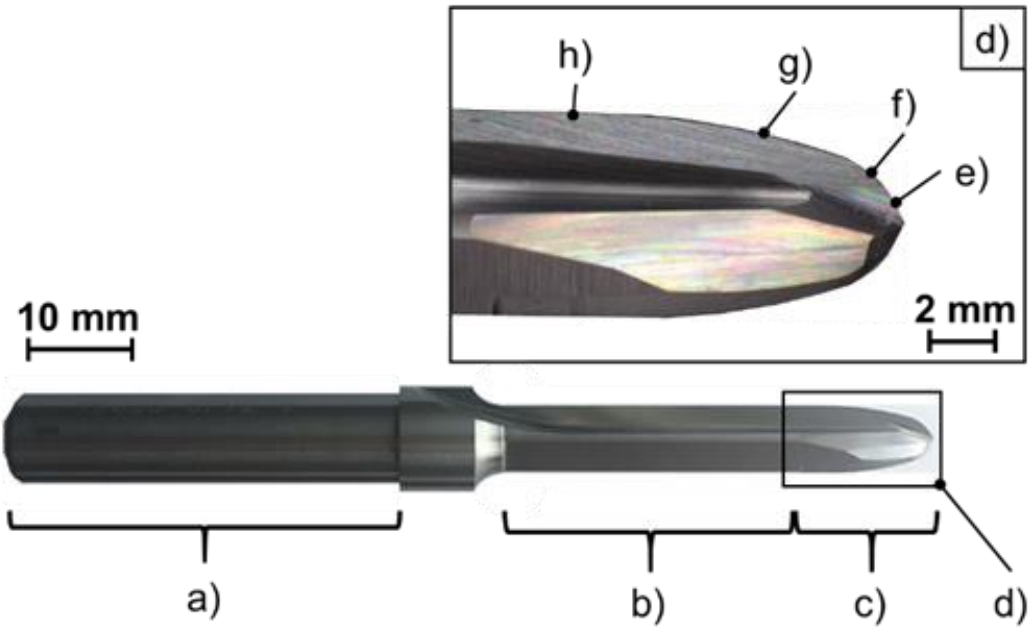

Figure 3.5. One-shot WC-Co drill utilized in the current study: (a) drill shank; (b) reamer cutting portion; (c) cutting edge portion; (d) magnified view of the drill cutting edge portion; (e) primary cutting edge; (f) rounded corner; (g) secondary cutting edge; (h) tertiary cutting edge

3.3.3 Substrate preparation and deposition of the diamond coating

This study utilized B-MCD coating, which has shown excellent performance in CFRP machining as reported in the Chapter 2.

Prior to the diamond film deposition, the drills were chemically pretreated. The conventionally used WCE method, described in the previous chapter, was adopted for the selected substrates and included treatment steps with the Murakami reagent and followed a nitric acid solution. The WCE based processes were all carried out in special designed semi-automatic setup, presented in Figure 3.6, by unmanned WCE cycle.

Before the WCE0 process, new one-shot drills were ultrasound cleaned in acetone and ethanol consecutively, with the aim to remove a grease contamination. Hereafter for the WCE1 and WCE2 processes, the film decoated drills had loaded to the setup without the ultrasound cleaning.

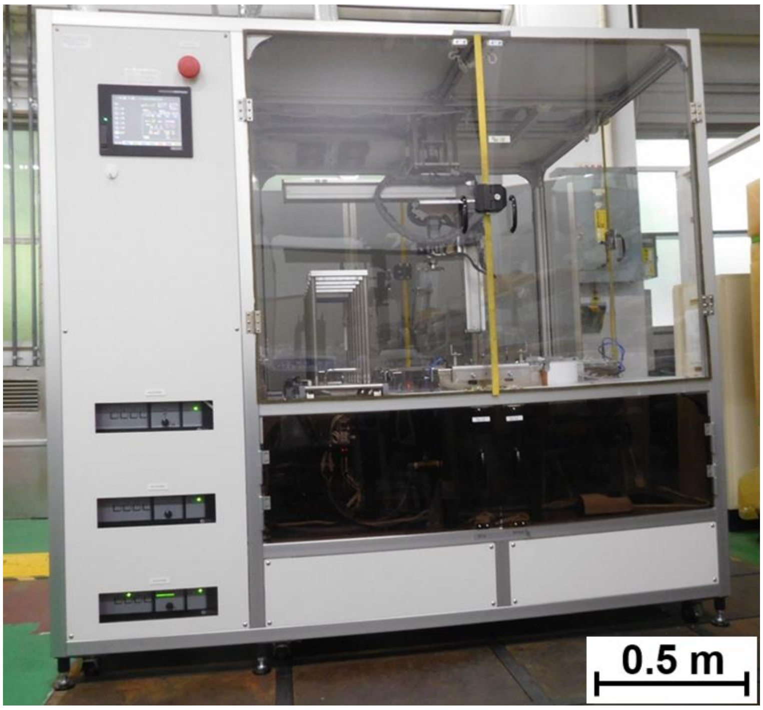

Figure 3.6. Original semi-automatic setup for chemical substrate pretreatment

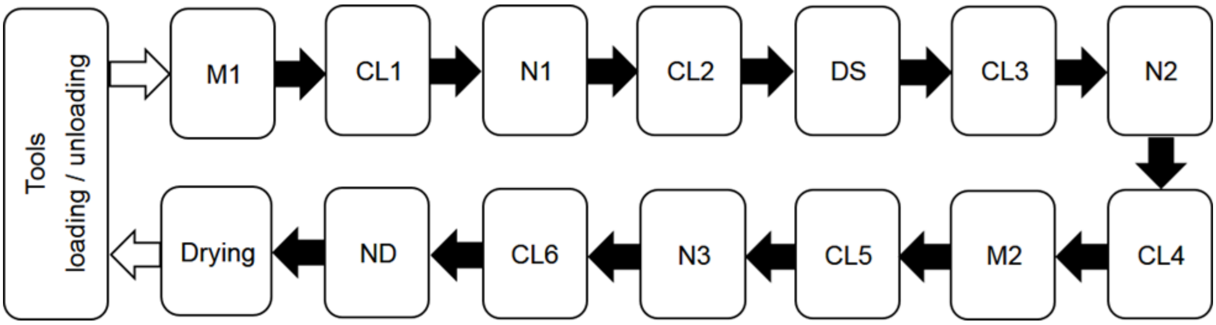

Figure 3.7. WCE cycle for chemical substrate pretreatment

The shown in Figure 3.7 WCE cycle consists next process steps, as Murakami reagent etchings (M1 and M2), nitric acid solution etchings (N1, N2 and N3), drill surface scratching (DS), seeding (ND) and cleaning steps (CL1 to CL6), included drills rinsing by purified water with following air blowing. All chemical etching steps were performed by immersing the tool substrates into an ultrasonic bath with the corresponding chemicals. It has been described previously that the effect of the Murakami reagent is to attack the WC grains present at the substrate surface, consequently roughing the surface and exposing the cobalt binder. Then next etching of the nitric acid solution oxidizes the cobalt binder to soluble Co^{2+} compounds, consequently washed out during the ultrasonication. DS step provides the tool surface scratching process in an ultrasonic bath containing a solution of 2 g diamond powder (2-8 μm of grain size) dispersed in 1000 ml of purified water, in order to produce a homogeneous surface free of any features which may have a detrimental effect on the diamond adhesion, as grinding marks, weakly bonded WC grains and etc. During the ND step, the treated tools were seeded ultrasonically by a purified water suspension with a nanodiamond having a 4 nm average particle size. Then a step named "Drying" includes the seeded tool substrates rinsing ultrasonically in acetone with following drying by air blowing. All mentioned above WCE process steps are summarized in Table 3.2.

A B-MCD film was deposited on the substrates using the HFCVD method in an industrial hot-filament reactor (ShinMaywa Industries), presented in Figure 3.8. A mixture of CH_4 and H_2 was utilized as a precursor gas in the deposition step and nucleation deposition process stages. The boron incorporation was carried out by evaporating a mixture of trimethoxyborane ($(CH_3O)_3B$) with acetone. The B/C atomic ratio is determined by pre-mixing the acetone and the trimethoxyborane according to a certain proportion. A controlled evaporation mixer was employed for the preparation of the gas-liquid mixture. Then all gases and the evaporated mixture were directly introduced into the chamber with driven flow rates.

During the deposition process, the filament temperature is approximately measured by the double-color integrated infrared thermometer (E1RH-F2-V, Fluke), and the substrate temperature is measured by Type K thermocouples installed in a worktable. Common deposition parameters and filament arrangement are shown in Table 3.3. Arrangement of the filaments and related drills are same, as illustrated in Figure 2.9 of the Chapter 2.

As a result, the B-MCD coating with a thickness of about 10 µm ± 1 µm was deposited on the tested drills. After each process stage, the deposited diamond film and chemically and/or ion-etched substrate surface were examined in terms of the surface morphology by a SEM (JSM5510, JEOL). In addition, the surface roughness evaluations for all process stages were conducted with a laser microscope (OLS4100, Olympus). In the assessment of the adhesion strength between the deposited coating and the WC-Co substrate, indentation tests were carried out (Rockwell hardness testing machine ARK-600, Mitutoyo).

Table 3.2. WCE process steps:

Notation	Description	Time
M1	Tool surface etching by immersion in Murakami reagent (1:1:10 $KOH+K_3[Fe(CN)_6]+H_2O$)	10 min
M2		30 sec
N1, N2, N3	Tool surface etching/ decobaltation by immersion in ultrasonic bath with nitric acid solution (10% HNO_3+90% H_2O)	1 min/step
DS	Tool surface wet scratching in ultrasonic bath with the diamond powder solution	10 min
ND	Seeding of treated tool surfaces by diamond growth centers in ultrasonic bath with a stable aqueous suspension of nanodiamond particles with average size of 4nm and concentration of 0.1-1 wt%	10 min
CL1 – CL6	Tool surface cleaning by rinsing in ultrasonic bath with purified water in order to remove chemicals remains and following air blowing	4 min/step
Drying	The seeded tool substrates rinsing ultrasonically in acetone with following drying by air blowing.	7 min

ShinMaywa
ShinMaywa
0.5 m

Figure 3.8. Industrial diamond coating system (ShinMaywa Industries) [127]

Table 3.3. Deposition process parameters:

Parameter	Boron-doped microcrystalline diamond (B-MCD)
Flow of H_2 [sccm]	700
Flow of CH_4 [sccm]	15
B/C atomic ratio [ppm]	8000
Process pressure [Pa]	600
Substrate temperature [K]	1073 ± 293
Duration [h]	33
Filament material	W
Filament length [mm]	280
Filament diameter [mm]	0.2
Filament height [mm]	7
Filament separation [mm]	24
Filament-substrate distance [mm]	10
Filament current [A/filament]	6
Filament temperature [K]	2273±323

3.3.4 Decoating by RIBE

Diamond-film RIBE decoating was performed with a commercial ion etching system (IE800, ShinMaywa Industries), presented in Figure 3.9. The diamond etching was achieved through oxygen ion beams generated with CDIS.

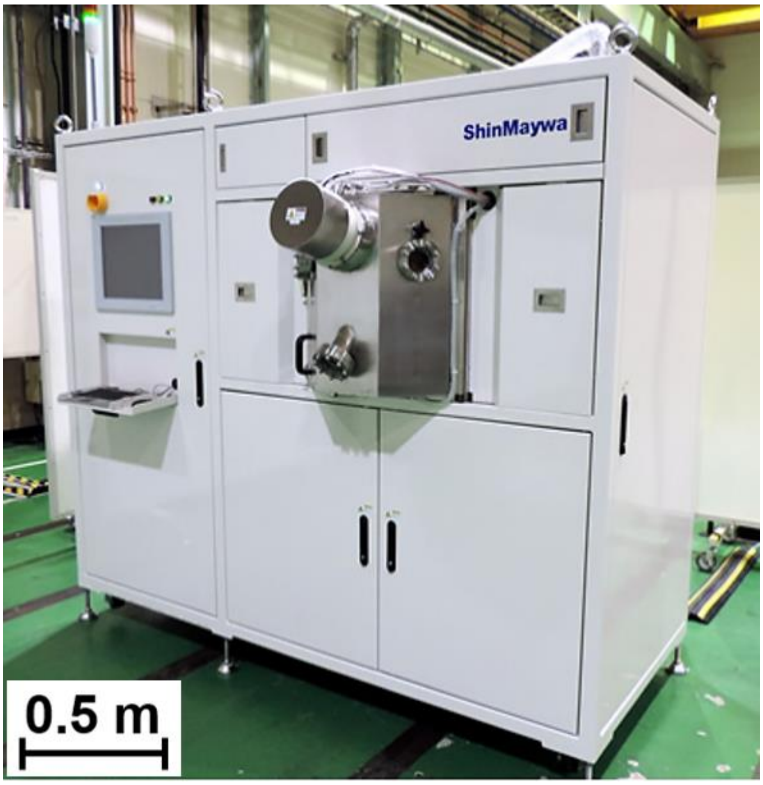

Figure 3.9. Industrial ion etching system IE800 (ShinMaywa Industries) [127]

The tools for decoating were placed in a vacuum chamber and exposed to a CDIS concentric array. The beam size of CDIS was ~100 mm in diameter and covered the whole coated length of the processed tools, so that the whole coating was etched with a good uniformity along the vertical axis. In addition, as illustrated in Figure 3.10, the tools were rotated planetary in order to provide an even ion/radical flux exposure in the horizontal plane, which was previously shown to result in a good etching uniformity inside the flutes [117].

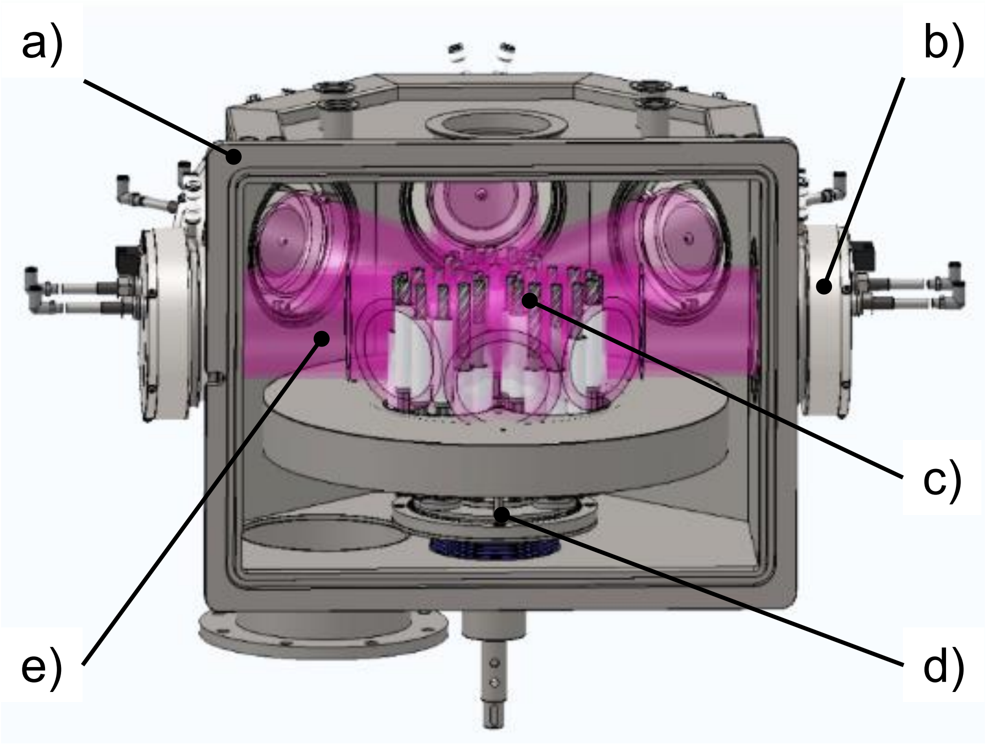

Figure 3.10. RIBE experimental setup for tool de-coating: (a) vacuum chamber; (b) CDIS; (c) processed cutting tools; (d) planetary rotation system; (e) simulated ion beam, pink colored

Pure oxygen was used as a beam-forming gas. The accelerating voltage was set to 4.0 kV, which generated a discharge current of ~100 mA at a 0.3 Pa pressure and the O_2 flow 60 sccm.

The RIBE rate was evaluated in a preliminary experiments and consists about 1.7 µm/h for the microcrystalline diamond film. Wherever the ion beam contacts with the uncoated tool parts, the WC-Co sputtering also took place but with a much slower rate due to the primarily chemical nature of the process, as described in the Section 3.2.4.

The applied tools were etched for 6 h in the same batch. The temperature during the etching did not exceed 573 K.

3.3.5 Cutting tests

In this study, the cutting performances of new and reconditioned drills were evaluated by drilling a series of consecutive holes in a workpiece. Automatically laid up CFRP laminates with a thickness of 14 mm and dimensions of 250 mm × 100 mm were used as the workpiece. Each workpiece consisted of 72 unidirectional layers of prepreg P2352W-19 (T800SC/3900 series, TORAY) in (0/90/45/0/-45/90/45/0/-45/90/45/0/-45/90/45/0/-45/90/45/0/-45/90/45/0/-45/90/45/0/-45/90/45/ 0/-45/90/ 45/ 0/-45/90/02)s lay-up. The carbon fiber volume ratio was about 60%. A technical data of the applied carbon fibers and laminates are described previously in the Section 2.3.3.

A vertical milling center OKUMA MD-45VA was utilized to perform the drilling tests. The workpiece was fixed using a tailored fixture mounted on a 3-component force dynamometer "Kistler 9257B", as shown in Figure 3.11. During experiments, thrust force signals were processed using a multichannel charge amplifier "Kistler 5019A" and monitored on a personal computer using data acquisition software DynoWare 3.2. The cutting parameters were as follows: the drill rotation n = 2700 rpm, the cutting speed V = 53.9 m/min, and the feed rate f = 0.1 mm/rev, which were kept constant. These cutting parameters utilize for machining CFRP commercial products by the same drills. No coolant was applied during the tests. The number of drilled holes was limited to below 200 in order to avoid the drill substrate wear and the necessity of tool regrinding. A drill flank wear was measured after each 20 holes using a digital microscope (VHX-1000SP, Keyence). After drilling 200 holes, the drills were checked for the damage to cutting edges, such as cutting edge chipping or a fracture via SEM.

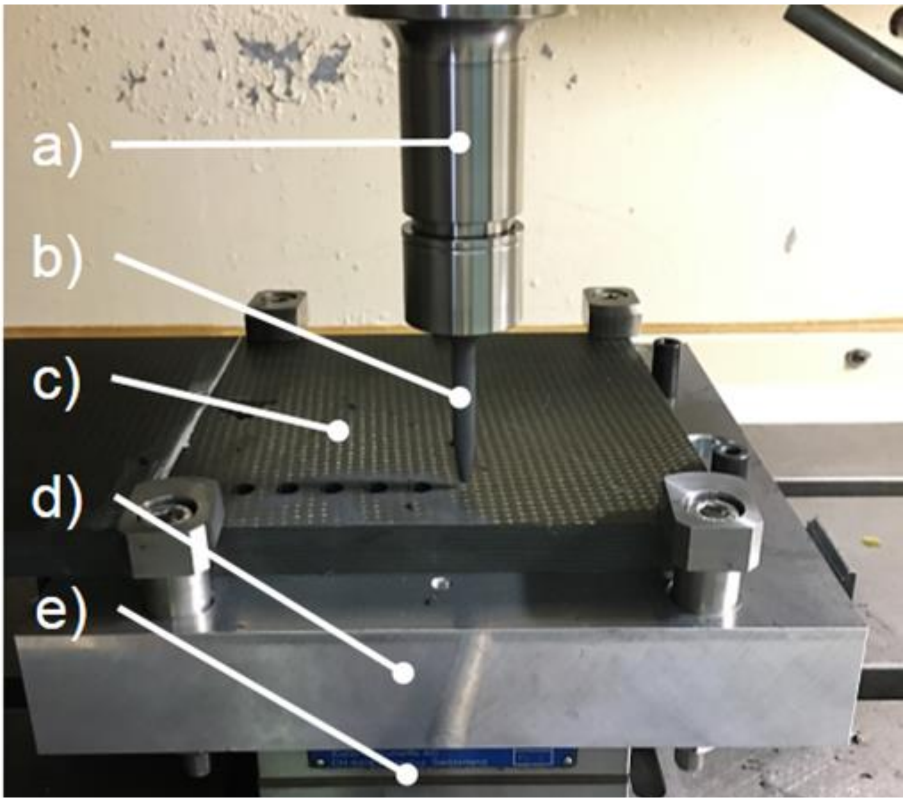

Figure 3.11. Experimental setup for cutting tests: (a) machine; (b) tested drill; (c) CFRP workpiece; (d) fixture; (e) dynamometer

3.4 Experimental results and discussion

3.4.1 Tool surface evaluation

Figure 3.12 displays the substrate surface morphologies obtained by SEM for different stages of the experiment, while Figure 3.13 shows the resulting surface roughness data of the stages. Surface texture parameter *S*a, as an arithmetical mean height, based on ISO 25178 - “Surface Texture”, was recorded and averaged from multi-point measurements on the flank surfaces of the drills. The scan size was determined by the optical magnification of the system (100×) in a resulting surface area of 129 µm × 129 µm with a profile Gaussian filter λc of 8 µm.

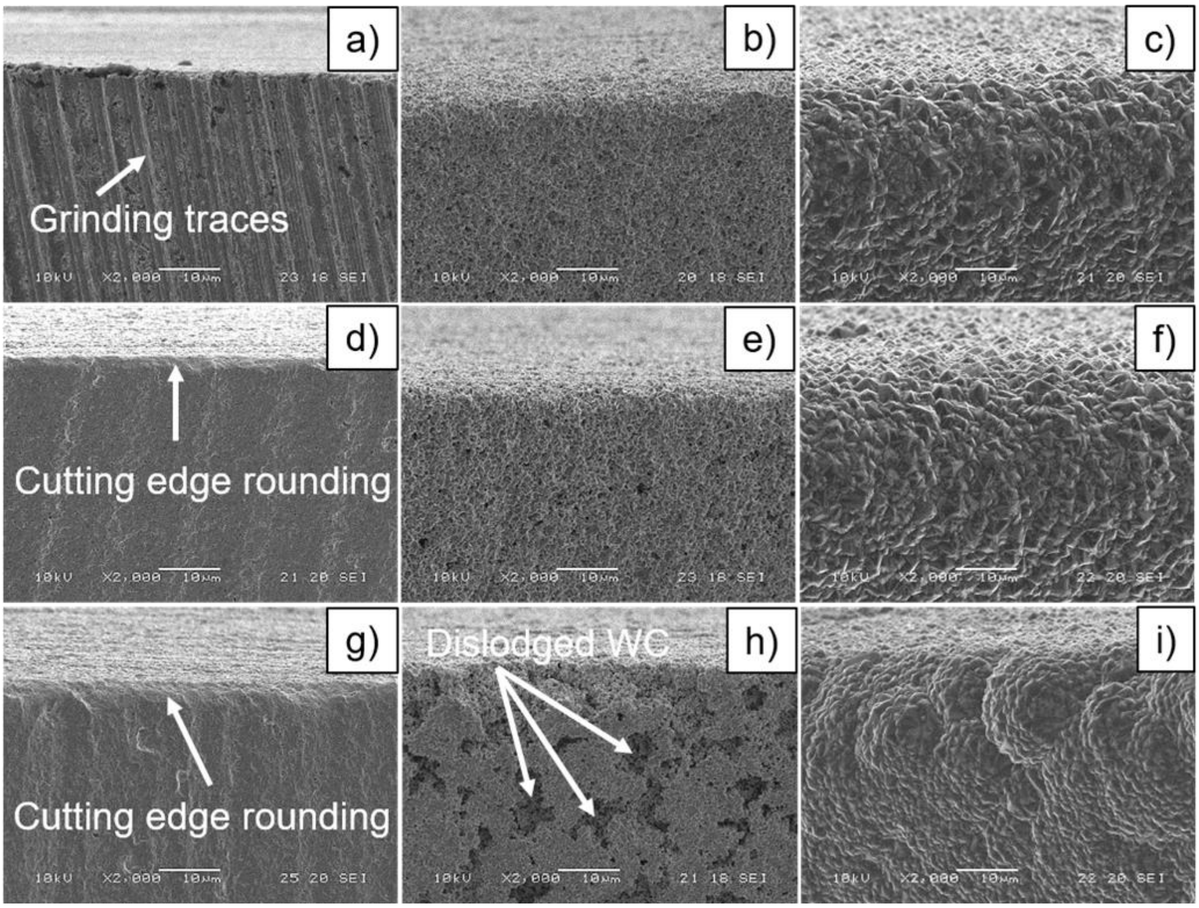
a)
Grinding traces
10kU X2,000 10μm 23 18 SEI
b)
10kU X2,000 10μm 20 18 SEI
c)
10kU X2,000 10μm 21 20 SEI
d)
Cutting edge rounding
10kU X2,000 10μm 21 20 SEI
e)
10kU X2,000 10μm 23 18 SEI
f)
10kU X2,000 10μm 22 20 SEI
g)
Cutting edge rounding
10kU X2,000 10μm 25 20 SEI
h)
Dislodged WC
10kU X2,000 10μm 21 18 SEI
i)
10kU X2,000 10μm 22 20 SEI

Figure 3.12. Morphologies of the drill flank surface, observed at 6 mm from the drill tip: (a) original, as grinded; (b) wet-chemical etching 0 (WCE0) of the new drill (TLC0); (c) chemical vapor deposition 0 (CVD0) of the TLC0; (d) reactive ion beam etching 1 (RIBE1) of the 1st-time reconditioned drill (TLC1); (e) WCE1 of the TLC1; (f) CVD1 of the TLC1; (g) RIBE2 of the 2nd-time reconditioned drill (TLC2); (h) WCE2 of the TLC2; (i) CVD2 of the TLC2

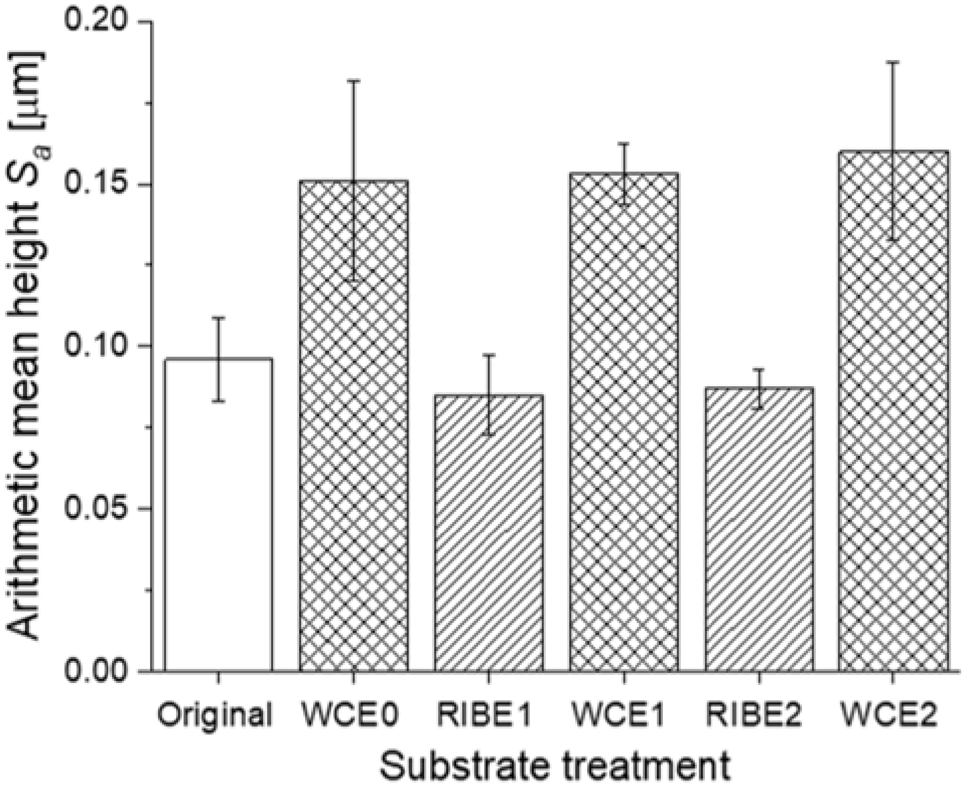

Figure 3.13. Substrate roughness characteristics by the arithmetical mean height (*S*a) of the surface texture

The original drill substrate, as shown in Figure 3.12(a), represented the as-ground surface depicting the directional marks left by the grinding process on the surface of the tool, which also provided a non-uniform texture in terms of the distribution of the WC grains and the Co binder due to the amount of surface damage after the grinding process [128]. These feed marks display an average surface texture roughness of *S*a = 0.096 µm.

The surface morphology after the WCE0 process, as shown in Figure 3.12(b), revealed a uniform surface with *S*a value of 0.151 µm and some directional surface features. The increase in the roughness after the process is attributed to the WCE, which attacked the WC grains and oxidized the cobalt binder to soluble Co compounds removed during the procedure under applied ultra-sonication [82]. Such a washing action may dislodge weakly bonded WC grains from the surface and create some porous surface textures. Further, Figure 3.12(e) shows a uniform surface with a roughness *S*a parameter of 0.153 µm, generated after the WCE1 process of the 1st reconditioning cycle. However, the surface, produced by the WCE2 process of the 2nd reconditioning cycle, had a rougher texture with *S*a of 0.160 µm and pitted areas, as shown in Figure 3.12(h). It is possible to propose that an accumulative effect of removing the binder phase in WCE stages led to the formation of randomly distributed, Co-free areas of the substrate with a depth deeper than the WC average grain size. Then, the weakly bonded carbide grains were dislodged by cavitation during an ultrasonic washing action after the chemical etching. As a result, the non-uniform-sized pitted areas appeared on the substrate surfaces after the WCE2 process. Thus, three repeated chemical etching processes over-treated the surface and provided porous textures due to the loss of WC grains and the Co depletion.

On the other hand, the RIBE process generated a rather smooth and uniform surface after all decoating cycles. Figure 3.12(d), g shows the morphologies of ion-etched surfaces after the 1st and 2nd decoating processes of the tool reconditioning, respectively. The roughness values of the etched surfaces consisted of *S*a of 0.085 µm and 0.087 µm after the 1st (RIBE1) and 2nd (RIBE2) decoatings, respectively. The observed effect of the partial surface integrity regeneration via RIBE can be attributed to the physical sputter etching of the damaged the WC-Co layer by energetic oxygen ions down to the pristine WC-Co.

The surface morphologies of the deposited diamond coatings are shown in Figure 3.12. The diamond surfaces, displayed in Figure 3.12(c, f) corresponding to the TLC0 and the TLC1, respectively, showed similar continuous, well-defined faceted textures of randomly oriented diamond grains with an average size of approximately 3 µm. Contrary, as shown in Figure 3.12(i), the diamond coating deposited on the TLC2 consisted of a combination of small faceted grains in globular agglomerated textures distributed mainly along the cutting edges.

This difference between the observed diamond films may be attributed to a high diamond nucleation density as the result of the rougher surface due to a huge amount of pits at the surface, as shown in Figure 3.12(h). As the depth of pits increased with the surface roughness, more diamond particles were embedded within the rough surfaces. This enhanced the nucleation of the diamond crystal and its growth behavior. Therefore, it can be proposed that the WCE2 process detrimentally reconstructed the surfaces, especially in the cutting edge areas, because over-treated surfaces induced the formation of non-uniform diamond films. A similar correlation between the substrate surface roughness and the diamond film morphology has been reported by Gomez et al. [129]. In their study, a diamond coating with a combination of small crystal facets in ball-like agglomerates was obtained on rougher samples compared between all pretreated samples.

In order to assess the quality of the deposited diamond coatings, Raman spectroscopy was employed. The Raman spectra of the diamond coatings are displayed in Figure 3.14, adopting the Raman microscope (RAMAN-11, Nanophoton) and a laser with a visible excitation wavelength of 532 nm.

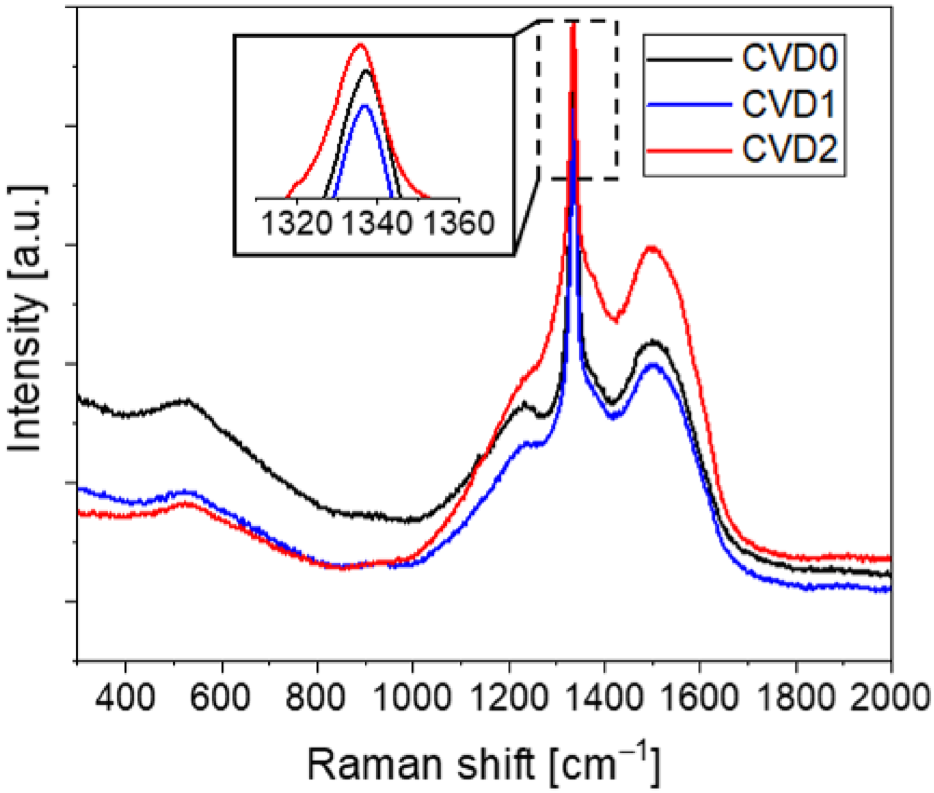

Figure 3.14. Raman spectra of the CVD0, CVD1, and CVD2 coatings, using a green (λ = 532 nm) excitation

It was found that the peak around 1332 cm^{-1}, indicative of the sp^3 bonding of the diamond [98], can be visible evidently for all the films. The Raman bands were present as 1337.27 cm^{-1}, 1337.28 cm^{-1}, and 1335.38 cm^{-1} in CVD0, CVD1, and CVD2 films deposited on the TLC0, the TLC1, and the TLC2, respectively. The wavelengths of these peaks shifted from the value of the natural diamond (1332.4 cm^{-1}), indicating the residual stress in the diamond films.

It is well-known that in the Raman spectra of a diamond coating, the peak close to 1332.4 cm^{-1} means the typical peak of the sp^3 diamond phase of the natural diamond without residual stress. The shift of this peak υ relative to 1332.4 cm^{-1} indicates residual stress in the coating. Estimation of the residual stress value in the diamond coating based on the Raman spectra can be done with the method described in the research of Ralchenko et al. [130]:

$$\sigma\ (\text{GPa}) = -0.567 \times (\upsilon - \upsilon_0), \qquad \text{(Eq.1)}$$

where υ_0 is 1332.4 cm^{-1} and the negative corresponds to the compressive stress.

According to this method, the residual stresses of the CVD0, CVD1, and CVD2 films were calculated as -2.761 GPa, -2.766 GPa, and -1.689 GPa, respectively. The CVD2 film had the lowest compressive stress value between the compared films, possibly due to the finer B-MCD structure and intergranular relaxation.

Furthermore, several visible peaks, characteristic of a diamond coating, can be identified as well. All presented Raman spectra showed two peaks located around 520 cm^{-1} and 1250 cm^{-1}, which are associated with the actual boron incorporation in the lattice [99]. In addition, the broad dominated peaks located around 1500 cm^{-1} for the CVD0, CVD1, and CVD2 films revealed the presence of sp^2 graphite (G-peak) phases [98]. The growth G-peak intensity of CVD2 can be associated with an increased non-diamond phase value due to reduced diamond grains.

3.4.2 Adhesion evaluation

In order to evaluate the adhesive strength between the deposited diamond coatings and the drill's substrate after the initial and reconditioning cycles, indentation tests were carried out using a Rockwell hardness testing machine with a diamond indenter, which had a conical angle of 120° and a radius of curvature at the tip 0.2 mm. Each diamond-coated drill was tested under a load of 980.7 N. Figure 3.15 shows the SEM images of the surface morphologies of the coated drills after the indentation tests. For the TLC0 and the TLC1, as shown in Figure 3.15(a) and (b), respectively, cracks of the diamond coatings around the indenter trace were observed. On the other hand, Figure 3.15(c) reveals the peeling of the diamond film of the TLC2 after indentation.

A magnified SEM image of the film-peeled area, presented in Figure 3.12(d), showed the substrate voids partially filled with the diamond material. The existence of the voids decreased the mechanical strength of the interface and created stress concentration regions. Thus, the adhesion force was significantly reduced.

The voids originated from the WCE2 step, as shown in Figure 3.12(h). Evidently, the diamond growth started inside the voids but did not completely fill them out before the continuous film coalesced and incapsulated the voids, blocking the gas-phase C transport and deposition in those areas. The findings suggested that the WCE2 and further step conditions should be fine-tuned in order to prevent the formation of excessively large craters and subsequent film voids. Another possible way is to apply the selective seeding process that stimulates an in-depth diamond growth, as has been reported by Linnik et al. [131].

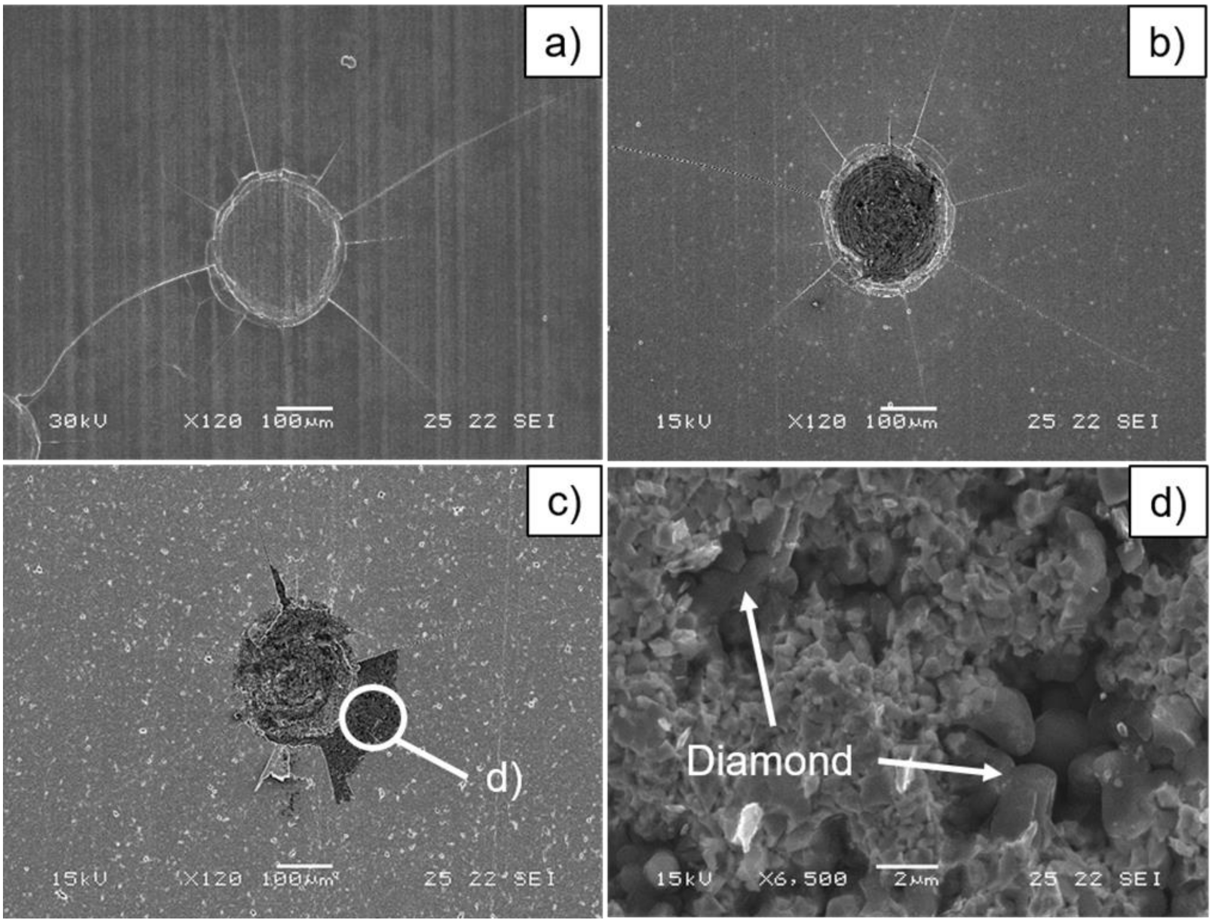
a)
30kV X120 100µm 25 22 SEI
b)
15kV X120 100µm 25 22 SEI
c)
d)
15kV X120 100µm 25 22 SEI
d)
Diamond
15kV X6,500 2µm 25 22 SEI

Figure 3.15. SEM images of indentation morphologies, obtained by a Rockwell testing machine with a load of 980.7 N on the TLC0 (a), the TLC1 (b), and the TLC2 (c, d)

3.4.3 Cutting edge rounding evaluation

In this study, the cutting edge rounding (CER) value was employed for the evaluation changing of the geometric shapes of drill cutting edges through the initial and reconditioning cycles of the experiments. A number of references reported the correlation between CER values and cutting forces, machined material delamination, etc. [59, 94, 100]. In addition, the CER parameter is frequently used as a criterion of tool wear, especially for non-coated WC-Co-based tools [36].

The CER values were measured on the tool substrates in two cutting edge places based on the applied one-shot drill shape. The first measurement position was determinate on the secondary cutting edge at 6 mm from the drill tip, and the drill cutting edge profile was characterized. It should be noted that the same position was used for the flank wear evaluation,

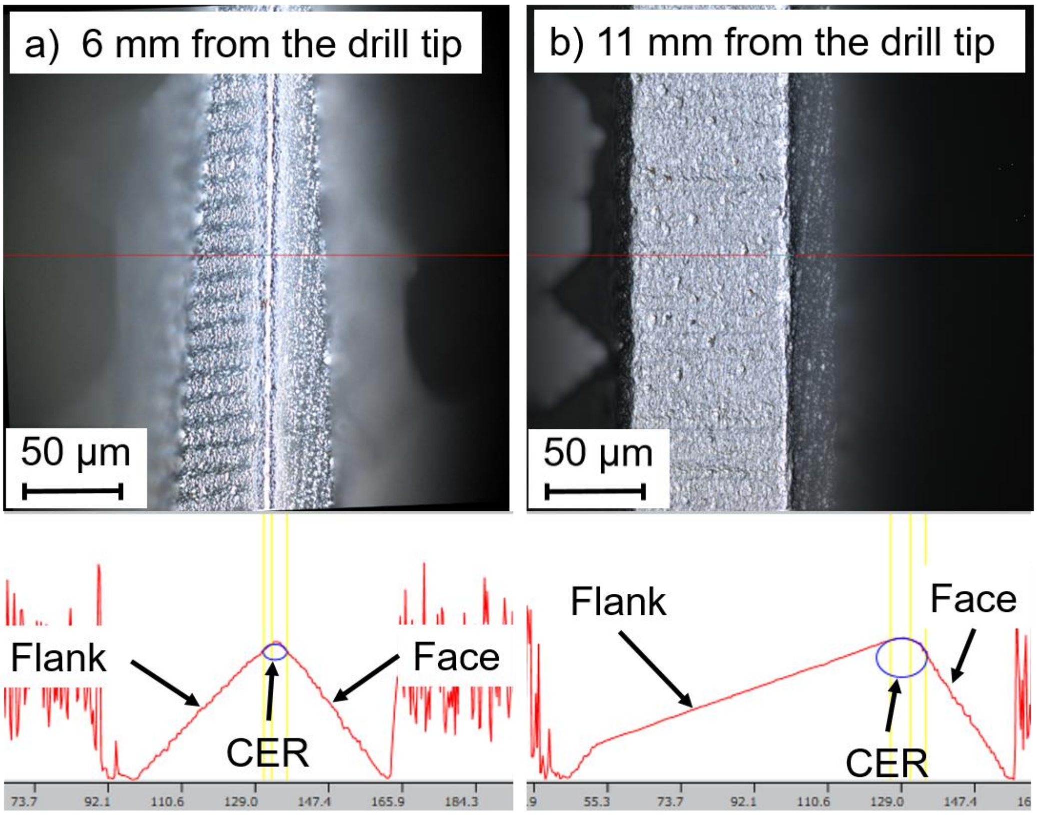

Figure 3.16. Measurement results of the cutting edge rounding (CER)

described in the following section. The second measurement position, associated with the reamer geometry, was on the tertiary cutting edge at 11 mm from the tip. Figure 3.16 shows the cutting edge profiles for both measurement positions described above carried out by a laser microscope (OLS4100, Olympus). First, the three-dimensional (3D) images of the cutting edge in the measurement positions were obtained from a surface area of 129 μm × 129 μm by an optical magnification of the system (100×). Then average values in this area for the edge radius were determined.

Figures 3.17 and 3.18 reveal the evolution of the CER values measured after the substrate treatment procedures. As shown in Figure 3.17, each pretreatment before diamond deposition led to increasing CER values. Because the chemical etching process accompanied the Co binder’s removal and loss of tungsten carbide grains, influencing the tool size and shape. On the contrary, the cutting edge sharpening effect was observed after the decoating stages. Although the film removal was not released uniformly for a complicated shape of the drill and the sputtering of the substrate occurred as well, the CER values decreased by approximately 0.5 μm every time for both the cutting edge geometries. The observed effect of micro-sharpening has been previously reported for medical needles exposed to ion beam irradiation with similar process parameters in the present study [125].

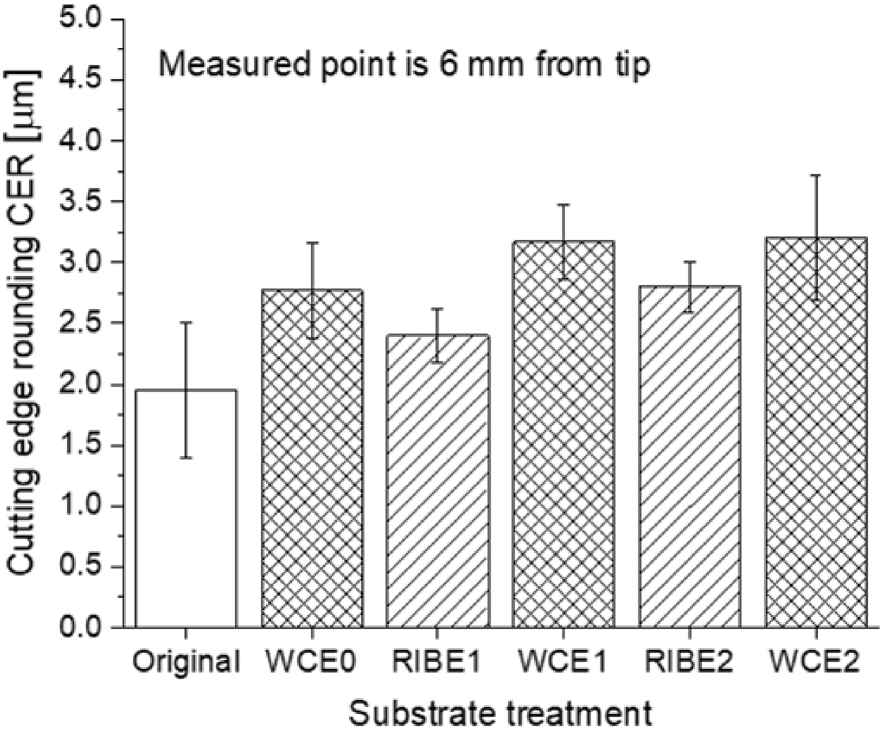

Figure 3.17. Change of the CER (6 mm measured point)

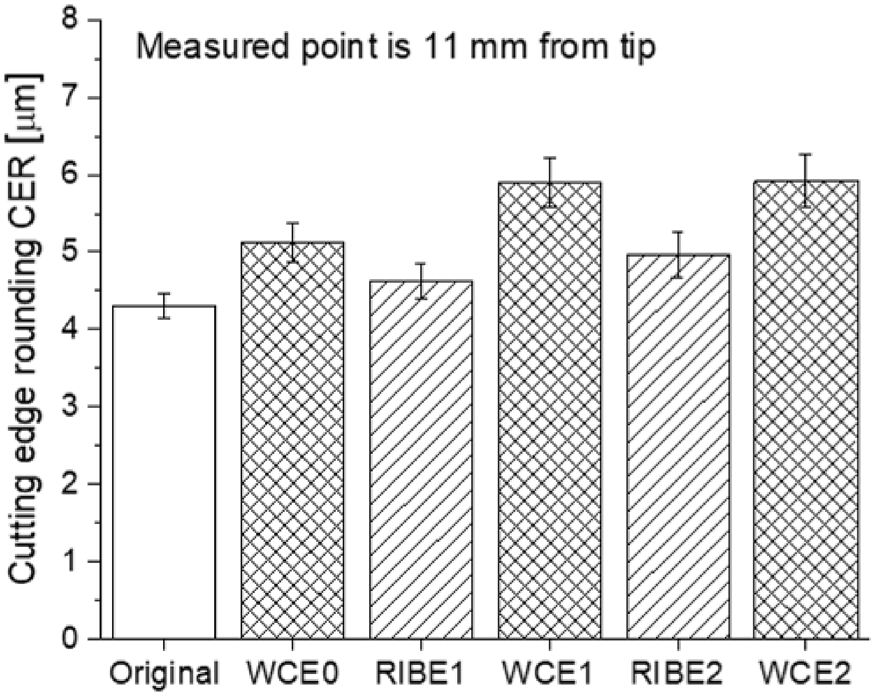

Figure 3.18. Change of the CER (11 mm measured point)

The mechanism consists in the incident angle-dependent sputtering yield, which drives the shape modification towards sharper edges in certain angle ranges and ion energies. For the cutting tools, the ion-induced sharpening of the edges may be beneficial from the standpoint of the cutting force reduction.

3.4.4 Drill flank wear evaluation

In the cutting tests, tool wear was evaluated as the maximum flank wear land width (*VB*max) as a function of the drilled hole number, as shown in Figure 3.19. Based on trial cutting test results, the *VB*max was always determined on the secondary cutting edge at 6 mm from the drill tip, which was placed close to the rounded corner connecting the secondary and the tertiary edges. Since there was a gradient in the tool wear from the corner of the drill cutting edge to the center, the area of the second cutting edge indicated above kept higher values of the flank wear measured in preliminary cutting tests compared to other areas of the drill edges.

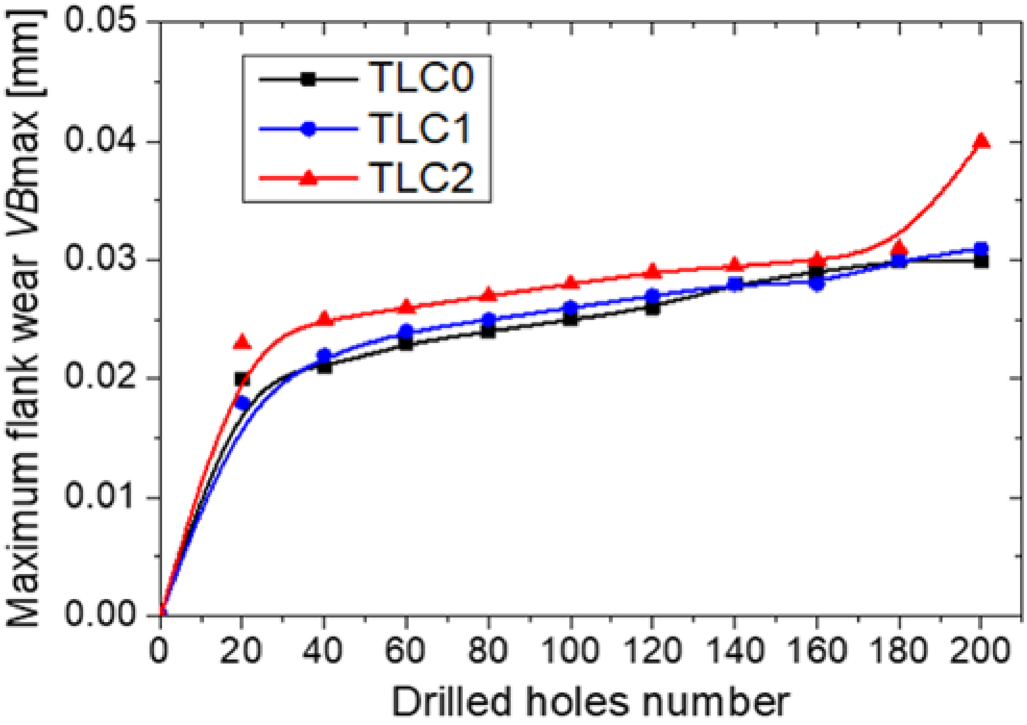

Figure 3.19. Variations of the maximum flank wear as a function of the drilled holes number

The results, shown in Figure 3.19, indicated that the evolution of the *VB*max values for the TLC0, the TLC1, and the TLC2 can be divided into two regions. The first region was the primary wear taking place, when ~40 holes were drilled. The second region was the region of steady-state wear observed between ~40 and 200 drilled holes. This was a normal operating region for the cutting tool. Some minor differences between the flank wear values were observed for the new and reconditioned diamond-coated drills. The abrasion of rough grains of the B-MCD film occurred with a fast increasing trend of the flank wear value, until 40 holes were drilled. Then, the smoothed diamond film led to the gradually increased wear, until 200 holes were drilled. However, the flank wear progress of the TLC2 showed a dramatically increasing trend after drilling 180 holes, which is typical for an accelerated wear region with the vanishing of the diamond film and the progressive substrate wear.

Figure 3.20 shows the wear morphologies of the tested drills after drilling 200 holes. For the TLC0, only the abrasion wear of the diamond film along the cutting edge was observed clearly, as shown in Figure 3.20(b) and (c). The TLC1 images (Figure 3.20e, f) showed the worn diamond film with localized film flaked areas, while the film detachments and the worn areas of the substrate were observed for the TLC2, as shown in Figure 3.20(i).

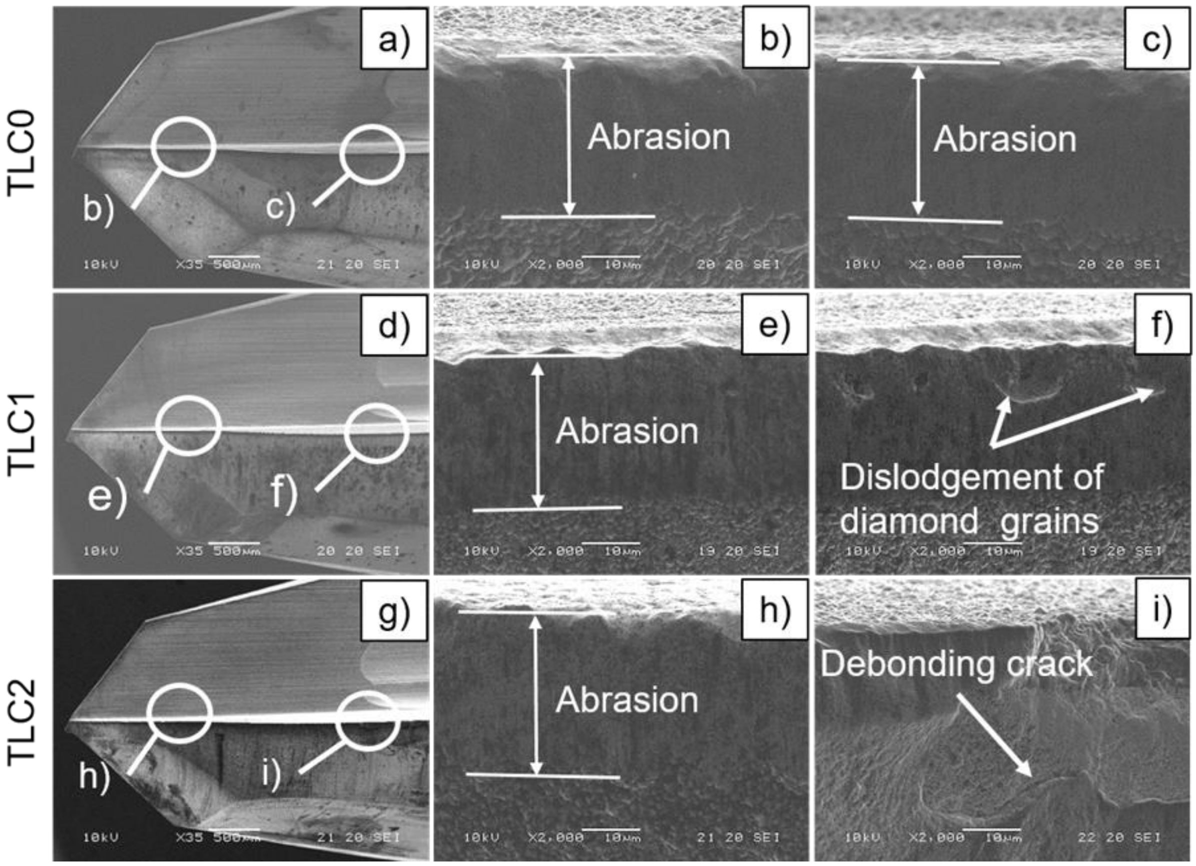

Figure 3.20. SEM images of the TLC0 (a–c), the TLC1 (d–f), and the TLC2 (g–i) after drilling 200 holes

During drilling, the cutting force instability produced by the altered orientation in the CFRP layers resulted in an intermittent cutting, which may have led to fatigue failure in the coating layer. In addition, a contact area was enhanced between the cutting edge and the machined surface due to the wear progress, which resulted in continuous or intermittent impacts and fluctuations of the cutting forces. These influences may induce additional shear stress and cracks beneath the film surface, as well. Such a cutting force combined effects, and the propagation of cracks along the film–substrate interface with the film detachment can occur. Therefore, the film detachment that occurred on the TLC2 could be attributed to the deteriorated adhesion between the diamond film and the WC-Co substrate by the 2nd-time reconditioning procedures, as discussed in the previous sections.

On the other hand, the drill tip areas of the TLC1 and the TLC2, as shown in Figure 3.20(e) and (h), had abrasion only, which can be explained as influencing the load of the thrust force mainly.

Despite that diamond film detachment occurred on the TLC2, it can be considered that all reconditioned drills showed flank wear values comparable with the new drill.

3.4.5 Thrust force evaluation

In this study, besides tool flank wear assessment, a thrust forces induced by the TLC0, TLC1 and TLC2 were evaluated as well due to its closely relating to the CFRP delamination, etc.

Detailed variation of the thrust forces produced during drilling of the CFRP workpiece using the one-shot drill can be seen in Figure 3.21. A shape of these forces relates to the shape of the drill and the workpiece thickness. Different drilling parameters do not alter the general shape but do alter the magnitude of thrust force. The thickness of the workpiece also affects the value of the thrust force.

The drilling process, presented in Figure 3.21, can be better explained if divided into four drilling stages indicating a typical variation trend. The gradual increment of the thrust force in the A-B area corresponds to the stage when the drill continuously cuts into the CFRP. Then the thrust force in the B-C area keeps relatively stable, because the primary, secondary and tertiary cutting edges contribute to the thrust force simultaneously. The slight reduction of the force in the C-D area is mainly caused by the drill tip has exited the bottom of the CFRP. Further, decreasing of the force in the D-E stage indicates the process when the drill cutting edges gradually come out of the CFRP laminate. On this stage, the reamer edges of the tool mainly contribute to the thrust force. Then the drill backs out of the workpiece. Presence the thrust

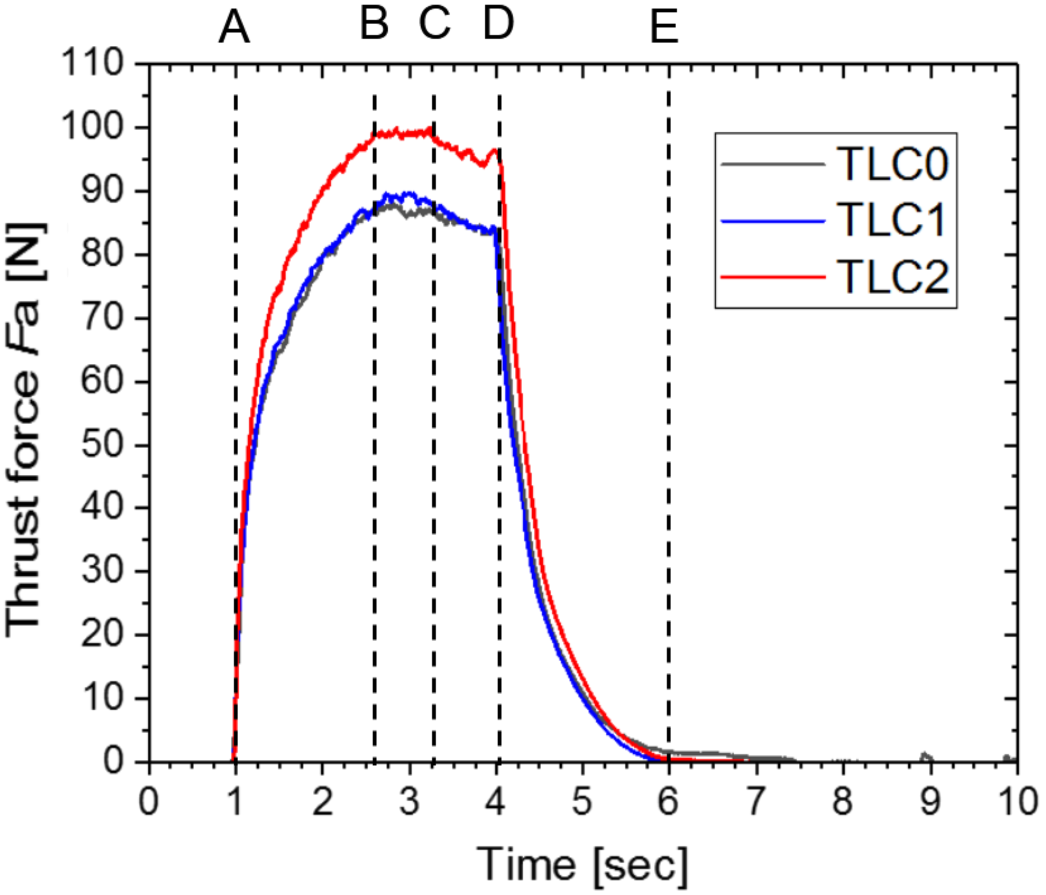

Figure 3.21. Variations of thrust forces for the TLC0, TLC1 and TLC2 during drilling process of 100th hole

force signal in drill back out area is occurred due to friction reamer edges to the hole wall. Therefore, reaming has continued while there is contact between the workpiece and the drill.

The variations of the thrust forces as a function of drilled holes' number are shown in Figure 3.22. The thrust forces, induced by all tested drills, are increased gradually, as the number of holes increased, which correlated with flank wear results shown in the previous section. Although the flank wear progress of the TLC2 showed a dramatically increasing trend after drilling 180 holes, the TLC2 induced thrust force shows low sensitive to the flank wear. That can be assumed that the current drill wear region has minor contribute in thrust force value.

The thrust forces, induced by TLC0 and TLC1, reveal similar trend. The difference with approximate value ~ 10 N has occurred between thrust forces induced by both TLC0, TLC1 compared with TLC2, as shown in Figures 3.21 and 3.22.

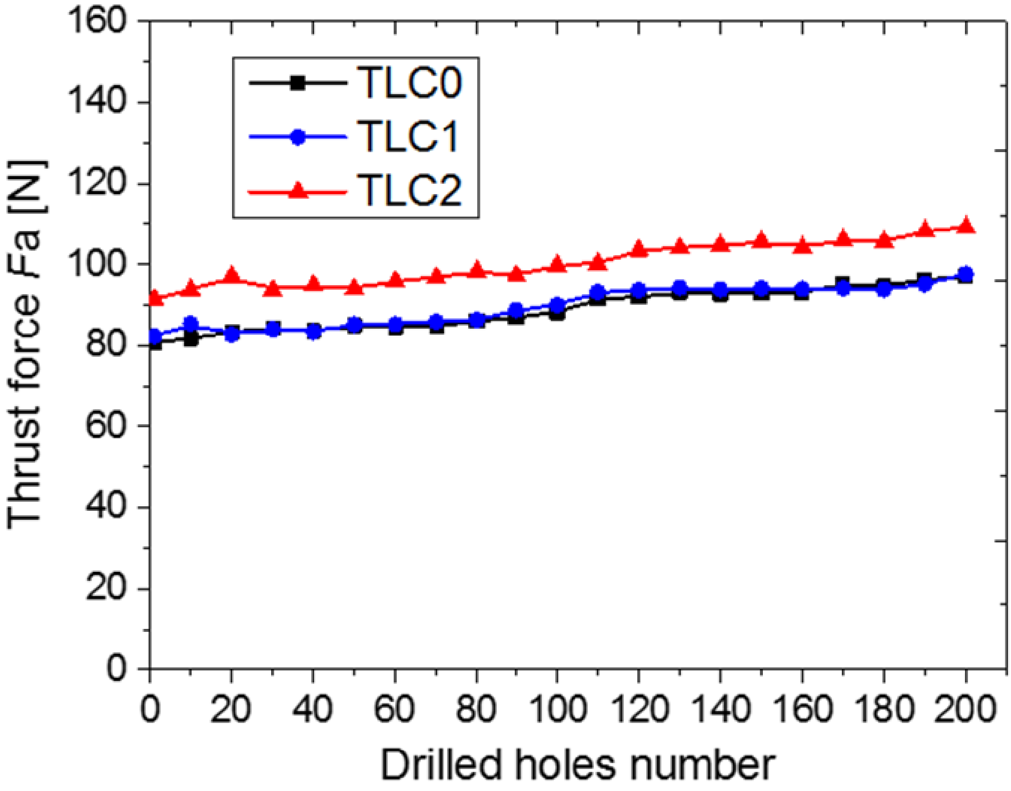

Figure 3.22. Variations of the thrust force as a function of drilled holes number

It is well known that the drilling force originates from two main aspects: the drilling resistance and friction resistance. The decreasing thrust force caused by the coverage of the diamond film should be attributed to the reduction of a coefficient of friction (COF) and corresponding friction resistance. However, due to most of the thrust force is caused by the drilling resistance, the influence of the tool shape on the thrust force is more obvious than the influence of the diamond film [61].

In our case, it can be assumed that influence of the diamond film provides, at least, equal contribution in the thrust force value. For instance, the reconditioning cycle procedures have created almost equal CER value of drill cutting edges, as shown in Figures 3.17 and 3.18. Moreover, deposited during the cycles diamond films reveal different surface morphologies. Indeed, as illustrated in Figure 3.23(g-i), TLC2 has diamond coating with non-uniform globular agglomerated textures distributed mainly along the cutting edges, compared with TLC0 and TLC1, as shown in Figure 3.23(a-c) and Figure 3.23(d-f) respectively. Such film morphology can increase drill cutting edge sizes locally, which led to increase the thrust force value.

Based on the results, it is possible to conclude that the reconditioned drills may induce predicted thrust force value, similar new drills.

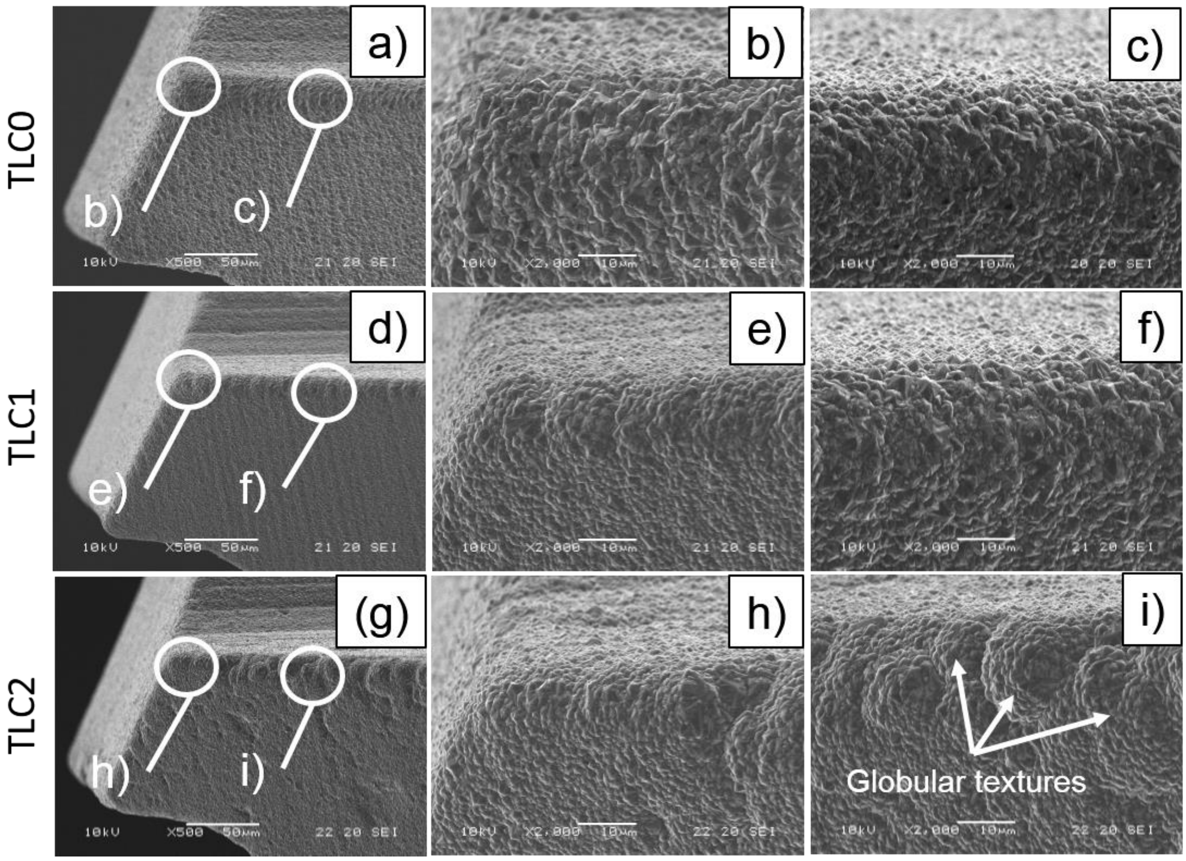
TLC0
TLC1
TLC2
a)
b)
c)
d)
e)
f)
(g)
h)
i)
Globular textures
10kV X500 50μm 21 20 SEI
10kV X2,000 10μm 21 20 SEI
10kV X2,000 10μm 20 20 SEI
10kV X500 50μm 22 20 SEI
10kV X2,000 10μm 22 20 SEI

Figure 3.23. SEM images of drill tip area of the TLC0 (a–c), the TLC1 (d–f), and the TLC2 (g–i) after diamond coating deposition

3.4.6 Hole quality evaluation

As described in the previous chapters, drilling CFRPs can induce damage surrounding the hole circumferences or inside the hole wall surfaces, including burrs, tearing, delamination, and matrix thermal damage. These defects affect the quality of drilled holes and may risk rejection of final composite structures. Moreover, delamination during drilling CFRP components has been recognized as the main irreparable failure that frequently occurs at the hole entry and exit sides. It is defined as the separation of adjacent composite plies and is characterized by interlaminar cracks in the material. The damage that occurs on the hole entrance is usually called peel-up delamination, while the hole exit damage is called push-out delamination. Peel-up delamination is a consequence of the cutting force pushing the separated and cut materials to the tool flute surface. In comparison, push-out delamination is caused by the thrust force bending the residual laminas shortly before the exit.

In this study, both types of CFRP delamination induced by the new and reconditioned drills were evaluated through the frequently used method proposed by Chen [35]. Delamination factor $F\mathrm{d}$ is defined as the ratio of the maximum diameter of a damaged zone ($D\mathrm{max}$, mm) to the nominal diameter of the hole (D, mm), and two circles are concentric. Then, the value of $F\mathrm{d}$ can be expressed as:

$$F\mathrm{d}=D\mathrm{max}/D, \qquad \text{(Eq.2)}$$

The maximal diameter of the damaged zone around each hole was measured using a digital microscope (VHX-1000SP, Keyence). For both delamination cases, as shown in Figures 3.24 and 3.25, the curves of the delamination induced by the TLC0 and the TLC1 showed similar behaviors and correlated with the drill flank wear data. The tool wear evolution generated an increase in the torque and the thrust force, which led to the CFRP delamination appearance. Indeed, when the cutting forces value exceeded the interlaminar fracture toughness of the laminates, delamination occurred.

Meanwhile, the TLC2 induced some delamination since the first hole was drilled, as shown in Figures 3.24 and 3.25. Further, the peel-up and push-out delamination curves showed gradually increased trends. Such curves behaviors can be explained as the effect of the non-uniform globular formation of the diamond film along the drill cutting edges. These formations generated varied edge geometries with different cutting angles that may lead to an unstable cutting process through the vibration with changing of the cutting forces. Subsequently, abrasion led to a smoothing of the diamond film, and the delamination curves correlated with the corresponding flank wear curve.

Figures 3.26 and 3.27 show images of hole entries and exits for the first and final holes drilled by the tested drills with the corresponding delamination factor values. The images presented the minor delamination of the last holes and the absence of cutting-induced breakout damages, such as burrs and splintering.

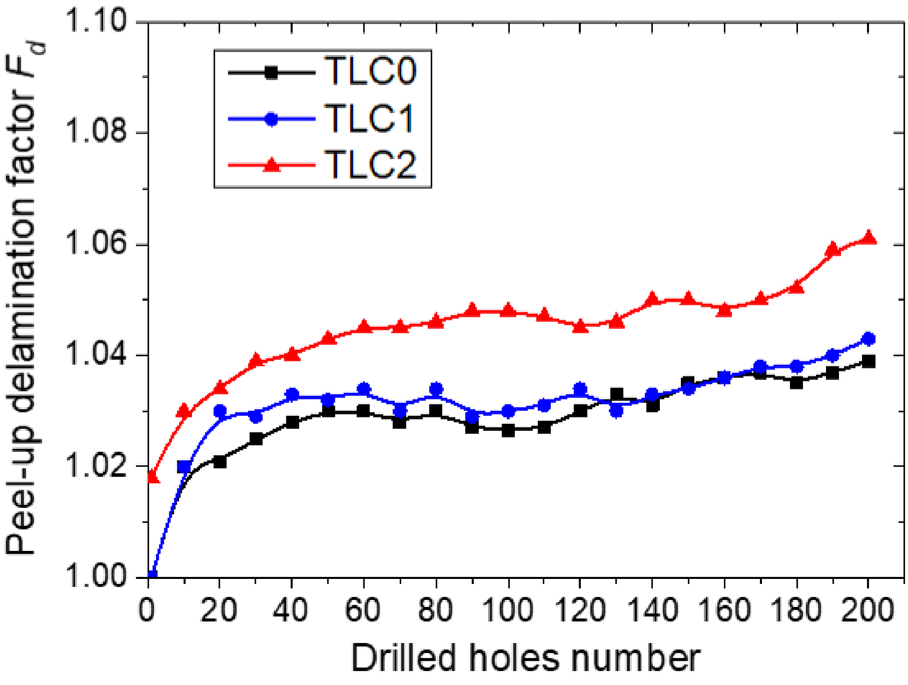

Figure 3.24. Variations of the delamination factor on the entry hole side as a function of the drilled holes number

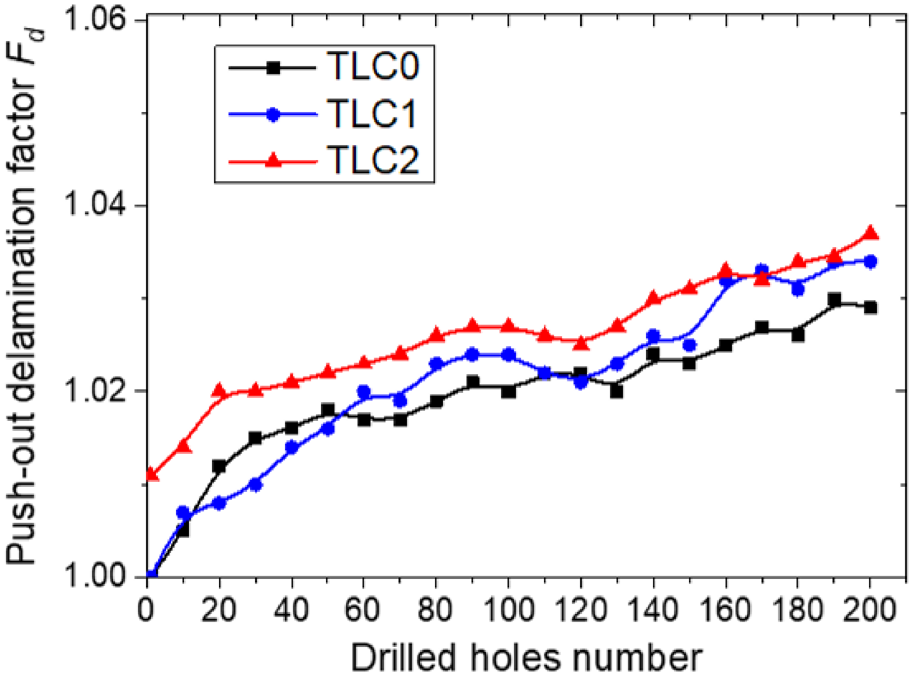

Figure 3.25. Variations of the delamination factor on the exit hole side as a function of the drilled holes number

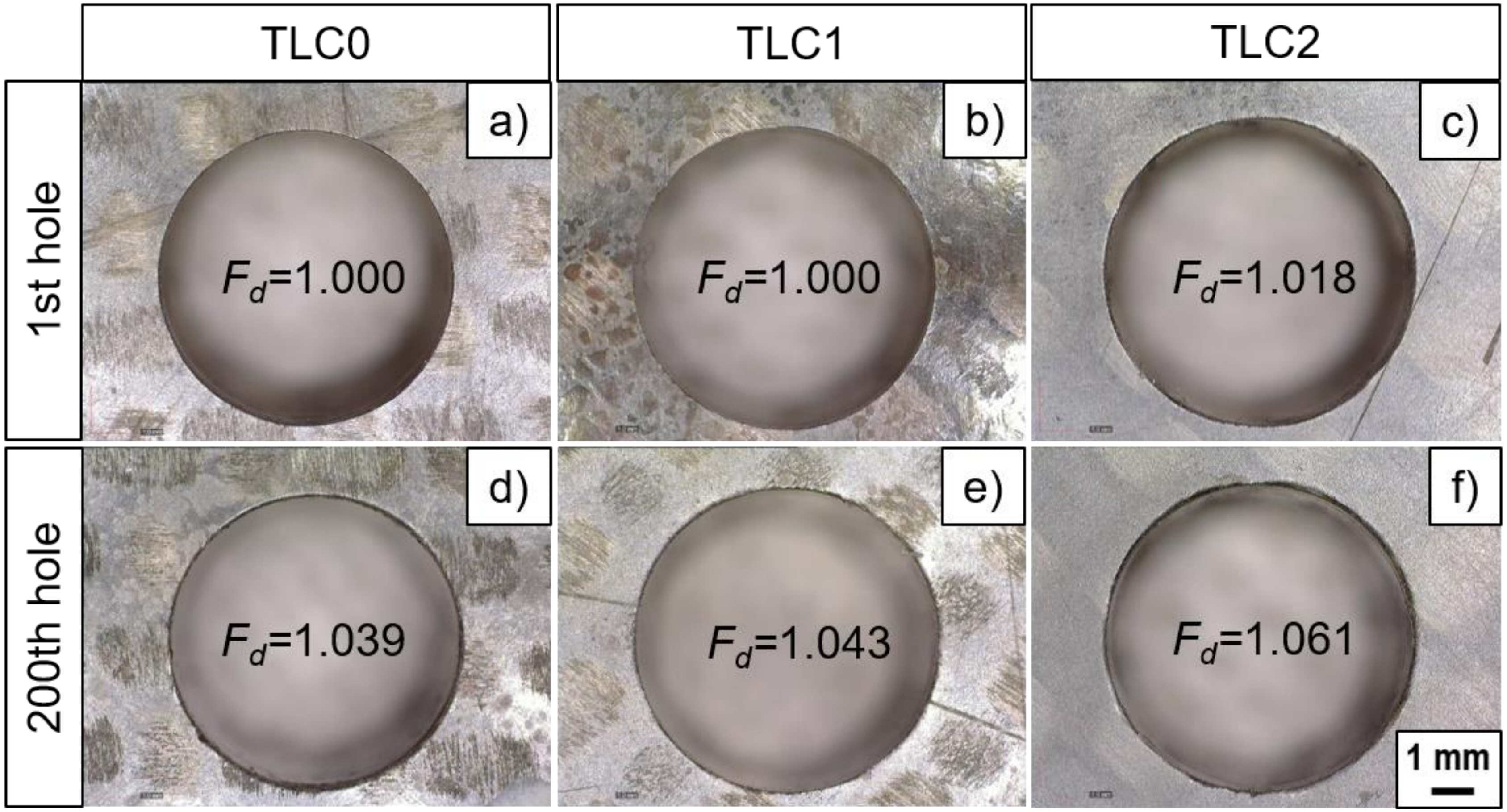
TLC0
TLC1
TLC2
1st hole
200th hole
a)
b)
c)
d)
e)
f)
F_d=1.000
F_d=1.000
F_d=1.018
F_d=1.039
F_d=1.043
F_d=1.061
1 mm

Figure 3.26**.** Images of the 1st and 200th CFRP hole entry sides made by the TLC0 (a, d), made by the TLC1 (b, e), and made by the TLC2 (c, f).

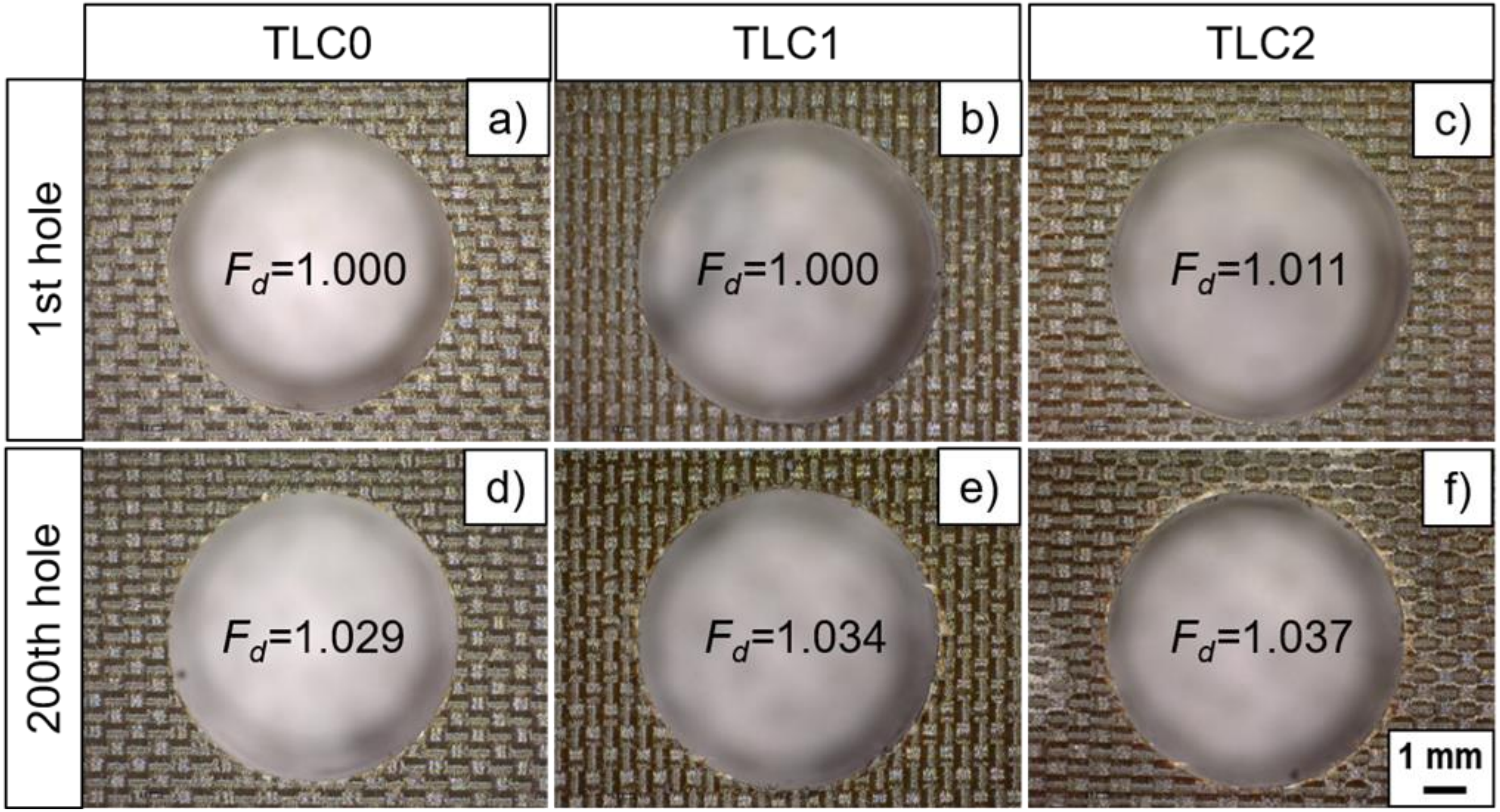
TLC0
TLC1
TLC2
1st hole
200th hole
a)
b)
c)
d)
e)
f)
F_d=1.000
F_d=1.000
F_d=1.011
F_d=1.029
F_d=1.034
F_d=1.037
1 mm

Figure 3.27. Images of 1st and 200th CFRP hole exit sides made by the TLC0 (a, d), made by the TLC1 (b, e), and made by the TLC2 (c, f).

Regarding the holes' size comparison, the drilled hole sizes were measured with a gauge plug having a nominal diameter of 6.36 mm. The gauge passed through all holes drilled by new and all reconditioned drills. Therefore, it is possible to conclude that the tested drills kept the drilled holes in the tolerance zone with the required size.

Based on the above evaluations, it was suggested that holes produced by the TLC0, the TLC1, and the TLC2 had comparable qualities in terms of the hole size and the delamination.

3.5 Conclusions

In this chapter, one-shot diamond-coated drills have been reconditioned two times without the drill regrinding between reconditioning processes. Then, the cutting performance of the reconditioned diamond-coated drills in drilling CFRP laminates was experimentally investigated and compared with the new diamond-coated drills. The main conclusions obtained were as follows:

(1) The RIBE decoating has demonstrated an insignificant influence on the WC-Co while completely removing a B-MCD film on the tool surfaces.

(2) The repeated substrate WCE pretreatment process resulted in increased crater formation in the WC-Co and should be tailored for the tool reconditioning in order to maintain the adhesion force of the B-MCD and maintain the WC-Co surface region mechanical robustness.

(3) The cutting performance of the reconditioned drills was confirmed through the drilling tests. All produced CFRP holes kept the required hole size and showed the absence of critical delamination and burrs. Moreover, even the two-time reconditioned drills showed the cutting performance results regarding the flank wear and the hole quality comparable with the new drills.

(4) The discussed RIBE-based reconditioning approach to the B-MCD-coated cutting tools may give significant advantages in CFRP machining in terms of the cost and the material savings and may facilitate a transition towards an eco-friendly circular economy.

Chapter 4. Conclusions

Nowadays, CFRP based composites became popular for use in a wide range of industries because of their high specific strength and stiffness coupled with damping properties and almost zero thermal expansion coefficient. Aerospace industry is major of composite application field, since benefits from composites are especially important where weight control is critical. For instance, CFRP enables weight reduction in transportation applications such as automobiles and aerospace that leads to energy reductions through fuel savings. It is estimated that every 10% of vehicle mass savings results in a 6%–8% improvement in fuel economy [3]. However, CFRP is one of the difficult-to-cut materials. The abrasive effect of hard carbon fibers in CFRP always leads to severe tool wear. Furthermore, when cutting tool conditions deteriorate due to wear and tear, the CFRP workpiece tends to show material-specific defects, such as delamination, burrs, and tearing of fibers. Research data show that the utilization of special shape-designed WC-Co tools with CVD diamond coatings give benefits in CFRP cutting performance. Also, the research data reveal that the interface adhesion between the diamond coatings and WC-Co tool substrates has a fatal effect on the cutting performance due to the peeling of the coating during machining. Considering that cemented carbide matrix contains Co as a binder and detrimental Co interaction with carbon during the diamond deposition process is well studied, many adhesions enhanced approaches were developed. One of the new promising ways of improving interface adhesion is boron doping into diamond coating.

Therefore, in this study, the effects of boron doping on the diamond films were investigated with the aims of improving film adhesion to WC-Co substrate and cutting performance of specially designed one-shot WC-Co drills with the doped diamond films when drilling CFRP. Three types of diamond coating, as B-MCD, B-NCD, and undoped NCD, were deposited on one-shot drills by the HFCVD method. The coating characteristics, such as surface morphology, roughness, carbon structure, and interfacial adhesion, were investigated. Then, cutting tests were carried out, and the tool's flank wear, thrust force, and torque were evaluated. Furthermore, drilled holes were inspected in terms of peel-up and push-out delamination.

The results obtained show that applied boron doping levels have influenced to deposited film properties. The deposited NCD and B-NCD diamond films have a significant distinction in surface morphologies. The B-NCD film has a homogeneous smooth surface with low visible fine ballas grains. In contrast, the NCD film shows a non-uniform surface with larger ballas grains. The B-MCD film exhibits a uniform rough surface with sharp grains. Raman spectra of the deposited diamond coatings shows the peaks related to corresponding film surface morphologies. Both boron-doped diamond films have peaks associated with boron presents. Moreover, the peak intensity has related with boron doped level. The Raman spectra of B-MCD coating show two broad peaks at 500.7 and 1223.8 cm^{-1} associated with boron doping. On the other hand, Raman spectra of the B-NCD coating show a relatively weaker peak at 517.8 cm^{-1} and not a clear visible peak near 1200 cm^{-1} compared with the B-MCD coating.

Adhesion estimation by Rockwell indentation test showed that film peeling areas around the indenter trace of both boron-doped diamond coatings were lower compared with NCD one. Furthermore, it was found that reduction in the boron doping level cannot compensate for the influence of impurities inherent to a diamond nanocrystalline film on it adhesion.

The cutting test results show the advantage of the B-MCD coated drill in terms of the flank wear value, the thrust force, and torque compared with the NCD and B-NCD coated drills.

Indeed, some minor differences between the flank wear values were observed until achieving 500 holes. Hereafter, the flank wear values have rapidly increased, especially for NCD and B-NCD coated drills, while the B-MCD coated drill kept a lower flank wear value. SEM observation of the tested drills, after drilling 600 holes, shows that the diamond film of NCD coated drill was removed along the cutting edges and the worn substrate has been observed clearly. On the other hand, for both boron-doped diamond coated drills, the worn diamond films with localized film flaked areas were observed. Moreover, the B-MCD coated drill showed lower film peeling and the flank wear value. This phenomenon could be attributed to enhanced adhesion between the diamond film and WC-Co substrate by application of appropriate boron doping level. Further, the quality of the CFRP drilled holes were evaluated. These results show that all diamond-coated drills generate stable peel-up and push-out delamination and uncut push-out burrs. Moreover, the B-MCD coated drill had generated the least push-out burrs.

To summarize, several important conclusions can be emphasized. Firstly, cutting test results confirm that appropriate boron doping of diamond coating enhances adhesion strength between the film and WC-Co substrate of the drill. Secondly, application of the B-MCD coating gives benefits in CFRP cutting performance compared with NCD and B-NCD coatings.

From the efficient cost-saving strategy point of view, reconditioning of the specially designed diamond coated tools is economically attractive due to their high cost and short tool life. Currently, the tool makers' industry does not have commercially available reconditioning techniques for the diamond-coated WC-Co tools at all. In this context, developed reconditioning approach to the diamond coated tools has been proposed. This approach consists in the reactive ion beam etching (RIBE) of a CVD diamond film by multiple closed electron drift ion sources (CDIS) and following deposition B-MCD film by HFCVD method.

In this research, the effects of RIBE decoating and surface pretreatment steps on WC-Co tools with a complex shape in terms of the ion-induced surface damage, geometry alteration, and adhesion of a subsequently re-applied CVD diamond film were experimentally investigated. Also, the cutting performance of the tools subjected to the RIBE decoating and repeated film deposition was evaluated via CFRP cutting tests and compared with the new diamond-coated drills. As result, one-shot diamond-coated drills have been reconditioned two times without the drill regrinding between reconditioning processes. Then, the cutting performance of the reconditioned diamond-coated drills in drilling CFRP laminates was experimentally investigated and compared with the new diamond-coated drills.

Based on the results, it is possible to conclude that the RIBE decoating has demonstrated an insignificant influence on the WC-Co while completely removing a B-MCD film on the tool surfaces. Meanwhile, the repeated substrate wet chemical etching (WCE) pretreatment process resulted in increased crater formation in the WC-Co and should be tailored for the tool reconditioning in order to maintain the adhesion force of the B-MCD and keep the WC-Co surface mechanical robustness. Indeed, the surface morphology after the initial WCE0 and WCE1 process of the 1st reconditioning cycle revealed a uniform surface with Sa value of 0.151 - 0.153 µm. However, the surface, produced by the WCE2 process of the 2nd reconditioning cycle, had a rougher texture with Sa of 0.160 µm and a lot of non-uniform-sized pitted areas. It is possible to propose that an accumulative effect of removing the binder phase in WCE stages led to the formation of randomly distributed, Co-free areas of the substrate with a depth deeper than the WC average grain size. Thus, three repeated chemical etching processes over-treated the surface and provided porous textures due to the loss of WC grains and the Co depletion. Such substrate pretreatment effect has influenced on surface morphologies of the deposited diamond coatings. The diamond surfaces, corresponding to the TLC0 and the TLC1, showed similar continuous, well-defined faceted textures of randomly oriented diamond grains with an average size of approximately 3 µm. Contrary, the diamond coating deposited on the TLC2 consisted of a combination of small faceted grains in globular agglomerated textures distributed mainly along the cutting edges. This difference between the observed diamond films may be attributed to a high diamond nucleation density as the result of the rougher surface. Raman spectra of the diamond film, related to TLC2, shows significant G-peak, as result of increased non-diamond phase value due to the diamond grain refinement. Results of adhesion evaluation by Rockwell indentation tests show that only some cracks of the diamond coatings around the indenter trace were observed for the TLC0 and the TLC1. On the other hand, the peeling of the TLC2 diamond film reveals after indentation. The SEM observation of the film-peeled area showed the substrate voids partially filled with the diamond material. The existence of the voids decreased the mechanical strength of the interface and created stress concentration regions. Therefore, it can be concluded that the WCE2 process detrimentally reconstructed the surfaces, especially in the cutting edge areas, because over-treated surfaces induced the formation of non-uniform diamond films and led reduction of film adhesion to the substrate. In order to evaluate changing of the geometric shapes of drill cutting edges through the initial and reconditioning cycles, the cutting edge rounding (CER) value was employed. As result, the cutting edge sharpening effect was observed after the decoating stages. Although the film removal was not released uniformly for a complicated shape of the drill and the sputtering of the substrate occurred as well, the CER values decreased by approximately 0.5 μm every time for the cutting edge geometries. Therefore, for the cutting tools, the ion-induced sharpening of the edges may be beneficial from the standpoint of the cutting force reduction.

To summarize experimental results, several important conclusions, written below, can be emphasized.

The cutting ability of the reconditioned drills was confirmed through the drilling tests. All reconditioned drills showed flank wear and thrust force values comparable with the new drill. Moreover, even the two-time reconditioned drills showed the cutting performance results regarding the flank wear and the hole quality comparable with the new drills.

The RIBE decoating has demonstrated ability to remove the diamond film on the tool surfaces without WC-Co substrate damage. Moreover, sharpening effect on the cutting edges of the reconditioned drills was observed after RIBE process.

The repeated substrate WCE pretreatment process resulted in increased crater formation in the WC-Co. In this context, the substrate pretreatment should be tailored for the tool reconditioning.

Finally, the developed RIBE-based reconditioning approach to the B-MCD-coated cutting tools gives significant advantages in CFRP machining in terms of the tool cost and the material savings and may facilitate a transition towards an eco-friendly circular economy.

Regarding of the future plan of experimental works, several aims should be discussed.

In order to determine limit number of tool reconditioning cycles without the tool regrinding, optimization of tool substrate pretreatment process is required.

Sharpening of tool cutting edges by RIBE application is promising approach. Therefore, further development this technology looks attractive for corresponding industrial fields.

References

1. Johnson, T., History of Composites. ThoughtCo, 2018, Available from https://www.thoughtco.com/history-of-composites-820404.
2. Gay, D., Hoa, S. and Tsai, S., Composite Materials – Design and Applications. 2003: CRC Press, ISBN 1-58716-084-6.
3. Das, S., Warren, J. and West, D., Global Carbon Fiber Composites Supply Chain Competitiveness Analysis. 2016, Available from https://www.osti.gov/servlets/purl/1333049
4. Callister, W. D. Jr., Rethwisch, D. G., Fundamentals of materials science and engineering: an integrated approach. 3rd Edition ed. 2008: Wiley, ISBN: 978-0-470-12537-3.
5. Brent A. Strong, Fundamentals of Composites Manufacturing: Materials, Methods, and Applications. 2008, Society of Manufacturing Engineers, ISBN 0-87263-854-5.
6. UMECO, An Introduction to Advanced Composites and Prepreg Technology. 2013 Available from https://www.yumpu.com/en/document/read/9334619/introduction-to-advanced-composites-and-prepreg-technology
7. Soutis, C., Fibre reinforced composites in aircraft construction, Progress in Aerospace Sciences, 2005, 41, p. 143-151. DOI: 10.1016/j.paerosci.2005.02.004.
8. Sheikh-Ahmed, J. Y., Machining of polymer composites. 2009, New York: Springer, ISBN: 978-0-387-35539-9. DOI:10.1007/978-0-387-68619-6.
9. Karataş, M.A., Gökkaya, H., A review on machinability of carbon fiber reinforced polymer (CFRP) and glass fiber reinforced polymer (GFRP) composite materials. Defence Technology, 2018, 14: p. 318 – 326. DOI: 10.1016/j.dt.2018.02.001.
10. König, W., Wulf, C., Graß, P. and Willerscheid, H., Machining of Fibre Reinforced Plastics. Annals of the CIRP, 1985. 34(2): p. 537 -548. DOI: 10.1016/S0007-8506(07)60186-3.
11. Bhatnagar, N., Ramakrishnan, N., Naik, N.K. and Komanduri, R., On the machining of fiber reinforced plastic (FRP) composite laminates. International Journal of Machine Tools and Manufacture, 1995. 35(5): p. 701 – 716. DOI: 10.1016/0890-6955(95)93039-9.
12. Teti, R., Machining of composite materials. Annals of the CIRP, 2002. 51(2): p. 611-634. DOI: 10.1016/S0007-8506(07)61703-X.
13. Ferreira, J.R., Coppini, N.L. and Miranda, G.W.A., Machining optimization in carbon fibre reinforced composite materials. Journal of Materials Processing Technology, 1999. 92 – 93: p. 135 – 140. DOI: 10.1016/S0924-0136(99)00221-6.

14. König, W., Graß, P., Quality Definition and Assessment in Drilling of Fibre Reinforced Thermosets. Annals of the CIRP, 1989. 38(1): p. 119 – 124. DOI: 10.1016/S0007-8506(07)62665-1.
15. John V. Foltz, Charles M. Blackmon, Metal-Matrix Composites, in ASM Handbook Vol. 2 Properties and Selection: Nonferrous Alloys and Special-Purpose Materials, 1990, ISBN: 978-1-62708-162-7. DOI: 10.31399/asm.hb.v02.a0001101.
16. Liu, D., Tang, Y. and Cong, W.L., A review of mechanical drilling for composite laminates. Composite Structures, 2012; 94: p. 1265–1279. DOI: 10.1016/j.compstruct.2011.11.024.
17. Chung, D. D. L., Carbon Fiber Composites. 1994, Newton: Butterworth-Heinemann. 215, ISBN: 0750691697.
18. Hexcel, Prepreg Technology, 2013. Available from https://kevra.fi/wp-content/uploads/Prepreg_Technology_.pdf
19. Brehl, D.E., Dow, T.A., Review of vibration-assisted machining. Precision Engineering, 2008. 32(3): p. 153 –172. DOI: 10.1016/j.precisioneng.2007.08.003.
20. Arul, S., Vijayaraghavan, L., Malhotra, S.K. and Krishnamurthy, R., The effect of vibratory drilling on hole quality in polymeric composites. International Journal of Machine Tools and Manufacture, 2006. 46(3-4): p. 252 – 259. DOI: 10.1016/j.ijmachtools.2005.05.023.
21. Linbo, Z., Lijiang, W. and Xin, W., Study on vibration drilling of fiber reinforced plastics with hybrid variation parameters method. Composites Part A: Applied Science and Manufacturing, 2003. 34(3): p. 237 – 244. DOI: 10.1016/S1359-835X(02)00207-5.
22. Makhdum, F., Phadnis, V.A., Roy, A. and Silberschmidt, V.V., Effect of ultrasonically-assisted drilling on carbon-fibre-reinforced plastics. Journal of Sound and Vibration, 2014. 333(23): p. 5939 –5952. DOI: 10.1016/j.jsv.2014.05.042.
23. Azmir, M. A. and Ahsan, A. K., Investigation on Glass/Epoxy Composite Surfaces Machined by Abrasive Water Jet Machining. Journal of Materials Processing Technology, 2008. 198(1-3), p. 122-128. DOI: 10.1016/j.jmatprotec.2007.07.014.
24. Shanmugam, D.K., Chen, F.L., Siores, E. and Brandt, M., Comparative study of jetting machining technologies over laser machining technology for cutting composite materials. Composite Structures, 2002. 57: p. 289 – 296. DOI: 10.1016/S0263-8223(02)00096-X.
25. Wang, J., A machinability study of polymer matrix composites using abrasive waterjet cutting technology. Journal of Materials Processing Technology, 1999. 94(1): p. 30 – 35. DOI: 10.1016/S0924-0136(98)00443-9.

26. Pan, C.T. and Hocheng, H., The anisotropic heat-affected zone in the laser grooving or fiber-reinforced composite material. Journal of Materials Processing Technology, 1996.62(1-3): p. 54 – 60. DOI: 10.1016/0924-0136(95)02192-2.
27. Cheng, C.F., Tsui, Y.C. and Clyne, T.W., Application of a three-dimensional heat flow model to treat laser drilling of carbon fibre composites. Acta Materialia, 1998. 46(12): p. 4273 – 4285. DOI: 10.1016/S1359-6454(98)00090-1.
28. Ouyang, W., Jiao, J., Xu, Z., et al., Experimental study on CFRP drilling with the picosecond laser “double rotation” cutting technique. Optics and Laser Technology, 2021. 142: 107238. DOI: 10.1016/j.optlastec.2021.107238.
29. Abrão, A.M., Faria, P.E., Davim J.P., et al., Drilling of fiber reinforced plastics: A review. Journal of Materials Processing Technology, 2007. 186: p. 1 – 7. DOI: 10.1016/j.jmatprotec.2006.11.146.
30. Zhang, H., Chen, W., Chen, D. and Zhang, l., Assessment of the exit defects in carbon fibre-reinforced plastic plates caused by drilling, Key Engineering Materials, 2001. 196: p. 43 – 52. DOI: 10.4028/www.scientific.net/KEM.196.43.
31. Xu, J., An, Q., Cai, X., et al., Drilling machinability evaluation on new developed high-strength T800S/250F CFRP laminates. International Journal of Precision Engineering and Manufacturing, 2013. 14(10): p. 1687 – 1696. DOI: 10.1007/s12541-013-0252-2.
32. Feito N., Álvarez J.D., Cantero J.L., et al., Influence of Special Tool Geometry in Drilling Woven CFRPs Materials. Procedia Engineering, 2015. 132: p. 632 – 638. DOI: 10.1016/j.proeng.2015.12.541.
33. Shyha, I.S.; Aspinwall, D.K.; Soo, S.L.; Bradley, S. Drill geometry and operating effects when cutting small diameter holes in CFRP. International Journal of Machine Tools and Manufacture, 2009. 49: p. 1008 – 1014. DOI: 10.1016/j.ijmachtools.2009.05.009.
34. Geng, D., Liu, Y., Shao, Z., et al., Delamination formation, evaluation and suppression during drilling of composite laminates: A review. Composite structures, 2019. 216: p. 168 – 186. DOI: 10.1016/j.compstruct.2019.02.099.
35. Chen, W.C., Some experimental investigations in the drilling of carbon fiber-reinforced plastic (CFRP) composite laminates. International Journal of Machine Tools and Manufacture, 1997. 37(8): p. 1097 – 1108. DOI: 10.1016/S0890-6955(96)00095-8.
36. Faraz, A., Biermann, D., Weinet, K., Cutting edge rounding: An innovative tool wear criterion in drilling CFRP composite laminates. International Journal of Machine Tools and Manufacture, 2009. 49: p. 1185 – 1196. DOI: 10.1016/j.ijmachtools.2009.08.002.
37. Davim, J.P., Rubio, J.C. and Abrão, A.M., A novel approach based on digital image analysis to evaluate the delamination factor after drilling composite laminates.

Composites Science and Technology, 2007. 67(9): p. 1939 – 1945. DOI: 10.1016/j.compscitech.2006.10.009.

38. Xu, J., Li, C., Mi, S., et al, Study of drilling induced defects for CFRP composites using new criteria, Composite Structures, 2018. 201: p. 1076 – 1087. DOI: 10.1016/j.compstruct.2018.06.051.
39. Bombardier Aerospace, Drilling of composites and composite/metallic assemblies. Process specification, 2011.
40. Turki, Y., Habak, M., Velasco, R., et al., Experimental investigation of drilling damage and stitching effects on the mechanical behavior of carbon/epoxy composites. International Journal of Machine Tools and Manufacture, 2014. 87: p. 61 - 72. DOI: 10.1016/j.ijmachtools.2014.06.004.
41. Xu, J., An, Q., Chen, M., A comparative evaluation of polycrystalline diamond drills in drilling high-strength T800S/250F CFRP. Composite Structures, 2014. 117: p. 71 – 82. DOI: 10.1016/j.compstruct.2014.06.034.
42. Geier, N., Davim, J.P., Szalay, T., Advanced cutting tools and technologies for drilling carbon fibre reinforced polymer (CFRP) composites: a review. Composites: Part A, 2019. 125: 105552. DOI: 10.1016/j.compositesa.2019.105552.
43. Gaitonde, V.N., Karnik, S.R., Rubio, J.C., et al., Analysis of parametric influence on delamination in high-speed drilling of carbon fiber reinforced plastic composites. Journal of Materials Processing Technology, 2008. 203: p. 431 – 438. DOI: 10.1016/j.jmatprotec.2007.10.050.
44. Heisel, U., Pfeifroth, T., Influence of point angle on drill hole quality and machining forces when drilling CFRP. Procedia CIRP, 2012. 1: p. 471 – 476. DOI: 10.1016/j.procir.2012.04.084.
45. Su, F., Zheng, L., Sun, F., et al., Novel drill bit based on the step-control scheme for reducing the CFRP delamination. Journal of Materials Processing Technology, 2018, 262: p. 157 – 167. DOI: 10.1016/j.jmatprotec.2018.06.037.
46. Fernandes, M, Cook, C., Drilling of carbon composites using a one shot drill bit. Part I: Five stage representation of drilling and affecting maximum force and torque. International Journal of Machine Tools and Manufacture, 2006. 46 (1): p. 70 – 75. DOI: 10.1016/j.ijmachtools.2005.03.015.
47. Murphy, C., Byrne, G. and Gilchrist, M.D., The performance of coated tungsten carbide drills when machining carbon fibre-reinforced epoxy composite materials. Proceedings of the Institution of Mechanical Engineers, Part B: Journal of Engineering Manufacture, 2002. 216 (2): p. 143 – 152. DOI: 10.1243/0954405021519735.

48. Jia, Z., Fu, R., Niu, B., et al., Novel drill structure for damage reduction in drilling CFRP composites. International Journal of Machine Tools and Manufacture, 2016. 110: p. 55 – 65. DOI: 10.1016/j.ijmachtools.2016.08.006.
49. Tsao, C.C. and Hocheng, H., The effect of chisel length and associated pilot hole on delamination when drilling composite materials. International Journal of Machine Tools and Manufacture, 2003. 43(11): p. 1087 – 1092. DOI:10.1016/S0890-6955(03)00127-5.
50. Tsao, C.C. and Chiu, Y.C., Evaluation of drilling parameters on thrust force in drilling carbon fiber reinforced plastic (CFRP) composite laminates using compound core-special drills. International Journal of Machine Tools and Manufacture, 2011. 51(9): p. 740 – 744. DOI: 10.1016/j.ijmachtools.2011.05.004.
51. Trent, E. and Wright, P., Metal cutting. 4th ed. 2001, Boston: Butterworth – Heinemann. ISBN: 0-7506-7069-X.
52. Lei, X., Wang, L., Shen, B., et al., Comparison of chemical vapor deposition diamond-, diamond-like carbon- and TiAlN-coated microdrills in graphite machining. Proceedings of the Institution of Mechanical Engineers, Part B: Journal of Engineering Manufacture, 2013. 227(9): p. 1299 – 1309. DOI: 10.1177/0954405413487898.
53. Heath, P.J., Developments in applications of PCD tooling. Journal of Materials Processing Technology, 2001. 116(1): p. 31 – 38. DOI: 10.1016/S0924-0136(01)00837-8.
54. Bouzakis, K.D., Michailidis, N., Skordaris, G., et al., Cutting with coated tools: Coating technologies, characterization methods and performance optimization. CIRP Annals - Manufacturing Technology, 2012. 61: p. 703 – 723. DOI: 10.1016/j.cirp.2012.05.006.
55. Asmussen, J. and Reinhard, D.K., Diamond Films Handbook. 2002, New York: Marcel Dekker Inc. ISBN: 0-8247-9577-6.
56. Vandevelde, T.C.S., Vandierendonck, K., Van Stappen, M., et al., Cutting applications of DLC, hard carbon and diamond films. Surface and Coating Technology, 1999. 113(1 – 2) p. 80 – 85. DOI: 10.1016/S0257-8972(98)00831-7.
57. Lifshitz, Y., Diamond – like carbon – present status. Diamond and Related Materials, 1999. 8(8-9): p. 1659 – 1676. DOI: 10.1016/S0925-9635(99)00087-4.
58. Mkaddem, A., Ben Soussia, A., El Mansori, M., Wear resistance of CVD and PVD multilayer coatings when dry cutting fiber reinforced polymers (FRP). Wear, 2013. 302: p. 946 – 954. DOI: 10.1016/j.wear.2013.03.017.
59. Wang, X., Kwon, P.Y., Sturtevant, C., et al., Tool wear of coated drills in drilling CFRP. Journal of Manufacturing Processes, 2013. 15: p. 127 – 135. DOI: 10.1016/j.jmapro.2012.09.019.

60. Davim, J.P. and Mata, F., Chemical vapour deposition (CVD) diamond coated tools performance in machining of PEEK composites. Materials & Design, 2008. 29(8): p. 1568 – 1574. DOI: 10.1016/j.matdes.2007.11.002.
61. Wang, X., Shen, X., Zeng, C. and Sun, F., Combined influences of tool shape and as-deposited diamond film on cutting performance of drills for CFRP machining. Surface and Coatings Technology, 2018. 347: p. 390 – 397. DOI: 10.1016/j.surfcoat.2018.05.024.
62. Zhang, J., Wang, X., Shen, B. and Sun, F., Effect of boron and silicon doping on improving the cutting performance of CVD diamond coated cutting tools in machining CFRP. International Journal of Refractory Metals and Hard Materials, 2013. 41: p. 285 – 292. DOI: 10.1016/j.ijrmhm.2013.04.017.
63. Wang, X., Shen, X., Yang, G. and Sun, F., Evaluation of boron-doped-microcrystalline/nanocrystalline diamond composite coatings in drilling of CFRP. Surface and Coatings Technology, 2017. 330: p.149 – 162. DOI: 10.1016/j.surfcoat.2017.10.002.
64. Wang, D.H., Ramulu, M. and Arola, D., Orthogonal cutting mechanisms of graphite/epoxy composite. Part I: unidirectional laminate. International Journal of Machine Tools and Manufacture, 1995. 35(12): p. 1623 – 1638. DOI: 10.1016/0890-6955(95)00014-O.
65. Tsao, C.C., Investigation into the effects of drilling parameters on delamination by various step-core drills. Journal of Materials Processing Technology, 2008. 206: p. 405 – 411. DOI: 10.1016/j.jmatprotec.2007.12.057.
66. Durão, L. M. P., Gonçalves, D. J. S., Tavares, J. M. R. S., Drilling tool geometry evaluation for reinforced composite laminates. Composite Structures, 2010. 92 (7): p. 1545 – 1550. DOI: 10.1016/j.compstruct.2009.10.035.
67. Iliescu, D., Gehin, D., Gutierrez, M. E., et al., Modeling and tool wear in drilling of CFRP. International Journal of Machine Tools and Manufacture, 2010. 50(2): p. 204 – 213. DOI: 10.1016/j.ijmachtools.2009.10.004.
68. Qiu, X., Li, P., Niu, Q., et al., New Compound Drill Bit for Damage Reduction in Drilling CFRP. International Journal of Precision Engineering and Manufacturing – Green Technology, 2019. 6(1): p. 75 – 87. DOI: 10.1007/s40684-019-00026-3.
69. Kuo, C., Soo, S., Aspinwall, D., et al., Tool wear and hole quality when single-shot drilling of metallic-composite stacks with diamond-coated tools. Proceedings of the Institution of Mechanical Engineers, Part B: Journal of Engineering Manufacture, 2014. 228(10): p. 1314 – 1322. DOI: 10.1177/0954405413517388.

70. Kuo, C., Wang, C. and Ko, S., Wear behavior of CVD diamond – coated tools in the drilling of woven CFRP composites. Wear, 2018. 398-399: p. 1 – 12. DOI: 10.1016/j.wear.2017.11.015.
71. Spitsyn, B., Bouilov, L., Deryagin, B., Diamond and diamond-like films: Deposition from the vapour phase, structure and properties. Progress in Crystal Growth and Characterization, 1988. 17: p. 79 – 170. DOI: 10.1016/0146-3535(88)90001-9.
72. Matsumoto, S., Sato, Y., Kamo, M. and Setaka, N., Vapor Deposition of Diamond Particles from Methane. Japanese Journal of Applied Physics, 1982. 21(4): p. 183 – 185. DOI: 10.1143/JJAP.21.L183.
73. Kamo, M., Sato, Y., Matsumoto, S. and Setaka, N., Diamond synthesis from gas phase in microwave plasma. Journal of Crystal Growth, 1983. 62: p. 642 – 644. DOI: 10.1016/0022-0248(83)90411-6.
74. Gracio, J.J., Fan, Q.H., Madaleno, J.C., Diamond growth by chemical vapour deposition. Journal of Physics D: Applied Physics, 2010. 43(37): p. 374017. DOI: 10.1088/0022-3727/43/37/374017.
75. Haubner, R., The history of hard CVD coatings for tool applications at the University of Technology Vienna. International Journal of Refractory Metals and Hard Materials, 2013. 41: p. 22 - 34. DOI: 10.1016/j.ijrmhm.2013.01.012.
76. Herlinger, J., Sp3's experience using hot filament CVD reactors to grow diamond for an expanding set of applications. Thin Solid Films, 2006. 501(1-2): p. 65 – 69. DOI: 10.1016/j.tsf.2005.07.108.
77. Sarangi, S.K., Chattopadhyay, A. and Chattopadhyay, A.K., Influence of process parameters on growth of diamond crystal on cemented carbide substrates by HFCVD system. International Journal of Refractory Metals and Hard Materials, 2012. 31: p. 1– 13. DOI: 10.1016/j.ijrmhm.2011.07.007.
78. Hu, J., Chou, Y.K., Thompson, R.G., et al., Characterizations of nanocrystalline diamond coating cutting tools. Surface and Coatings Technology, 2007. 202(4-7): p. 1113–1117. DOI: 10.1016/j.surfcoat.2007.07.050.
79. Deuerler, F., Lemmer, O., Frank, M., et al., Diamond films for wear protection of hardmetal tools. International Journal of Refractory Metals and Hard Materials, 2002. 20(2): p. 115 – 120. DOI: 10.1016/S0263-4368(02)00009-4.
80. Gåhlin, R., Alahelisten, A., Jacobson, S., The effects of compressive stresses on the abrasion of diamond coatings. Wear, 1996. 196(1 – 2): p. 226-233. DOI: 10.1016/0043-1648(95)06907-0.

81. Haubner, R., Kalss, W., Diamond deposition on hardmetal substrates – Comparison of substrate pre-treatments and industrial applications. International Journal of Refractory Metals and Hard Materials, 2010. 28(4): p. 475 – 483. DOI: 10.1016/j.ijrmhm.2010.03.004.
82. Haubner, R., Kubelka, S., Lux, B., et al., Murakami and H_2SO_4/H_2O_2 Pretreatment of WC-Co Hard Metal Substrates to Increase the Adhesion of CVD Diamond Coatings. Journal of Physics, 1995. 5: p. 753 – 760. DOI: 10.1051/jphyscol:1995589.
83. Polini, R., Chemically vapour deposited diamond coatings on cemented tungsten carbides: Substrate pretreatments, adhesion and cutting performance. Thin Solid Films, 2006. 515(1): p. 4 – 13. DOI: 10.1016/j.tsf.2005.12.042.
84. Sommer, M., Haubner, R., Lux, B., Diamond deposition on copper treated hardmetal substrates. Diamond and Related Materials, 2000. 9(3-6): p. 351 – 357. DOI: 10.1016/S0925-9635(99)00250-2.
85. Endler, I., Leonhardt, A., Born, R., et al., Interlayers for diamond deposition on tool materials. Diamond and Related Materials, 1996. 5(3-5): p. 299 – 303. DOI: 10.1016/0925-9635(95)00352-5.
86. Haubner, R., Lux, B., Diamond deposition on steel substrates using intermediate layers. International Journal of Refractory Metals and Hard Materials, 2006. 24(5): p. 380–386. DOI: 10.1016/j.ijrmhm.2005.11.008.
87. Sarangi, S.K., Chattopadhyay, A. and Chattopadhyay, A.K., Effect of pretreatment, seeding and interlayer on nucleation and growth of HFCVD diamond films on cemented carbide tools. International Journal of Refractory Metals and Hard Materials, 2008. 26(3): p. 220 – 231. DOI: 10.1016/j.ijrmhm.2007.05.002.
88. Ullram, S., Haubner, R., Temperature pre-treatments of hardmetal substrates to reduce the cobalt content and improve diamond deposition. Diamond and Related Materials, 2006. 15: p. 994 – 999. DOI: 10.1016/j.diamond.2005.12.055
89. Wang, X., Zhang, J., Sun, F., et al., Fracture and solid particle erosion of micro-crystalline, nano-crystalline and boron-doped diamond films. International Journal of Refractory Metals and Hard Materials, 2014. 45: p. 31 – 40. DOI: 10.1016/j.ijrmhm.2014.02.005.
90. Gaydaychuk, A., Linnik, S., Zenkin, S., High temperature tribology of heavily boron doped diamond films against steel. International Journal of Refractory Metals and Hard Materials, 2020. 88: 105191. DOI: 10.1016/j.ijrmhm.2020.105191.
91. Srikanth, V., Sampath Kumar, P., Bhooshan Kumar, V., A Brief Review on the *In Situ* Synthesis of Boron-Doped Diamond Thin Films. International Journal of Electrochemistry, 2012. 2012: 218393. DOI: 10.1155/2012/218393.

92. Kalss, W., Bohr, S., Haubner, R., et al., Influence of Boron on Diamond Growth on WC-Co Hardmetals. International Journal of Refractory Metals and Hard Materials, 1996. 14: p. 137 – 144. DOI: 10.1016/0263-4368(96)83427-5.
93. Roy, M., Dua, A.K., Nuwad, J., et al., Controlled in situ boron doping of diamond thin films using solution phase. Journal of Applied Physics, 2006. 100(12): p. 124506. DOI: 10.1063/1.2400806.
94. Wang, F., Qian, B., Jia, Z., et al. Secondary cutting edge wear of one-shot drill bit in drilling CFRP and its impact on hole quality. Composite Structures, 2017. 178: p. 341–352. DOI: 10.1016/j.compstruct.2017.04.024.
95. Wang, X., Wang, C., Sun, F. Development and growth time optimization of boron-doped micro-crystalline, undoped micro-crystalline and undoped nanocrystalline composite diamond film. Proceedings of the Institution of Mechanical Engineers, Part B: Journal of Engineering Manufacture, 2018. 232(7): p. 1244 – 1258. DOI: 10.1177/0954405416666902.
96. Ferrari, A.C., Robertson, J., Raman spectroscopy of amorphous, nanostructured, diamond–like carbon, and nanodiamond. Philosophical Transactions of the Royal Society A, 2004. 362: p. 2477 – 2512. DOI: 10.1098/rsta.2004.1452.
97. Pfeiffer, R., Kuzmany, H., Knoll, P., et al., Evidence for trans-polyacetylene in nanocrystalline diamond films. Diamond and Related Materials, 2003. 12: p. 268 – 271. DOI: 10.1016/S0925-9635(02)00336-9.
98. May, P.W., Ludlow, W.J., Hannaway, M., et al., Raman and conductivity studies of boron-doped microcrystalline diamond, facetted nanocrystalline diamond and cauliflower diamond films. Diamond and Related Materials, 2008. 17(2): p. 105 – 117. DOI: 10.1016/j.diamond.2007.11.005.
99. Ushizawa, K., Watanabe, K., Ando, T., et al., Boron concentration dependence of Raman spectra on {100} and {111} facets of B-doped CVD diamond. Diamond and Related Materials, 1998. 7(11-12): p. 1719 – 1722. DOI: 10.1016/s0925-9635(98)00296-9.
100. Gaugel, S., Sripathy, P., Haeger, A., et al., A comparative study on tool wear and laminate damage in drilling of carbon-fiber reinforced polymers (CFRP). Composite Structures, 2016. 155: p. 173 – 183. DOI: 10.1016/j.compstruct.2016.08.004.
101. Wang, X., Shen, X., Sun, F., et al., Influence of boron doping level on the basic mechanical properties and erosion behavior of boron-doped micro-crystalline diamond (BDMCD) film. Diamond and Related Materials, 2017. 73: p. 218 – 231. DOI: 10.1016/j.diamond.2016.09.025.

102. Zhang, J., Yuan, Y., Zhang, J., Cutting Performance of Microcrystalline, Nanocrystalline and Dual-Layer Composite Diamond Coated Tools in Drilling Carbon Fiber Reinforced Plastics. Applied Sciences, 2018. 8: 1642. DOI: 10.3390/app8091642.
103. Astakhov, V.P., Drills: Science and Technology of Advanced Operations. 2014: CRC Press, ISBN 9781466584341.
104. Bouzakis, K.D., Lili, E., Michailidis, N., et al., Manufacturing of cylindrical gears by generating cutting processes: A critical synthesis of analysis methods. CIRP Annals, 2008. 57(2): p. 676 – 696. DOI: 10.1016/j.cirp.2008.09.001.
105. Available from https://www.sandvik.coromant.cn/en-us/services/pages/reconditioning.aspx
106. Toboła, D., Czechowski, K., Wroñska, I., et al., The effects of the coating stripping process on regenerated tool cutting edges. Journal of Achievements in Materials and Manufacturing Engineering, 2013. 61(2): p. 294 – 301.
107. Bonacchi, D., Rizzi, G., Bardi, U., et al., Chemical stripping of ceramic films of titanium aluminum nitride from hard metal substrates. Surface and Coatings Technology, 2003. 165: p. 35 – 39. DOI: 10.1016/S0257-8972 (02)00720-X.
108. Ardila, L.C., Moreno, C.M., Sánchez, J.M., Electrolytic removal of chromium rich PVD coatings from hardmetals substrates. International Journal of Refractory Metals and Hard Materials, 2010. 28: p. 155 – 162. DOI: 10.1016/j.ijrmhm.2009.07.008.
109. Stoikou, M.D., Etching of CVD Diamond Surfaces. 2010. Available from http://www.ros.hw.ac.uk/handle/ 10399/2441
110. Bello, I., Fung, M.K., Zhang, W.J., et al., Effects at reactive ion etching of CVD diamond. Thin Solid Films, 2000. 368: p. 222 – 226. DOI: 10.1016/s0040-6090(00)00769-0.
111. Jacob, W., Hopf, C., Schlüter, M., Chemical sputtering of carbon materials due to combined bombardment by ions and atomic hydrogen. Physica Scripta, 2006. T124: p. 32 – 36. DOI: 10.1088/0031-8949/2006/T124/007.
112. Cuesta, A., Martınez-Alonso, A., Tascón, J.M., Carbon reactivity in an oxygen plasma: a comparison with reactivity in molecular oxygen. Carbon, 2001. 39: p. 1135 – 1146. DOI: 10.1016/S0008-6223 (00)00235-9.
113. Leech, P.W., Reeves, G.K., Holland, A., Reactive ion etching of diamond in CF_4, O_2, O_2 and Ar-based mixtures. Journal of Materials Science, 2001. 36(14): p. 3453 – 3459. DOI: 10.1023/a:1017964129419.
114. Yunata, E.E., Aizawa, T., Yamauchi, K., High density oxygen plasma ashing of CVD-diamond coating with minimum damage to WC (Co) tool substrates. Mechanical Engineering Journal, 2016. 3: 15 – 00533. DOI: 10.1299/mej.15-00533.

115. Yunata, E.E., Aizawa, T., Tamaoki, K., Kasugi, M., Plasma Polishing and Finishing of CVD-Diamond Coated WC (Co) Dies for Dry Stamping. Procedia Engineering, 2017. 207: p. 2197 – 2202. DOI: 10.1016/J.PROENG.2017.10.981.
116. Liu, H., Hanyu, H., Murakami, Y., et al., Recycling technique for CVD diamond coated cutting tools. Surface and Coatings Technology, 2001. 137: p. 246 – 248. DOI: 10.1016/S0257-8972 (00)01081-1.
117. Remnev, A., Uemura, K., Geometrical aspects of ion beam and plasma-based stripping processes for refurbishing cutting tools. Japanese Journal of Applied Physics, 2019. 58: SAAB04. DOI: 10.7567/1347-4065/aaec8c.
118. Remnev, A., Reactive ion beam stripping process for diamond coated cutting tools reconditioning. Surface and Coatings Technology, 2019. 378: 124939. DOI: 10.1016/j.surfcoat.2019.124939.
119. Shirk, M.D., Molian, P.A., Malshe, A.P., Ultrashort pulsed laser ablation of diamond. Journal of Laser Applications, 1998. 10: p. 64 – 70. DOI: 10.2351/1.521822.
120. Duhopelnikov, D., Experimental study of ion accelerator “RADICAL” without cathode-neutralizer. Vestnik MGTU (by Russian), 2004. p. 74 – 83.
121. Zhurin, V.V., H R Kaufman, H.R., Robinson, R.S., Physics of closed drift thrusters. Plasma Sources Science and Technology, 1999. 8(1): R1-R20. DOI: 10.1088/0963-0252/8/1/021.
122. Hopf, C., Schlüter, M., Jacob, W., Chemical sputtering of carbon films by argon ions and molecular oxygen at cryogenic temperatures. Applied Physics Letter, 2007. 90: 224106. DOI: 10.1063/1.2745267.
123. Klocke, F., Krieg, T., Coated tools for metal cutting – features and applications. CIRP Annals, 1999. 48(2): p. 515 – 525. DOI: 10.1016/S0007-8506(07)63231-4.
124. Remnev, A., Nagato, K., Uemura, K., Effect of reactive gas additives on surface morphology evolution of stainless steel substrate undergoing low energy Ar ion bombardment. Vacuum, 2015. 119: p. 223 – 227. DOI: 10.1016/j.vacuum.2015.05.024.
125. Remnev, A., Nagato, K., Uemura, K., Effect of working gas composition in medical needle sharpening by ion beam sputtering. Biomedical Physics and Engineering Express, 2018. 4(2): 25033. DOI: 10.1088/2057-1976/aa9b3d.
126. US8734067B2 Drill, 27.05.2014.
127. Available from https://www.shinmaywa.co.jp/pbp/english/index.html
128. Hegeman, J.B.J.W., De Hosson, J.T.M., De With, G., Grinding of WC-Co hardmetals. Wear, 2001. 248: p. 187 – 196. DOI: 10.1016/S0043-1648(00)00561-5.

129. Gomez, H., Durham, D., Xiao, X., et al., Adhesion analysis and dry machining performance of CVD diamond coatings deposited on surface modified WC-Co turning inserts. Journal of Materials Processing Technology, 2012. 212: p. 523 – 533. DOI: 10.1016/j.jmatprotec.2011.10.020.

130. Ralchenko, V.G., Smolin, A.A., Pereverzev, V.G., et al. Diamond deposition on steel with CVD tungsten intermediate layer. Diamond and Related Materials, 1995. 4: p. 754 – 758. DOI: 10.1016/0925-9635(94)05299-9.

131. Linnik, S., Gaydaychuk, A., Okhotnikov, V., Improvement to the adhesion of polycrystalline diamond films on WC-Co cemented carbides through ion etching of loosely bound growth centers. Surface and Coatings Technology, 2018. 334: p. 227 – 232. DOI: 10.1016/j.surfcoat.2017.11.043.

Acknowledgements

The present work was carried out at the Nontraditional Machining (NTN) Laboratory, the Graduate School of Natural Science and Technology, Okayama University and Laboratory of Advanced Technologies of Industrial Machinery System Division, ShinMaywa Industries, Ltd. This doctoral thesis would not possible without the guidance and the cooperation of several individuals who contributed and extended their valuable assistance in the preparation and completion of this study.

First and foremost, my utmost gratitude to Head of NTN Laboratory, Prof. Akira Okada, for his guidance and supervision throughout my doctoral course studies at all. His excellent mentorship and patience during my 6 years of study has been invaluable for understanding the value of scientific research. On a personal level, I will never forget the valuable discussions and advice related to both my academic and non-academic matters.

I would also like to thank Prof. Masahiro Fujii and Prof. Kazuhito Ohashi for their guiding comments and revision of this thesis.

Special thanks to my former head Prof. Kensuke Uemura, ITAC Ltd of ShinMaywa Industries, for assigning me for the project and motivating me to engage in the doctor course.

I thank past and present members of NTM Laboratory for the support, continuous assistance and cooperation. Sincere thanks to Dr. Yasuhiro Okamoto and Dr. Togo Shinonaga for their valuable advice and revision of this thesis. Also, I am very appreciative to Ms. Hiroko Matsumoto for her secretarial support.

I would like to express my gratitude to Dr. Hitoshi Ogawa, Tokushima ITC, and Dr. Alexey Remnev, ITAC Ltd of ShinMaywa Industries, for their valuable input in this research work.

I also appreciate the support from ShinMaywa Industries. I especially thank Mr. Koichi Okamoto and Mr. Shumpei Asai for their inspiration, encouragement and great support in my difficult time. Special thanks to Mr. Yasuhiro Koizumi who helped me in the experimental works.

Finally, special and deep appreciation to my wife Olga and my kids, Michael and Nikita, for their support, patience and encouragement during this study.

List of publications

Journal

1. A. Soldatov, A. Okada, H. Ogawa, Cutting performance evaluation of boron-doped and undoped diamond coatings in drilling of CFRP laminates, Proceedings of the Institution of Mechanical Engineers, Part B: Journal of Engineering Manufacture, Vol. 236, issue 5, pp. 614 - 624, (2021). DOI: 10.1177/09544054211040624.
2. A. Soldatov, A. Remnev, A. Okada, Reconditioning of Diamond Coated Tools and Its Impact on Cutting Performance for CFRP Laminates, Applied Sciences, Vol. 12, No.3, pp. 1288: 1 - 17, (2022). DOI: 10.3390/app12031288.

Conference

1. A. Soldatov, A. Okada and K. Uemura, Investigation of Nanocrystalline Diamond Coating on Cutting Tools for CFRP, The 2nd International Conference on Machining, Materials and Mechanical Technologies (IC3MT), p.43, (Matsue, Japan, 2016-10).
2. A. Soldatov, A. Okada, K. Uemura, H. Ogawa, Cutting Performance of Boron-doped Diamond Coated Tools in Drilling of CFRP, The 9th International Conference on Leading Edge Manufacturing in 21st Century (LEM21), in Electronic Proceedings, (Hiroshima, Japan, 2017, 11). DOI: 10.1299/jsmelem.2017.9.008.
3. A. K. Soldatov, A. Okada, A. G. Remnev, K. Uemura, Investigation of Refurbishing Technique for Diamond Coated Tools, The 6th International Congress on Energy Fluxes and Radiation Effects (EFRE 2018), p.391, (Tomsk, Russian Federation, 2018-09).

Patent

1. 多結晶ダイヤモンド被覆超硬合金工具およびその製造方法
   植村賢介，アレキサンダーソルダトフ
   特願 2017‐112584，特開 2018‐204079